FLORIDA INTERNATIONAL UNIVERSITY

Miami, Florida

DEVELOPMENT OF A PLASMONIC ON-CHIP SYSTEM TO CHARACTERIZE CHANGES FROM EXTERNAL PERTURBATIONS IN CARDIOMYOCYTES

A dissertation submitted in partial fulfillment of

the requirements for the degree of

DOCTOR OF PHILOSOPHY

in

BIOMEDICAL ENGINEERING

by

Seyedeh Maedeh Mozneb

2022

To: Dean John L. Volakis
College of Engineering and Computing

This dissertation, written by Seyedeh Maedeh Mozneb, and entitled Development of a Plasmonic On-Chip System to Characterize Changes from External Perturbations in Cardiomyocytes, having been approved in respect to style and intellectual content, is referred to you for judgment.

We have read this dissertation and recommend that it be approved.

Joshua Hutcheson

Sharan Ramaswamy

Shuliang Jiao

Jin He

Gerard L. Coté

Anthony J. McGoron, Major Professor

Date of Defense: March 16, 2022

The dissertation of Seyedeh Maedeh Mozneb is approved.

Dean John L. Volakis
College of Engineering and Computing

Andrés G. Gil
Vice President for Research and Economic Development
and Dean of the University Graduate School
Florida International University, 2022

DEDICATION

I dedicate this dissertation to all future scientists and scientists-in-training, who will find this work inspiring and follow up on its potential for advancing cardiac biotechnology in the 21st century. I dedicate this dissertation to all the patients, whom I believe, one day will benefit from the work done here, or it has all been for nothing! And finally, I dedicate this dissertation to the one, who taught me how to see the truth within me and out there in the universe.

ACKNOWLEDGMENTS

First and foremost, I would like to thank my parents for giving me the right of existence and their unconditional support throughout the years of my studies, morning and night, thousands of miles away. Second, I would love to thank my best friend, my cubicle mate, classmate, lab mate, roommate, and soulmate, Amirali Nilchian, who was by my side, discussing the scientific bottlenecks of this work till dawn for years. I am also thankful for his patience in listening when I could not stop talking about it!

I have been fortunate to have had two major advisors for my Ph.D. journey, where I received two different training disciplines, both academically and personally. I am incredibly thankful to Prof. Chen-Zhong Li for his years of mentorship, friendship, kindness, and trust from day one of our introduction. I am most grateful for his continuous support and uncountable learning opportunities he provided me with, both for my academic and personal growth. Observing his interpersonal skills showed me a high-standard role model for human-human interaction. I am highly and humbly thankful to Prof. Anthony J. McGoron, for his help in bringing me up to the awareness of the boundaries of scientific research, asking the questions that had to be asked when no one else did, and breaking my fear in looking for the truth. I am immensely thankful to Prof. McGoron, without whom I would not have had the courage to enter the scientific society after graduation. I want to thank the scientific committee members of this dissertation, whose perspectives tremendously facilitated the progression of this interdisciplinary work. A special thank you to the staff and faculty of the FIU's animal facility, especially Ms. Deborah Brooks, who assisted in the tissue collection of almost all experimental procedures of this work and supported me through the emotional hardship of animal research. I want to give a special

thanks to the faculty and staff of the AMERI center for research, Dr. Alexander Franco Hernandez, Dr. Patrick Roman, Mr. Steward Schwartz, and Mr. Jonathan Comparan, for their continuous educational support and patience with my learning process. Furthermore, I would like to extend a special thank you to Prof. Ranu Jung, previous chair of our BME department, for introducing me to the FIU in the Washington DC branch. Their "Women in Politics and Policy" workshop presented me with a comprehensive perspective of the United States science advocacy policies and the routes to their accessibility.

I would like to extend a special thank you to the staff, scientists, and fellow graduate students of the National Science Foundation's CELL-MET Engineering Research Center, for always having "a little science and education for everyone." Thank you to my friends and mentors during my involvement with this center for their immeasurable educational discussions, which partially directed me to shape the optimistic perspective I have today for our future scientific community and intrigued me to be a part of it; thanks to Ms. Paige Cloonan, Dr. Ayşe Muniz, Dr. Joshua Javor, Dr. Tony Thomas, Dr. Anant Chopra, Dr. Sharon Fletcher, Dr. Kacy Ronaldson, Dr. Alberto Ribfiaro, Prof. Chris Chen, and Prof. Gordana Vujak-Novakovic. A very special thank you to the people who provided me the opportunity to communicate with an extensive, diverse human community, where I learned how people of different ages and educational backgrounds could be inspired by the exciting science we observe in our labs every day; thanks to Dr. Helen Fawcett, Dr. Thomas Dudley, Mr. Andrew Green, Ms. Brenda Hugot, Ms. Cynthia Kowal, Ms. Nozomi Ito, and all other staff of the CELL-MET workforce development and inclusion teams.

I want to extend a special acknowledgment for the exceptional support of FIU's biomedical engineering family, our staff, graduate, and undergraduate students. I am humbly grateful

to have known and grown up aside fascinating scientists with the purest souls that I get to call my best friends; a warm and unique thank you to my better half, Dr. Lakshmini Balachandar, Dr. Ricardo Siu, Dr. Sana Nasim, Dr. Teshaun Francis, Dr. Arash Moshkforoush, (soon to be Dr.) Mafer Banderas, and (soon to be Dr.) Arianna Ortega. Extending a warm shoutout to the staff of the BME department at FIU, especially Mrs. Claudia Estrada, for her tireless, bright, and shiny daily attitude, who always supported and cared for the health and happiness of the BME student family.

This was an astonishing journey, and all whom I came across were indefinite mentors for me either personally, professionally, or both. I would not have been the person I am today without them. Thank you

ABSTRACT OF THE DISSERTATION

DEVELOPMENT OF A PLASMONIC ON-CHIP SYSTEM TO CHARACTERIZE CHANGES FROM EXTERNAL PERTURBATIONS IN CARDIOMYOCYTES

by

Seyedeh Maedeh Mozneb

Florida International University, 2022

Miami, Florida

Professor Anthony J. McGoron, Major Professor

Today's heart-on-a-chip devices are hoped to be the state-of-the-art cell and tissue characterizing tool, in clinically applicable regenerative medicine and cardiac tissue engineering. Due to the coupled electromechanical activity of cardiomyocytes (CM), a comprehensive heart-on-a-chip device as a cell characterizing tool must encompass the capability to quantify cellular contractility, conductivity, excitability, and rhythmicity. This dissertation focuses on developing a successful and statistically relevant surface plasmon resonance (SPR) biosensor for simultaneous recording of neonatal rat cardiomyocytes' electrophysiological profile and mechanical motion under normal and perturbed conditions. The surface plasmon resonance technique can quantify (1) molecular binding onto a metal film, (2) bulk refractive index changes of the medium near (<200 nm) the metal film, and (3) dielectric property changes of the metal film. We used thin gold metal films (also called chips) as our plasmonic sensor and obtained a periodic signal from spontaneously contracting CMs on the chip. Furthermore, we took advantage of a microfluidic module for controlled drug delivery to CMs on-chip, inhibiting and promoting

their signaling pathways under dynamic flow. We identified that ionic channel activity of each contraction period of a live CM syncytium on a gold metal sensor would account for the non-specific ion adsorption onto the metal surface in a periodic manner. Moreover, the contraction of cardiomyocytes following their ion channel activity displaces the medium, changing its bulk refractive index near the metal surface. Hence, the real-time electromechanical activity of CMs using SPR sensors may be extracted as a time series we call the Plasmonic Cardio-Eukaryography Signal (P-CeG). The P-CeG signal render opportunities, where state-of-the-art heart-on-a-chip device complexities may subside to a simpler, faster and cheaper platform for label-free, non-invasive, and high throughput cellular characterization.

TABLE OF CONTENTS

CHAPTER PAGE

LIST OF FIGURES

FIGURE PAGE

CHAPTER 1. INTRODUCTION

1.1 Motivation and Goals of This Dissertation

The motivation of this dissertation is to apply Surface Plasmon Resonance (SPR) to monitor the electromechanical activity of live cardiac cells. A commercialized SPR device (Biosensing Instruments, Az) is used to monitor real-time variations of the features of neonatal rat cardiomyocyte (CM) contraction in response to chemical stimuli. For the first time, the contraction profile from a monolayer of beating CMs, collected using SPR, has been thoroughly analyzed into its different components for complete feature extraction.

Due to the novelty of using SPR to measure the periodic electromechanical signals from contracting excitable CMs. Furthermore, specific drug studies are carried out to shed more light on the origin of the received periodic signal. The drugs blebbistatin, caffein, and verapamil were used in this study to inhibit the mechanical and partial electrical activity of the CMs. Using inhibitors of these excitatory and inhibitory pathways, features of the chemically induced signals are compared to those of control data. The analytical model, empirical studies, and drug-induced signal variations suggest the source of the periodic SPR signal received from contracting CMs to be the field potentials produced by these cells. We have also taken advantage of the properties of this opto-physical technique to quantify the binding kinetics of the abovementioned drugs to their receptors on the CM's plasma membranes.

The results suggest that the collected signal originated from the charge redistribution near the sensor surface due to an influx and outflux of ions from CMs during a contraction event. The ion redistribution causes a change in the energy of the resonating plasmonic particles as the charged ions to interact with the electron density cloud. The SPR

device detects a difference in these energy alterations and measures them between the reemitted light's refraction angle and the light's original refraction angle ($\Delta\theta$). Our group has denoted this periodic signal as "Plasmonic Cardio-Eukaryography" (P-CeG). Propagating waves of surface plasmons are most sensitive to the charge variations within a penetrating evanescent field of <200nm perpendicular to the metal sensor surface. Therefore, it is noteworthy that all events observed are slightly beyond the cell's plasma membrane, where researchers must also account for biological activities within the cytosol. The overall signal is a collective response of all ionic events from this 200nm sensitive area. Cellular contraction also contributes to the signal; however, to extract a contraction-specific frequency from the SPR signal, a more controlled experimental setting and more robust data analysis paradigms that what is presented in this dissertation are required. To summarize, the main goals of this dissertation are:

1) Use surface plasmon resonance (SPR) to conduct highly reproducible, precise, label-free, and real-time monitoring of a monolayer of cardiac syncytium ionic events during a contraction episode and 2) Use SPR as a real-time and label-free yet sensitive method for monitoring changes in contraction profile of cardiac cells due to environmental perturbations (e.g., drug and chemical exposure).

Future studies in CM electrophysiological analysis might benefit from the cell on-chip device developed in this study. In addition, the model and signal analysis algorithm developed is a more comprehensive and faster analysis methodology for understanding cardiac channelopathies, which allows for the development of novel treatment options.

1.2 Specific Aims

Specific Aim 1: Develop a cardiac cell on-chip platform using an SPR measurement system to provide a more comprehensive method for obtaining a holistic understanding of cardiac cells. Establishing an in-vitro model for drug testing and novel drug development is fundamentally crucial. Despite all previously developed systems, there still exists a need for establishing a preferably non-interference sensing and stimulating platform for recording cardiomyocytes (CM) health parameters, such as cellular function and ion channel activity, under normal and stimulated conditions. Through this aim, we focused on developing a label-free and non-intrusive alternative to currently available methodologies for monitoring cardiac cell contraction in a flow-through environment. We expected that SPR could monitor the changes in contraction properties of neonatal rat CMs (such as beating rate, contraction period, rise, and decay time of signal peaks). Therefore, we investigated the strain of contracting cells, frequency and regularity of neonatal rat CMs' beating, cultured on SPR gold films, and the effects of different flow rates on the contractile signal acquisition.

Specific Aim 2: Characterize changes of the SPR signal from beating myocytes during external perturbations and show that the profiles are highly susceptible to those perturbations. For example, we can show how changes in injected sample chemical concentration affect the cardiac cell's electromechanical function using the P-CeG signal analysis before and after the stimulation. Monitoring these perturbations using conventional methods, such as fluorescent tags and microcantilever-based devices, is a multistep cell labeling process, which increases the chance of experimental error. Hence, using a non-interfering technology like SPR can resolve challenges and bring more

accurate knowledge of CMs function profiles to light. We expected that the results from this aim would better explain the effects of the abovementioned external chemical stimuli on the electromechanical signaling and cell function of CMs. Due to the label-free and non-interfering nature of SPR as the sensing modality, collected data represent the cells' relatively native response compared to existing gold standards, such as fluorescent probes. The outcome of this study will facilitate the development of a system suitable for a heart-on-a-chip model for further functional/behavioral testing of cells for novel drug discovery.

1.3 On-Chip Biosensors

1.3.1 Historical Survey

Many investigators have moved their bioanalysis methods from handheld laboratory devices to miniaturized versions ON-CHIP[1–5]; all processes associated with handling, mixing, and sensing of a specific bio-target are miniaturized on a single sensor or multiple smaller sensors that perform the same operations as laboratory-scaled devices. Such devices, called lab-on-chip, are highly favored nowadays in the healthcare society and for point of care (POC) applications, as they tremendously increase cost efficiency[6], parallelization[7], ergonomics, diagnostic speed, and sensitivity[8]. The essential knowledge and technologies required in developing on-chip biosensors are molecular biology, biophysics, electrochemistry, circuits, and microfluidics. A fundamental understanding of the formerly mentioned technologies is essential to fabricate an on-chip biosensor successfully. Microfluidics are micro-sized flow channels that support sample fluid volumes as low a picolitre while also manipulating biochemical reactions in minimal volumes. Understanding molecular and cell biology is critical to optimizing the design of chemical reactions, which is vital in reaching the desired device design. Finally, picturing

and conceiving the target biological entity as a whole is crucial in combining biology and engineering.

With the development of photolithography in the early 1950s, researchers could begin to fabricate at the micron scale, which evolved into the fabrication of micromechanical structures (MEMS) in the late 1960s. However, it was not until the evolution of soft lithography two decades later that microfluidics could be developed, and thus the fundamental concept of on-chip technology was born. The idea emerged to transfer laboratory equipment and techniques such as PCR, gas-chromatography, electrophoresis, cell lysis, and cell sorting to an on-chip design, making molecular and cell biology research much faster and more accessible[9–12]. Later, the development of micro-total analysis systems (μTAS) caught the attention of military agencies such as the Defense Advance Research Project Agency to detect biological threats. Today, researchers use on-chip sensors and devices for molecular biology, proteomics, cell biology, and chemistry, decreasing the experimental process from hours to just a few minutes and decreasing sample and reagent volumes, thus reducing cost.

Furthermore, co-culturing different types of live cells within a 3D microfluidic device to form a mini-organ (such as heart, liver, lung) for applications like faster drug development allows for another complex form of these lab-on-chip devices, called organ-on-chips. Organ-on-chip devices enable replicating disease models and monitoring the effect of stimuli like drugs on organ behavior in real-time. Most on-chip devices are made of polydimethylsiloxane (PDMS), thermopolymers, silicon, glass, and paper, which will be explained later in the microfluidic classification section.

Features such as low cost, low sample volume, parallel operation capability, ease of use, reduction of human error, availability, portability, and increased sensitivity are the highly desired characteristics that on-chip technology offers. As the world is challenged with the coronavirus (COVID-19) pandemic, point-of-care testing devices are of utmost importance for monitoring and maintaining good global health[13]. Moreover, in developing countries, where healthcare resources for the diagnosis of infectious diseases such as COVID-19 are limited, the concept of a compact and portable diagnostic device is essential to saving the most lives. Nevertheless, on-chip devices have been less favored than conventional ones for laboratory use due to the increased signal/noise ratio resulting from miniaturization and the need for complex electronics assembly and an external operating system to function.

1.3.2 Classification of On-Chip Devices

The on-chip devices can be categorized based on their biosensing element, sensing approach (type of their biotransducers), or microfluidic employed. Depending on the application of the desired biosensor, one or multiple biological components necessary for carrying out a biochemical reaction of interest will be used. These components are usually immobilized on a substrate either connected to the transducer or as one for signal production. For example, catalytic-based biosensors use enzymes[14], microorganisms[15], organelles[16], and cell/tissue constructs, while affinity-based biosensors use antibodies[17], nucleic acids[18], and aptamers[19] as their biological detector component. The bioelement is then conjugated to an electrochemical, optical, or piezoelectric-based signal collector, which makes up devices such as glucose monitors and wearable sweat analzyers[13,20–22], localized surface plasmon resonance apparatus (LSPR)[23] and quartz crystal microbalance

(QCM)[24] devices, respectively. Finally, depending on the output requirements, channel-based[25–27], digital[28], or paper-based[29,30] microfluidics can be integrated with the rest of the components in packaging the complete device. Most on-chip device applications are focused on translating a chemical reaction into a user-friendly observable and interpretable signal for extensive market use (e.g., glucose monitors, pregnancy tests). While the point of care device fabrication and mass production for public accessibility is essential, utilizing on-chip devices in molecular biology, proteomics, and cell and tissue engineering is highly promising. On-chip PCR[31], microreactor-based DNA sequencing[32], protein release characterization and quantification from live cells[33], and electrochemical detection of neurotransmitter release from live neurons[34] are a few of the fascinating possibilities that on-chip devices will be offering for understanding nature. A detailed presentation of the most recent investigations in on-chip development are given in table 1.1.

Table 1.1 On-chip devices based on device components

On-chip device components	Type of sub-components	Medium Type (bioelement/ technique/ instrument)	Mechanism of Operation	Advantage	Drawback	Reference
Biological Element	Catalytic Based	Enzymes	Gel entrapment / covalent bonding / physical absorption	commercial availability, medical applicability, ease of isolation and purification of bioelements from different sources	-	16, 19
		Microorganisms	Covalent bonding / physical absorption	adaptability to high/low pH and different temperature environments and metabolizing new molecules	-	17, 20
		Organelle		special functionality application	-	18, 21
		Cell/Tissue Constructs		high surface adhesivity	-	22
	Affinity-Based	Antibodies	Irreversible bond to a receptor using orientation control of receptor (chemical/electrical control)	electrical / chemical stimulation acceptor, reusable sensor, high sensitivity		23, 26, 27
		Nucleic Acids			-	24
		Aptamers			-	25, 28
Transducer	Electrochemical	Potentiometric	A three-electrode or two-electrode system (working, counter, reference), with working electrode being the transducer	cost effectiveness, simplicity, applicability to a variety of target analytes. studying a reaction's reversibility, receiving quantitative measures of reaction, redox behavior of a compound and electrochemically active surface area of the catalysts	-	15, 29, 30, 3, 32
		Amperometric			-	
		Conductometric				
	Optical	SPR	1) formation of a biolayer of absorbed analyte diffused from a liquid sample in contact with the waveguide's functionalized surface, or 2) changes occurring in the refractive index of the liquid sample itself.	Fast responding, non-invasive, label-free, high repeatability in real-time measurements	complex design of experiments, complex data analysis	33, 34, 35, 36, 37, 38, 39
		Chemiluminescence		fast responding, readily available tags for almost any target analyte, high stability, low noise	tagging required, possible effects on protein conformation changes	
		Absorbance		fast responding, label-free, high immunity to external disturbances, high repeatability	-	
	Piezo electrode-based	Surface Acoustic Waves	-	-	-	40
		Quartz Crystal Microbalance		-	-	41
Microfluidic	Channel Microfluidics	Microreactors, Bioreactors and µTAS devices	Valves, mixers and pumps derive the liquid samples using pneumatic pressure through channels	Handling fluids down to a nanoliter level, ultra-high throughput in sorting biochemical reactions	Too many components necessary for function	42, 43, 33
	Digital Microfluidics (DMF)		a voltage potential derives the fluid into desired channels for mixing, dispensing, merging and analysis	No need for extra components (valve, pump, etc.), handling fluids in picolitre, digital board integration, automation	highly cumbersome fabrication, costly, impractical on mass production and portability	45
	Paper-based Microfluidics	lateral flow	hydrophobic/hydrophilic treatment of channels as well as dimensional design allows for activation of capillary force for selective fluid movement	Abundance of fabrication material, portable, simple fabrication, fast mass production, cost-effective,	-	46, 47, 48
		vertical flow			-	

1.4 Methods for Cardiomyocyte Characterization

With the invention of the electrocardiogram (ECG or EKG) machine in 1895 by the Dutch physician Willem Einthoven, non-intrusive fundamental studies of the human heart's electrical activity could be initiated for the very first time. Afterward, several techniques and methodologies were developed to understand the physiological characteristics of cardiac cells and investigate the embryology and developmental analysis of cardiac evolution in mutations and heart disease[35]. *In-vitro* and *in-vivo* studies were adopted and optimized for cardiac cell functional and structural analysis[36]. With the beginning of the tissue engineering era, several studies focused on developing cardiac tissue to better understand the organ's physiology as a whole and possibly for regeneration purposes (e.g., implantable cardiac patches)[37,38]. The advancement and preference of using induced pluripotent stem cells (iPSCs) for tissue fabrication as a substitute to mammalian cell lines brought significant challenges to tissue engineering and cellular regeneration[39]. The differentiation of iPSCs into CMs resulted in the construction of immature tissue. A multifaceted improvement became essential to establish compatible samples for physiological studies, drug testing, and discovery or clinical use (implants). This improvement included but was not limited to monitoring cardiac cell health parameters, such as metabolic rate and respiration in conjugation with structural studies. From there, the focus of several researchers shifted towards investigations in the following areas in cellular and sub-cellular levels.

1. Surface patterning for enhanced cell attachment and aligned cell culture[40]

2. Novel designs of cardiac-specific engineered extracellular matrix (e-ECM) and scaffolds to improve cell morphology, function and mechanical properties, gene expression, and cellular heterogeneity[41,42]
3. Using electrical, mechanical, and chemical cues in aligning cardiac cells and their improvement towards adult-like cells[43,44]
4. Novel sensor designs for measuring metabolite distribution, action potential propagation, and force of contraction in a cell monolayer[45]
5. Developing an integrated tissue on a chip sensing system by fabricating heart-on-chip devices for real-time and continuous recording of the microenvironment and cell metabolic properties[45]
6. Novel optical modalities to observe cardiac action potentials, acquire high-resolution images from deep within scattering tissue, advance to higher spatiotemporal sensitivity, and take advantage of less invasive approaches[46–48]
7. Developing accurate algorithms for measuring contractile function and content evaluation of cardiac cells[49]

The following sections will introduce the progression of research and the development of new techniques in monitoring cardiac cells' functional and structural characteristics.

1.4.1 Basic Cardiac Physiology and Electrophysiology

The human heart has different cells working together to pump blood throughout the body. Cardiomyocytes (cardiac muscle cells), fibroblasts (cells making up the cardiac ECM), and cardiac pacemaker cells (responsible for the action potential generation) are the three main types of cells making up a human heart. Fully matured adult CMs are about 100μm long, 10-25μm in diameter, and highly striated. They are cylindrical and connected

to their neighboring cells through cellular bridges such as gap junctions and intercalated disks; these are highly important in fast signal transduction between cells. Healthy distribution of gap junctions on cells' plasma membrane and the presence of intercalated disks results in the production of a homogeneous cellular contraction following a fast signal propagation between cells in a cardiac syncytium. This signal, namely the cardiac action potential, depends on the cells' transmembrane potential developed based on continuous ionic exchange.

Each cardiac muscle fiber has hundreds to thousands of rod-shaped myofibrils, densely packed together, making about 80% cellular volume. Mitochondria and other cell organelles are distributed between these myofibrils. Each myofibril contains the contractile element of CMs, the sarcomeres, made of myofilaments that include the contractile proteins. Central thick filaments made of myosin are connected in the middle at the M line. In contrast, the more lateral thin filaments containing actin are anchored by alpha-actinin-rich Z disks on each side of the sarcomere. The sarcoplasmic reticulum (SR) and the T-tubules are organelles in the intracellular space responsible for regulating contraction. Large numbers of mitochondria, the energy-providing elements during contraction, are closely associated with SR.

In developing a contraction, an electrical signal, called an action potential, is initiated in the sinoatrial node at the base of the heart in the right atrium and which automatically travels through the sarcolemma towards the apex of the heart. Initiation of an action potential depends on the continuous function of Na^+/K^+ protein pumps and Na^+/Ca^{2+} exchanger proteins located on the CMs plasma membrane. These proteins maintain a negative potential across the plasma membrane and are crucial in CMs

electrophysiological homeostasis. This negative potential, called the resting membrane potential, activates consecutive voltage-gated ion channels to open and close in exquisite harmony to form the cardiac action potential. The cardiac action potential is marked by its distinctive plateau of 300 milliseconds in duration, corresponding to a temporary charge balance between ions inside and out of the cell. Following an action potential, a rise in intracellular calcium ion levels provides the final trigger for contraction. Ca^{2+} ions enter the cell and bind to regulatory sites on troponin, a significant protein in thin filaments. With enough calcium ions and adenosine triphosphate (ATP), the thin filament begins to slide due to actin-myosin binding, inducing muscle contraction. When the amount of calcium ions subsides, the binding site on actin is blocked, and the muscle fiber relaxes.

Several elements leading to cardiac muscle contraction can become dysfunctional, resulting in an incomplete contraction. Understanding the reasons for these malfunctions may help advance the development of lab-made CMs. Therefore, functional and structural analysis of cardiac cells has been crucial in developing mature and accurate cardiac tissue models.

1.4.2 Functional Characterization of Cardiomyocytes

In the functional characterization of cardiac cells, many in-vitro approaches were developed to investigate different aspects of an action potential and its propagation, amongst other parameters involved in a contraction. For electrophysiology, patch clamping[50], using multielectrode arrays (MEA)[51] and fluorescent imaging of cell proteins have been used; in contrast, traction force microscopy52, atomic force for monitoring cellular beating profile microscopy[53], impedance-based assays[54], video microscopy[55] and most recently SPR[56] have been used.

Patch clamping is one of the more traditional modalities that provides information on ion currents and is highly sensitive in detecting currents directly from a single cell[57]. However, its invasive nature (breaking through cell membrane for signal acquisition) cannot be used for long-duration studies. Therefore, for a higher throughput experimental design and a less invasive approach, several groups have used the MEAs, where the field potential is recorded from a single or a monolayer of cells[58]. Further, the use of calcium indicators and voltage-sensitive dyes are two of the most common modalities in understanding the physiology of CMs. Given the integration of a fast responding camera, the output data can be reliably interpreted[59]. Nevertheless, the tags must enter the cell or get conjugated into its plasma membrane proteins to produce the signal. Thus, there is a probability of altering the cell's environment, resulting in a less accurate physiological output.

Another aspect of analyzing cardiac cell functionality, and the most unique yet decisive indicator of their health, is their spontaneous contraction features (e.g., force, frequency). Traction force microscopy combined with embedded fluorescent beads and atomic force microscopy (AFM) two of the most favorable yet time-consuming techniques employed to gather information on CMs contraction profiles[53,60]. SPR's latest application for monitoring the mechanical behavior of cardiac cells was established only a few years ago[61]. Researchers used the optical concept of SPR for tracking contraction profiles of excitable cells. The idea offers much hope in single CM observation, and sensing since ion/photon interaction (the cause of the signal received by SPR from excitable cells) allows for a more efficient energy transfer paradigm than conventional techniques. A more comprehensive and exciting alternative is SPR imaging, which was used to validate cyclic

SPR signal by employing a bright-field image alongside the SPR signal to monitor cell motion[61,62]. Our group has also been successfully testing the effect of the external perturbation on a cardiac monolayer contraction using SPR[56], which will be discussed in Chapter two.

1.4.3 Structural Characterization of Cardiomyocytes

In addition to mechanical behavior, a structural analysis of CMs is crucial to understanding cell maturity and healthy tissue formation. Current tissue assemblies rely on mechanical and electrical stimulation to develop mature CMs. Relative maturity of a cardiac cell is often measured by its sarcomere length, elongated morphology and cell organization, cellular genetic profiling, expression of cardiac-specific membrane proteins such as connexin-43, and cellular metabolism analysis using mitochondria, lactate, and glucose quantification[36,63,64]. A fundamental understanding of CMs' pathophysiology will help extract the most relevant properties of cells that can fabricate a more accurate tissue construct.

A healthy adult CM can be binucleated, has an elongated rod shape with a surface area of 10,000-14,000μm^2 and is anisotropic for efficient signal transduction[2]. In oxidative metabolism of cardiac cells, elements such as glucose, lactate, glycogen, long-chain fatty acids, pyruvate, and various amino acids play a key role[65–67]. Adult CMs have long F-actin fibers with an abundance of sarcomeric α-actinin and troponin-I proteins. Higher expression of connexin-43 and integrin-ß1 is an indicator of better cell-cell and cell-ECM interactions of cardiomyoytes[68]. Also, the ratio of CMs to fibroblasts in culture is very closely associated with the enhanced functionality of cells.

In contrast, uncontrolled growth of fibroblasts has been known to be a feature of many cardiac pathologies[69], primarily due to increased stiffness of the ECM and more resistance to contraction force. Although heart metabolism is highly flexible in response to different stimuli (e.g., cardiac cells can switch their metabolism to glycolysis in anaerobic environments), CMs in their early development are more susceptible to damage, given an immature metabolic profile[65]. All structural components of CMs, such as the M-bands, Z disks, microtubules, and abundance of mitochondria, also indicate a healthy cell. Several studies have focused on genetic expression analysis of adult CMs versus immature CMs, which concluded higher ventricular cell maturation, gap junction protein connexin-43, and contractile cardiac protein beta myosin's heavy chain[70].

Other techniques, such as reverse transcription-polymerase chain reaction (RT-PCR), immunocytochemistry, immunohistochemistry, radionucleotide tracers, measuring the metabolic flux rate, and western blotting, have also been employed for an understanding of the structural parameters of CMs[36,65,71,72]. These measurements also rely on extensive labeling of cells, separate analysis for different metabolites, and several other instruments for analyzing the health of the cells. Also, the existing modalities cited above mostly explore the structural properties of fixed cell samples. Understanding the direct link between real-time cell health and cell function is essential for developing a more comprehensive live CM electrophysiology research model.

1.5 Controlling Cardiomyocytes' Microenvironment

Due to the challenges in developing a fully functional cardiac tissue *in vitro*, many protocols were tested to produce a highly dense and oriented tissue structure using artificial

cues such as controlled electrical and mechanical stress induction on cell-cultured environments[45,66].

1.5.1 Physical Stimulations

Cardiac cells are electrically active. Therefore, induction of an electrical field or point stimulation can tune the activation of voltage-gated ion channels, controlling a few of the cell's signaling pathways. For example, Ronaldson et al. exposed their lab-constructed cardiac tissue to controlled electrical and mechanical stimulations known as a "training program," which resulted in adult-like gene expression profiles, organized ultrastructure, and presence of transverse tubules, oxidative metabolism, and functional calcium handling[36]. Other studies used electrical stimulation to synchronize the contraction of multiple CMs[43,45,73] and have used MEA's for inducing gene expression and extracting CMs' orientation information[70].

Mechanical beating is another critical functionality of CMs, in which the summation of all cells contracting together (in *syncytium*) makes the "heartbeat." Applying an external mechanical force/pulse stimulation to CMs is shown to train the cells into beating in a synchronized manner[36]. Administration of mechanical cues was carried out through inventions such as microfabricated pillars and membranes integrated within microfluidics that house CMs[44,74,75] or oscillatory robotic probes on the CM's substrate[74].

The other physical stimuli that can be applied are optical based. The concept of optogenetics has been recently established for several biomedical applications, such as understanding the underlying reasons for epilepsy[76]. A light source activates an optically active biological element (e.g., protein) to drive and control a desired biological reaction in optogenetics. However, the thick myocardium does not allow efficient light transfer to

target cells in cardiac constructs. Hence, the route of optical stimulation for clinical applications is limited. Nevertheless, there still are exciting studies on the pacing of cardiac cells[77,78], along with discoveries of fibroblasts' role in action potential conduction velocity[79], which make optogenetics a unique tool in developing the correct image of cardiac cells' function.

1.5.2 Temperature and Dissolved Oxygen Regulations

Culturing cells under controlled physiological dissolved oxygen, carbon dioxide, metabolite (energy source), pH and temperature conditions are beneficial to cells' growth and maturity. For example, in cardiac tissue bioreactors where flow is supported, continuous oxygen delivery using oxygen carriers through perfused media to cardiac tissue increases cell viability. In addition, it results in the development of thicker, healthier tissue contructs[80].

Lastly, maintaining a physiological temperature at 37°C is vital for cardiac cell culture. Like any other mammalian cell type, CMs are highly dependent on physiological temperature to preserve their function *in-vitro*. In addition, the protein conformation of several of the membrane proteins in CMs is highly reliant on the maintenance of the physiological temperature. Decreased temperature from physiological values will result in cardiac cell's synchronized beating rate and the propagation velocity of the synchronized field potential to reduce drastically[81,82].

1.6 Heart-on-Chip Devices

As the need for understanding cardiac functionality in three dimensions evolved, researchers started focusing on adapting structural and functional analysis techniques mentioned in sections 4.2 and 4.3 of this chapter for application in three-dimensional (3D)

tissue. Most challenges in this area lie in fabricating a long-lasting, highly compatible engineered cardiac construct compatible with active human tissue for efficient and effective regeneration of diseased tissue. To achieve such a high standard for 3D tissue that is to be used in clinical settings, the use of heart-on-chip devices offers a comprehensive perception of needed enhancements. A heart-on-chip is a microfluidic device resembling and reproducing the main features of a human heart in micro dimensions. Modeling different cardiac diseases, organ-vasculature interaction, substrate mechanical property optimization, signal propagation order, and testing the cardiotoxicity of a drug in 3D tissues are some of the driving incentives for fabricating heart-on-chips. However, as mentioned earlier, the complex structure of the human heart and challenges associated with growing mature cardiac cells in culture to match that of an adult human CM could encounter several threats. Maintenance of tissue over prolonged durations, inducing and controlling tissue vascularization, designing highly dense and organized CMs, accurate replication of cardiac ECM and its mechanical properties, and the effect of fluid flow on cell function are some of the challenges.

With more advanced technology and microfabricated devices, a few platforms were made for constructing a 3D cardiac tissue with embedded electronics that would act as a sensing and stimulating system to be used as a cardiac patch or work towards the better fabrication of one[83–87]. Feiner et al. studied the possibility of depositing gold electrodes, using lithography techniques, directly on albumin scaffolds as sensing, stimulating, and drug release platforms for cardiac tissue[84]. Later, they completed the design by developing a patch composed of embedded gold sensors within a fibrous scaffold with cultured cardiac cells[86]. The device was capable of monitoring cell activity (contraction) from 9 different

sensing points on the scaffold and a stimulating program for synchronizing each beat across all tissue. Their design also had a drug release polymer embedded within the scaffold's mesh for simultaneously monitoring the drug's effect on tissue contraction. Common in all the research mentioned above, tissue contraction profile, oxygen consumption, and metabolic indices were defined as essential parameters in cardiac tissue engineering and were investigated separately. The gaps in the research described here are:

1. Lack of a comprehensive label-free and non-interfering platform for continuous measurement of cardiac cell health and functionality (e.g., the force of contraction, oxygen consumption, and metabolism) in real-time.
2. Correlating metabolism and respiration to function (contraction profile) under different environmental conditions (e.g., drug stimulation, temperature change, oxygen administration).
3. Tracking and understanding cellular behavior through real-time monitoring of ion channel activity

Information acquired from such a platform is essential for advancing current cardiac cells and tissue structural and functional properties before clinical use and drug development. For example, a fully functional cardiac patch with near-native tissue to regenerate muscle damage from myocardial infarctions can decrease the chance of heart attack recurrence and possibly eliminate the need for further invasive procedures. Also, replicating the proper form of personalized cardiac tissue can facilitate the production of novel drugs for cardiac channelopathy-based diseases, which leads to significant arrhythmias and cardiac failure.

1.7 Surface Plasmon Resonance Biosensors

In 1902, a Johns Hopkins physicist, Robert William Wood, made an interesting observation. Using a diffraction grating with metal covered on its back, he looked at polarized white light and saw unusual dark and light bands patterns in the reflected light[88]. Although several theories were proposed to explain these anomalies, it was not until 40 years later that Fano concluded that the abnormal bands were associated with surface waves (surface plasmons)[89]. In 1968, Kretschmann and Otto both showed, with different configurations, that these surface plasmons (SPs) can be excited by employing attenuated total reflection[90,91]. After the 1980s, with the exploration of evanescent waves and their high sensitivity to small matter (e.g., antigens, proteins) variations, the technique was applied to study the interaction kinetics between two biomolecules[92]. Further past that point, SPR was used for many applications such as thin-film characterization, helping understand processes taking place on metal surfaces, and in a turning point, for gas and biomolecule detection[92,93].

SPR is a phenomenon that occurs under specific conditions within the plasmon's quasi-particles at a noble metal surface (usually gold or silver). Based on the theory of quantum mechanics, an electron's position can only be described by a probability function. Therefore, an electron can also be viewed as a stationary wave (cloud). The calculation of the probability of an electron's presence in a known point in space gives a quantity called the electron density of the electron cloud. The outer shell electrons of metals, forming up the electron cloud, are shared by all the atomic nuclei. SPR is the collective oscillation of the electrons, which are not bounded to individual atoms, triggered by the light's alternative current (AC) electric field. The Surface Plasmon (SP) wave propagates along the metal

surface, and in the case of nanoparticles, it changes to a standing wave. When a p-polarized light hits a metal surface, its photons couple to the free electrons in the electron density cloud of the metal and generate SPs. Total internal reflection occurs at a correct incident angle, where the minimum reflectivity is observed. As a result, an evanescent wave rises <200 nm in the medium on top of the metal surface. The evanescent wave is highly sensitive to changes in the refractive index of the medium, based on variations in its dielectric constant, hence helpful in detecting changes in mass and motion of small molecules. The plasmon energy can be defined as:

$$\omega_p^2 = Ne^2/m\varepsilon_0 \ \ e.v \qquad \text{(Equation 1)}$$

Where ω_p is the plasmon frequency, N is the number of density of electrons ($1/m^3$), e is the electron charge ($1.602*10^{-19}$ coulombs), m is the electron mass ($9.11*10^{-31}$ Kg), and ε_0 is the permittivity of free space ($8.854*10^{-12}$ $N.m^2/coulomb^2$). Dielectric of the metal, angular frequency of the SPs, and refracted angle theta are presented, respectively:

$$\varepsilon(\omega)=1-(\omega p/\omega)^2 \qquad \text{(Equation 2)}$$

$$\omega p=\sqrt{4\pi e2}\ N/m \qquad \text{(Equation 3)}$$

$$\sin(\theta_R) = \sqrt{\frac{\varepsilon 1.\varepsilon m}{(\varepsilon 1+\varepsilon m)\varepsilon 2}} \qquad \text{(Equation 4)}$$

ε_2 is defined as the dielectric constant of the BK7 prism used in the BI2000 device (Biosensing Instruments, AZ.) with a value of 2.30. On the other hand, the dielectric constant of the medium (ε_1) flowing on top of the sensor surface alters in response to molecular binding events due to the medium's viscosity changes. This variation in the dielectric constant of the medium results in its refractive index (n) to change as well,

causing the reflected pseudo-image to shift. This shift is observed through expansion or reduction of the reflected angle, theta.

SPR technique can be applied in several aspects in pharmaceutical research and drug discovery applications. From target identification and characterization to pharmacokinetics of drugs as a secondary measure in clinical trials, SPR is making it highly competitive as an all-in-one device compared to other available technologies. Due to its nature in design and unlike pull-down assays like filter binding, which are used for determining a physical interaction between proteins, SPR can detect the number of complexes formed, even in the presence of free material (such as unbound molecules in the sample liquid, which are not the target of the assay)[94–96]. Quantifying binding kinetics of molecular interactions will allow SPR to characterize the weakest complex formations usually lost during washing steps in conventional methods. The diffusion rate of an analyte controls the upper and lower limits for association and dissociation kinetics to its binding partner immobilized on an SPR sensor and baseline stability of the instrument, respectively.

Like other biosensors, SPR biosensors should also be characterized for their detection limit and sensitivity. The detection limit for SPR biosensors can be defined in one of three ways: 1. Minimum size of molecule detectable in solution, 2. Minimum concentration of the detectable sample, and 3. The ability to detect very fast or prolonged binding interactions (measuring low or high-affinity interactions). For example, as the analyte size in the solution gets smaller, the overall intensity of the SPR's signal will

decrease. Hence, with the right design of experiments, the accurate number for the sensor's limit of detection can be achieved.

It should be stated that given all the advantages of using an SPR biosensor, it also has some cons that must be considered when designing a suitable sensor. For example, an active biomolecule's presence is mandatory for receiving a signal from SPR, which relies on highly accurate and controlled immobilization of biomolecules on the SPR sensor. On the other hand, sensor reusability in SPR studies depends on the development of unique sensor surface regeneration chemistries that might affect future binding events. Today's technology advancements for controlled ligand dispensing under an electrical field[97] and progress in quantum computing and artificial intelligence provide us with the necessary tools to tackle these drawbacks on SPR.

1.7.1 Lab-on-Chip and Cell-on-Chip SPR Biosensors

With the establishment of photolithography and soft lithography and an increase in demand for novel portable biosensors, the concept of lab-on-chip devices was combined with SPR to develop state-of-the-art technologies for multiplex and non-invasive biosensing applications. Especially with the substitution of a noble metal nanoparticle-coated optical fiber instead of the heavy-duty SPR instrument, lots of hope rose from the possibility of fabricating the next generation of portable and point of care (POC) biosensors.

A grating-coupled SPR sensor (GC-SPR) was developed by Boril et al. for integration into a microfluid device for studying cell adhesion kinetics with and without an external stimulation[98]. Another group combined surface plasmon resonance imaging (SPRi) in a microarray chip with on-chip mass spectroscopy to identify specific

carbohydrate ligands using a target protein binding to various cytokines[99]. Researchers have also focused on advancing the data analysis techniques using a system-on-chip incorporated SPR device, combining optical computing for sensing biochemical elements[100].

Although SPR has been chiefly used for measuring the association and dissociation kinetics of molecular binding, in recent years, our lab and other groups have found potential applications of cell-integrated SPR for cell micromotion monitoring[101], drug exposure and vesicle release from cells[102], live cancer cell attachment monitoring[103] and binding kinetics of membrane proteins in single cells[104]. SPR has even been used in an exciting study by Fathi et al. for detecting early-stage differentiation of stem cells into endothelial cells. At the same time, conventional techniques such as flow cytometry and fluorescent microscopy could not define the stage of differentiation[105]. Furthermore, SPR can exploit photonics in acquiring information from cells and possibly tissue as a label-free and real-time technique. Therefore, cells and tissues will receive a minor intervention with their native environment, giving the most accurate response compared to conventional fluorescent tagging and electrochemical measurement of cellular properties.

We have selected Surface Plasmon Resonance (SPR) as a label-free technique to explore ongoing ionic and molecular events during a contraction episode of CMs under normal and perturbed conditions.

1.8 Chapter Outcome

As the need for developing a non-surgical solution (e.g., drug treatment) for treating cardiac channelopathy-induced arrhythmias increases, a more thorough approach is needed for novel drug testing and development. Since other methods have proven to be

cumbersome to assemble and adjust for various *in-vitro* drug testing applications, efforts in establishing a new methodology are relevant. Surface Plasmon Resonance technology, an optical technique with high spatiotemporal resolution, is exploited in this investigation as a novel method for myocyte contraction profile acquisition and analysis.

This work aims to validate Surface Plasmon Resonance as an alternative to the already existing gold standard techniques for monitoring cardiac cells' electromechanical profiles. By culturing live cardiomyocytes on thin gold SPR sensors, we may record their electrical and mechanical properties simultaneously through surface plasmon resonance. **We hypothesized that the electrical potential differences across cardiomyocytes' cell membrane and their mechanical force during an episode of cellular contraction changes the gold's surface plasmons' resonance energy, thus changing the refraction angle of the light that induced surface plasmons.** The change in light's refraction angle (millidegree) from light's original refraction path before cellular contraction contains quantifiable information related to CM's electromechanical properties. Due to its label-free nature, SPR is less complex and faster in acquiring data than fluorescent tagging techniques conjoined with microscopy. Sole microscopy techniques with no labeling need complex sequential images taken to extract electrophysiological data from the signal. However, the SPR signal from live CMs can directly correlate to extracellular field potential and cell-substrate contraction strain, potentially decreasing the recurring error in data analysis.

Nevertheless, suppose the target of the study is limited to the contractility of cardiac cells along with observations of the field of motion (monitoring extracellular molecules and vesicles, calcium fluxes). In that case, a microscopy configuration might be most beneficial. Though it is worth mentioning that even in such cases, merging advanced signal

processing techniques (e.g., machine learning and artificial intelligence) with plasmonic sensing of excitable cells might be resourceful in gathering simultaneous electromechanical information from CMs.

The objective of this research is met through two aims: **1) Development of an on-chip cardiac myocyte platform and SPR measurement system** and **2) Characterization of changes in the SPR signal throughout the cardiac cycle during external perturbations.** We have used microscopy as a conventional method for monitoring cardiac cell contraction profiles using digital image correlation before SPR studies. The periodic SPR response unit profile of contracting cells is compared to those obtained through image processing. Signal features of both SPR and microscopy data were compared to previously reported results. We have also tested the effects of cardiac-specific drugs such as verapamil and blebbistatin on signals acquired from contracting cardiac cells.

Surface Plasmon Resonance technology offers a vast unexplored field of applications, especially in monitoring live cell activities in real-time, given its high temporal (1000Hz) resolution and sub-micron spatial resolution (150nm). We hope further investigation on the subject will facilitate new drug development and shed light on novel ion channel pathways within excitable cells, resolving their possible resultant channelopathies.

CHAPTER II. DEVELOPMENT OF ON-CHIP PLASMONIC DETECTOR FOR CARDIAC MYOCYTE FUNCTIONAL RECORDINGS

2.1 Introduction

It has been more than a century that *in-vitro* cell cultures alongside *in-vivo* animal and human models have been used for unraveling underlying causes of human diseases. In the case of cardiovascular diseases (CVDs), due to the nature of the human heart as a complex machine, a comprehensive high-resolution real-time grasp of cardiac events can play a crucial role in pointing research in its proper direction. A comprehensive understanding of the periodic events in the heart must include the organ's electrical signal conduction and cell contraction. Cardiac fibroblasts, vasculature, extracellular matrix (ECM), and cardiomyocytes of different heart regions (e.g., ventricular, atrial, and nodal) constitute a simplified classification of this exquisite organ's cellular structure. The adult human heart has more than four hundred different types of cells based on their evolutionary and developmental origins[106]. The clockwork of molecular activity of these cells' ion channels drives the action potential harmonically through the whole organ for its contraction. Following the behavior of each of these constituents from single ion channels to complete organs, as a UNIT, is the key to accurate clinical translations of disease preventions and treatments made in the laboratory.

Due to the vast scale difference between cardio-specific molecules and the heart itself (from nanometer to centimeter), technologies that have been developed to interact with the target cardio-biological entity have a spectrum of sizes as well. For example, patch clamps, mass spectroscopy, and fluorescent probes are commonly used to characterize voltage-gated ion channels of cardiac cells. At the same time, devices such as the

electrocardiogram (ECG) and photoplethysmography (PPG) are used for a systemic response collection from the organ-vasculature functions. Partially bridging this gap, at least between the micrometer and millimeter-scale, with the existing concept of surface plasmon resonance is the goal of our study.

An immense surge of scientific data and evidence has come to light in the past few decades because of rising new technologies. Microelectromechanical System and Nanoelectromechanical System (MEMS and NEMS) devices, as well as progressions in artificial intelligence (AI) and machine learning, have made it possible for today's researchers to observe and manipulate biology (in its most primitive form, though!) in nanoscale. This nanoscale/microscale's manipulation results in a clinical product (e.g., gene editing bio carriers, novel nanodrugs, or origami micro-stents) with the hope of reaching CVD treatments and cures. Implementation of such products *in-vivo,* given misinterpretations of the systemic response to such manipulations, can cause a faulty upstream butterfly effect. As we previously noted in chapter 1, heart-on-chip devices have been developed to expedite the systemic understanding of microscale manipulations of tissue in culture. With the overall aim of creating a clinically valuable cardiac tissue for regeneration, or to facilitate novel drug discovery, heart-on-chip devices hold state-of-the-art status in the field.

Current heart-on-chip devices lack a reliable holistic approach for monitoring and manipulating cardiac tissue using electrical and mechanical stimulations[83,107]. Furthermore, the scale difference of biological entities mainly brings about hardship for the researcher and the device to gather information on all scales. Therefore, it seems that recycling an old

concept (surface plasmon resonance) for monitoring modern multi-scale interactions with cardiac tissue (e.g., application in a heart-on-chip device) is relevant.

2.2 Conceptual Background

Before we dive into the details of experimental methodology, it is essential to discuss the most recently established and agreed-on scientific concepts involving surface plasmon resonance interaction with excitable cells such as CMs. Therefore, the following pages present a mathematical and physical explanation of surface plasmon resonance phenomena derived from the Schrödinger equation, Maxwell equations, and energy conservation law. Moreover, since we will be interacting with the nano, micro, and millimeter scales of biology and chemistry in one setting, a brief commentary is also presented on cardiac cells' evolutionary, developmental and electrophysiological aspects.

2.2.1 Mathematical Elaboration of Surface Plasmons Interacting with Excitable Cells

For this dissertation's purpose and within the scope of our study, a simplified adaptation of the excitable cell-SPR model is presented in Figure 1. The figure describes each element within the excitable cell-SPR model, where two adjacent CMs are located within the detection disk of the evanescent field. Each environment through which light travels is shown in Figure 2A. The green arrow demonstrates the magnitude of the electrical field in each medium. We sought to define a correlation between refraction angle change ($\Delta\theta$) to changes of charge over time near CMs' plasma membrane using the excitable cell-SPR model. We will refer to this correlation as the ***charge-angle correlation function***. A summation of all estimated values across the selected detection area of the sensor is used to quantify the extracellular charge at each point in time during cells' contraction cycle.

Obtaining changes in charge over time for contracting CMs might have a correlation to their filed potential profiles.

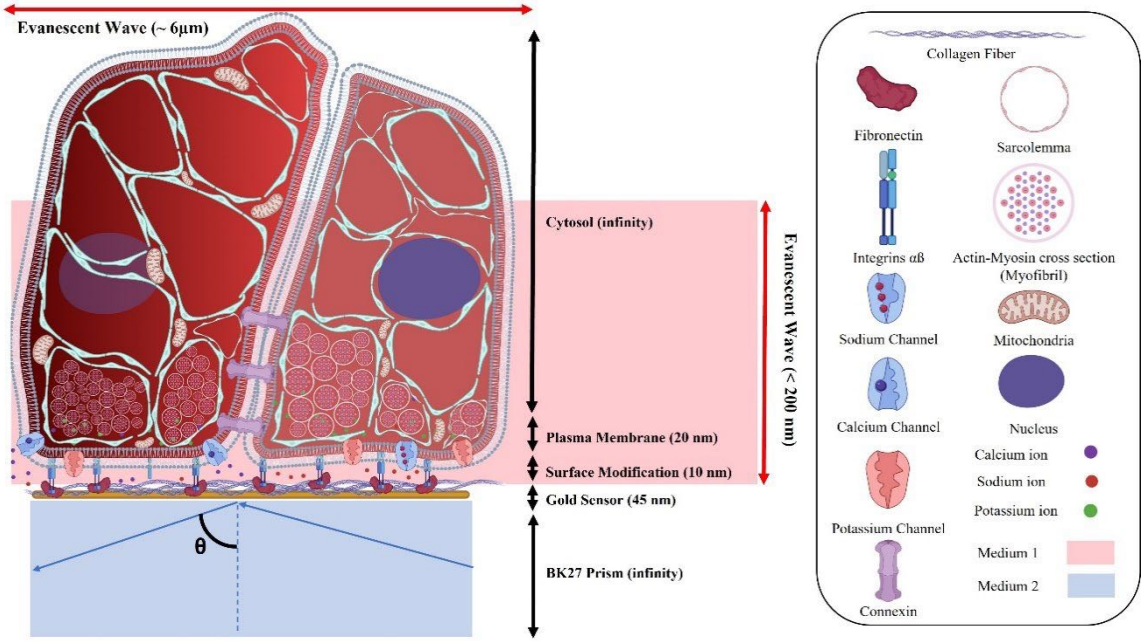

Figure 1. Illustration of the excitable cell-SPR model for two adjacent CMs. Light with a wavelength of 630 nm is radiated through the prism (n=2.30, medium 2) onto a 45nm gold film, which is then totally internally reflected. The so-called Kretschman configuration is used as the plasmonic modality to monitor the physiological events of CMs within the evanescent field (medium 1). In the light's travel trajectory, the thickness of the cell (~10μm) and prism are assumed to be an infinite medium compared to plasmonic spatial sensitivity.

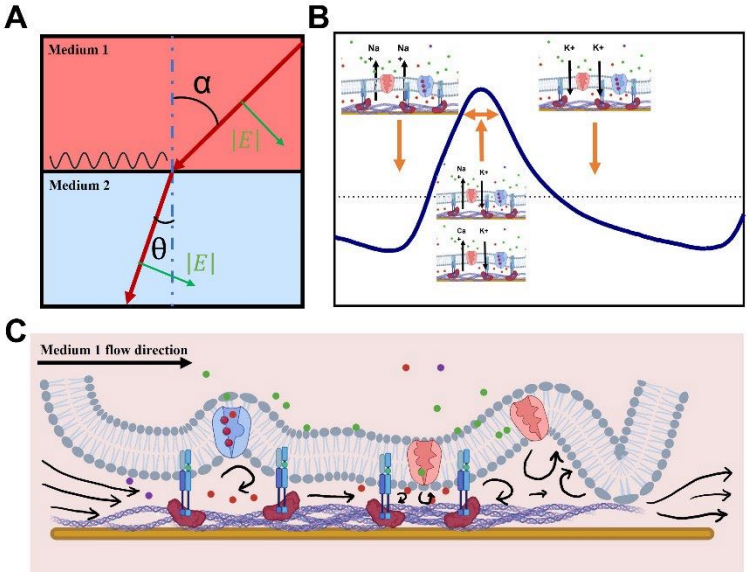

Figure 2. Biophysical illustrations of the excitable cell-SPR model. A. Light's direction of travel traced by the red arrow after total internal reflection (TIR) is depicted. Medium 1 constitutes the cell membrane, surface modifications of collagen and fibronectin, and dynamic fluid flow. The black wave shows the propagation of electromagnetic waves parallel to the sensor surface because of TIR. Medium 2 is solely the device's prism with a refraction index of n=2.30. B. Consecutive events of a cardiac action potential are overlapped with a sample signal of contracting CMs on the SPR sensor. Ion channel events of depolarization, plateau, and cardiac action potential repolarization are shown with orange arrows from left to right, respectively. C.

Possibility of turbulence fluid flow between the cell and the gold surface is depicted. In the case of CMs, as the cells contract, regions shown with spiral arrows indicate that turbulent flow will shrink or expand, increasing and decreasing the turbulence kinetic energy. The horizontal arrow shows the direction of the medium flow.

As discussed in chapter 1, SPs are a rippling wave in the electron density cloud as an electromagnetic wave (e.g., light) interacts with metal atoms. Noble metals like gold are inert; metals also have a very dense atomic arrangement that contributes to making up a continuum of their free-electron cloud's wavefunction, which will be discussed in the next paragraph. Due to Heisenberg's uncertainty principle, the exact position and momentum of quantum objects, such as electrons, cannot be determined in an enclosed space. Instead, a probability wavefunction, called Ψ(t,x), defined by Schrödinger's equation, is used to estimate the probability position of electrons in space and time. A time-independent format of Schrödinger's equation will be used in determining our charge-angle correlation function. The Schrödinger equation suggests that the energy probability wavefunction (EΨ(x)) of the electron density cloud's total energy comprises kinetic (first term of eq. 5) and potential (second term of eq. 5) components.

$$E\Psi(x) = \frac{-\hbar^2}{2m}\frac{d^2\Psi(x)}{dx^2} + V\Psi(x) \quad \text{(Equation 5)}$$

E is the electron's total energy, ħ is the reduced Planck constant (h/2π), m is the electron's mass, and V is the potential wavefunction of the electron gas cloud. Solving Schrödinger's equation for E in an enclosed space, the length of L for electrons of state n defines the total energy of the electron density cloud:

$$E = \frac{\hbar^2 n^2 \pi^2}{2mL^2} \quad \text{(Equation 6)}$$

The energy ϵ is quantized and can only have specific values. The probability wavefunction, on the other hand, alternates between the following two equations for odd and even electron state values:

$$\Psi(x)=\sqrt{\frac{2}{L}}\cos\left(\frac{\pi n x}{L}\right) \qquad \text{for n=1,3,5…} \qquad \text{(Equation 7)}$$

$$\Psi(x)=\sqrt{\frac{2}{L}}\sin\left(\frac{\pi n x}{L}\right) \qquad \text{for n=2,4,6…} \qquad \text{(Equation 8)}$$

The squared value of the function ($|\Psi(x)|^2$) is commonly known as the amplitude of the probability wavefunction. The collective oscillations in $|\Psi(x)|^2$ of the free electrons in three-dimensional space forms the quasiparticle of plasmons.

When an electromagnetic wave such as light strikes the gold surface, gold absorbs the light and dissipates its energy within the metal. The dissipated energy gives rise to the already existing plasmons, which redistributes the gold's conductance electrons as an oscillating electromagnetic wave (light) travel through them. In the development of SPR devices, a prism is employed to induce coupling of the light's resonance frequency to that of the SPs of the gold layer (exciting the plasmons). It is configured based on Kretschmann–Raether's[91] configuration to result in a total internal reflection of light. This excitation at the right frequency boosts the electron density cloud's wavefunction's amplitude ($|\Psi(x)|^2$). Notice that an increase in the amplitude will not affect the total energy of the electron density cloud (E) due to the law of energy conservation. Instead, it will affect the kinetic and potential energy wavefunctions. This boost, in turn, will give rise to a standing wave in the near vicinity of the gold surface, called the evanescent wave/field. The evanescent wave's intensity decreases exponentially in parallel and perpendicular to the gold's surface (range of detection sensitivity is within <200nm perpendicular and

<3.1μm parallel to the gold surface[108]). This drop-in intensity occurs as light propagates away from its incident point on the metal's surface. SPR devices are based on the sensitivity of this standing electromagnetic wave (evanescent wave) to variations in the refractive index of the dielectric medium above the gold surface (e.g., gas, fluid). Maxwell equations will assist in investigating why variations in charge distributions of the electron density cloud will cause changes in refracted light's angle ($\Delta\theta$).

Since light is the "data carrier" for our study, it is essential to grasp the interaction between light and matter before applying the concept to real-world problems. Maxwell developed a set of mathematical equations to affirm Faraday's hypothesis that changes in electrical field will induce a magnetic field, and changes in a magnetic field will induce an electrical field. The final Maxwell equation relates the changes in the magnetic field of an infinitesimal element of a closed-loop system to the current produced based on propagation space's electromagnetic permeability:

$$\int B.ds = \mu_0 I + \mu_0 \varepsilon_0 . \frac{d\varphi_E}{dt} \quad \text{(Equation 9)}$$

Where B is the magnitude of the magnetic field, μ_0 and ε_0 are the magnetic and electrical permeabilities of the space where the wave travels; I is the current, and φ_E is the electrical flux. Since the speed of the electromagnetic wave (V) is inversely proportional to the square root of both permeabilities (eq. 10), the finalized form for energy densities of the electrical and magnetic field is rearranged (eq. 11,12) (note that the contribution of the magnetic field can never be ignored in light's energy density measures).

$$V = \frac{1}{\sqrt{\mu_0 \varepsilon_0}} \quad \text{(Equation 10)}$$

$$U_E = \frac{\varepsilon_0 E^2}{2} \quad \text{(Equation 11)}$$

$U_B = \frac{B^2}{2\mu_0}$ (Equation 12)

Light has equal electrical and magnetic energy densities. Therefore, the total energy density of light's electromagnetic wave and the magnitude of light's electric field are:

$U_{Total} = U_E + U_B = \varepsilon_0 E^2$ (Equation 13)

$|E| = h.f$ (Equation 14)

Where h is the Planck's constant and f is the light's frequency. From eq. 13, it is seen that the total energy density of light is directly proportional to its electrical field's magnitude. This equation can also be written based on the magnetic field's (B) importance. However, our interest resides in the variations in the electrical field of the dielectric medium, hence the motivation for presenting the electrical component here.

When light enters a medium with a different dielectric constant, it refracts. A medium's dielectric constant (ε) is affected by the material properties of that medium (e.g., density) and environmental factors, such as temperature that can alter material properties. The changes in the medium's dielectric constant will define the refraction angle (θ) at which the light bends (refer to equation 4). On the other hand, the magnitude of the electrical field ($|E|$) component of light's electromagnetic wave is always the same across different mediums and perpendicular to the direction of light's travel (Figure 2A). As the dielectric constant of the medium changes, and because of the law of conservation of energy, while $|E|$ is kept constant, its x and y components (E_x, E_y) WILL change in the refracted light. The constant magnitude of the electric field in all mediums is why the refraction angle (θ) is different from the incident angle (why light bends!).

Earlier, we stated that the total internal reflection of light due to the Kretschman's configuration in SPR devices occurs to couple photons to plasmons. In assisting the

simplification of our excitable cell-SPR model, we can interpret the previous sentence another way. When a total internal reflection occurs, the second medium where the beam of light enters can be assumed as the initial medium (Figure 2A). Therefore, the primary medium from which light originally propagated is counted as the second medium, where light refracts and is detected. Therefore, in this paradigm light is originated in medium one and bends as it travels to medium two. The illustration in Figure 1 is used to describe the physiology of the phenomena driving the P-CeG signal. Recalling from the previous paragraph that θ of the refracted light changes with alterations of the medium's dielectric constant, ε. Most commercialized SPR devices detect $\Delta\theta$ and correlate it with variations in the small molecular constituent of the medium (analyte concentration). However, suppose charged particles are present in the medium (e.g., ions). In that case, they, in turn, will generate an electrical field, which, depending on the net particle charge, can oppose or agree with the direction of the incident light's electrical field. Depending on the direction of the ionically induced electrical field, the refracted light can bend away from or towards the normal to the plane of refraction. SPR has been used recently for monitoring cell-generated action potentials in excitable cells[61,62,109–113]. However, to the best of our knowledge, no correlation has been made between variations of ionic fluxes during an excitable cell's activity to the angle of refracted light.

Going back to the illustration in Figure 1, in developing our excitable cell-SPR model, we will assume the closed-loop of medium1/medium2 complex as the system for applying the law of energy conservation. Total energy at each medium encompasses potential (U) and kinetic (K) components and elements. In the first medium, where charged particles flow in and out, we consider the total energy to be a summation of the energies of

electron density cloud (U_1, K_1) and that of the cell membrane (U'_1, K'_1). Furthermore, the second medium receives the energy of the refracted light as its total energy (U_2). Thus, applying the law of conservation of energy, we have:

$$U_2 = U_1 + K_1 + U'_1 + K'_1 \quad \text{(Equation 15)}$$

The right and left sides of eq. 15 are counted as states one and two for conservation of energy calculations, respectively. The potential energy of the electron density cloud (U_1) for gold in eq. 15 is denoted as the first ionization energy. It is the ground state potential for valence electrons. It has five significant contributors: 1. nucleus-nucleus repulsion of gold atoms, 2. electron-nucleus attraction, 3. electron-electron repulsion, 4. electron self-repulsion, and 5. exchanged energy within the cloud. Gold's ionization energy is $1.4*10^{-18}$ joules, which is negligible in our model's assumption (U_1=0). K_1 is the kinetic energy of electrons in the electron density cloud of length L (eq. 6). Moreover, we assume a stationary fluid flow (K'_1=0), a net constant charge density for the electron gas (Q_1), and a net total charge value near the excitable cell's membrane (Q_2) due to ion fluxes, which are a constant r distance apart from each other. The electrical potential (U'_1) resulting from charge differences between Q1 and Q2 contribute to the refracted angle in medium 2. Hence, combining equations 6, 13, 14, and 15 and inputting initial boundary conditions, the charge alternations near the cells' membrane as a factor of the medium's dielectric constant change can be calculated.

$$\varepsilon(hf)^2 = \frac{\hbar^2 n^2 \pi^2}{2mL^2} + k\frac{Q_1 Q_2}{r} \quad \text{(Equation 16)}$$

k is Coulomb's constant and ε is the dielectric of medium one after ions influx, which is empirically extracted for our model employing eq. 4. Due to Gauss's law, Q_1, or the total charge enclosed within volume v of the electron, can be estimated through eq. 17 and 18.

$$\Phi_E = 4\pi d^2|E| \quad \text{(Equation 17)}$$

$$Q_1 = -3.52 * 10^{-20}|E|\varepsilon \quad \text{(Equation 18)}$$

d is the radius of the electron cloud (i.e., Bohr radius, 0.529 Å) and the negative sign denotes the nature of the electron density cloud's charge. Assuming a constant distance between the electron cloud and cell membrane (r), and Č being assigned to all constants in the equation, we will reach:

$$\check{C} = \frac{r}{3.52*10^{-20}k} \quad \text{(Equation 19)}$$

$$Q_2 = \check{C}\frac{\frac{\hbar^2 n^2 \pi^2}{2mL^2} - \varepsilon(hf)^2}{\varepsilon hf} \quad \text{(Equation 20)}$$

Q_2 (coulombs) is the total net charge near the cell membrane at each time; Q_2 will show an absolute value for charge distribution near the cell membrane during an action potential event. In our study, equation twenty will be used for observing charge variations near the cell membrane as the CMs contract.

2.2.2 Cardiomyocyte Syncytium Electrophysiology

Besides the biological elaboration for CMs introduced in chapter one and following up on the previously introduced excitable cell-SPR model, more in-depth knowledge of cardiac cells' ion channels responsible for action potential generation and conduction is required. The illustration in Figure 2B shows the changes in membrane potential of a CM, tracked by its contraction phase, which will be explained thoroughly in the following few paragraphs.

Phase zero (Ph. 0) is depolarization, where voltage-gated sodium channels (e.g., Nav1.5) open and allow the fast inward current of Na^+ ions into the cell. A potential of -70mV defines the threshold for opening the fast-opening sodium channels. It also marks

the proper functionality of calcium/sodium exchanger and sodium/potassium pumps (e.g., HCN4) for maintaining the "Funny Currents" (I_f)[114,115]. HCN4, also known as the potassium/sodium hyperpolarization-activated cyclic nucleotide-gated channel, is mainly expressed in human heart pacemaker cells (e.g., atrioventricular, or sinoatrial cells of the human heart). HCN4 is dominantly responsible for maintaining the hyperpolarization of pacemaker cells, which are accountable for action potential propagation through the heart[116]. HCN4 and other proteins responsible for maintaining the funny currents in pacemaker cells of the heart are almost half the size of voltage-gated Na^+ channels, such as Nav1.5 (compare 120kDa and 220kDa, respectively). Therefore, a smaller number of ions (i.e., less amount of charge) will be exchanged through these hyperpolarization maintaining channels. This small quantifiable (~2mV) charge variation during a hyperpolarization event is a hallmark of spontaneous action potential production in CMs.

Interestingly, in an adult heart, expression of HCN4 is mainly found in nodal cells, partially found in AV (atrioventricular) cells, and is absent in ventricular CMs (VCMs)[106,117]. This distribution of HCN4 protein suggests that a spontaneous contractile behavior from ventricular CMs is implausible unless joint with pacemaker cells or active electrical stimulation. On the other hand, HCN4 is well expressed in stem cell derived CMs, which advocates for the developmental aspect of these cells to be taken into account in ALL cardiac cell studies.

Phase one (Ph. 1), immediately followed by phase two (Ph. 2), is initiated as the voltage-gated K^+ channels open and allow K^+ to leave the cell, decreasing the membrane potential. At a potential of +5mV, Ph. 2 starts, and the slow opening Ca^{2+} channels, or L-type Ca^{2+} channels open, and let Ca^{2+} ions enter the cell, balancing out the K^+ ions leaving

the cell. The 300ms plateau blueprint of the cardiac action potential is developed due to L-type Ca^{2+} channels and voltage-gated K^{+} channels activities. This phase also communicates the event of Calcium-Induced-Calcium-Release (CICR) from the sarcoplasmic reticulum (SR) of CMs[118]. CICR is a downstream effect of Ca^{2+} ions entering the cell through t-tubules. As extracellular Ca^{2+} enters the cell, it signals the SR to deplete Ca^{2+} ions. As a result, the SR is "draped" over the cell's contractile proteins (e.g., actin and myosin) for efficient Ca^{2+} transfer; the rapid binding of Ca^{2+} produced through CICR to these proteins initiates cellular contraction.

Phase three (Ph. 3) of the cardiac action potential, also known as repolarization, is a sharp decrease in membrane potential due to increased permeability to K^{+} ions through voltage-gated K^{+} channels, where the membrane potential reaches its -90mV potential. Phase four (Ph. 4), the refractory period, is the last before the next cycle recurs. These abovementioned phases complete an action potential of a mature cardiac cell. Their correlation to the electrocardiogram complexes (e.g., ST, QRS) is the basis for diagnosing cardiovascular diseases. It should be noted that the ion channels mentioned above only make up for portions of more than 500 membrane proteins on a single adult CM[117,119]. Out of all CMs membrane proteins, 40% are cardio-specific, amongst which are the non-voltage gated ion channels such as acid-sensitive ion channels (ASICs) and mechanosensitive channels, which are beyond the necessary membrane proteins needed to be considered for the scope of this dissertation.

The following methodology for empirical studies was pursued to investigate further the applicability of SPR in monitoring such detailed physiological phenomena from live cardiac cells.

2.3 Methodology

The experimental design for this investigation consists of 1. gold sensor surface modifications, 2. fabrication of PDMS cell concentrators for the selective spatial distribution of CMs on gold sensors, and 3. heart collection and cell culture methods. In addition, all procedures necessary for efficient setup and maintenance of a microfluidic-based SPR device, before and after experimentation, are discussed. All experimental procedures and animal care and use in this study are approved by the Institutional Animal Care and Use Committee (IACUC) at Florida International University (Approval No. 20-038-AM01). The entire methodology process is illustrated in Figure 3A-D.

2.3.1 Gold Sensor Preparation Before Cell Culture

Before any surface treatment, all sensors and devices must be cleaned of any residue and sterilized. The gold sensors used in this study are reusable. However, the used sensors require a different cleaning process than the new sensors. Used sensors for cell culture are bleached for 5 minutes using a 10% v/v of sodium hypochlorite, followed by two hours submerging in acetone, 30-minute ultrasound sonication, oxygen plasma treatment, and a final 100% ethanol and deionized (DI) water wash. New or old sensors are then submerged in 70% ethanol for 15 minutes, Nitrogen (N2) dried, and UV-sterilized for 15 minutes before any surface treatments. Sensors are then washed with Ca^{2+}-free buffer solution (HBSS) under a sterile hood. An essential step in high yield culture and viability of cells on-chip is the last wash step. The wash step removes any residue from the sterilization step, including traces of ethanol, affecting the surface modifications by inhibiting a successful binding between the protein and sensor.

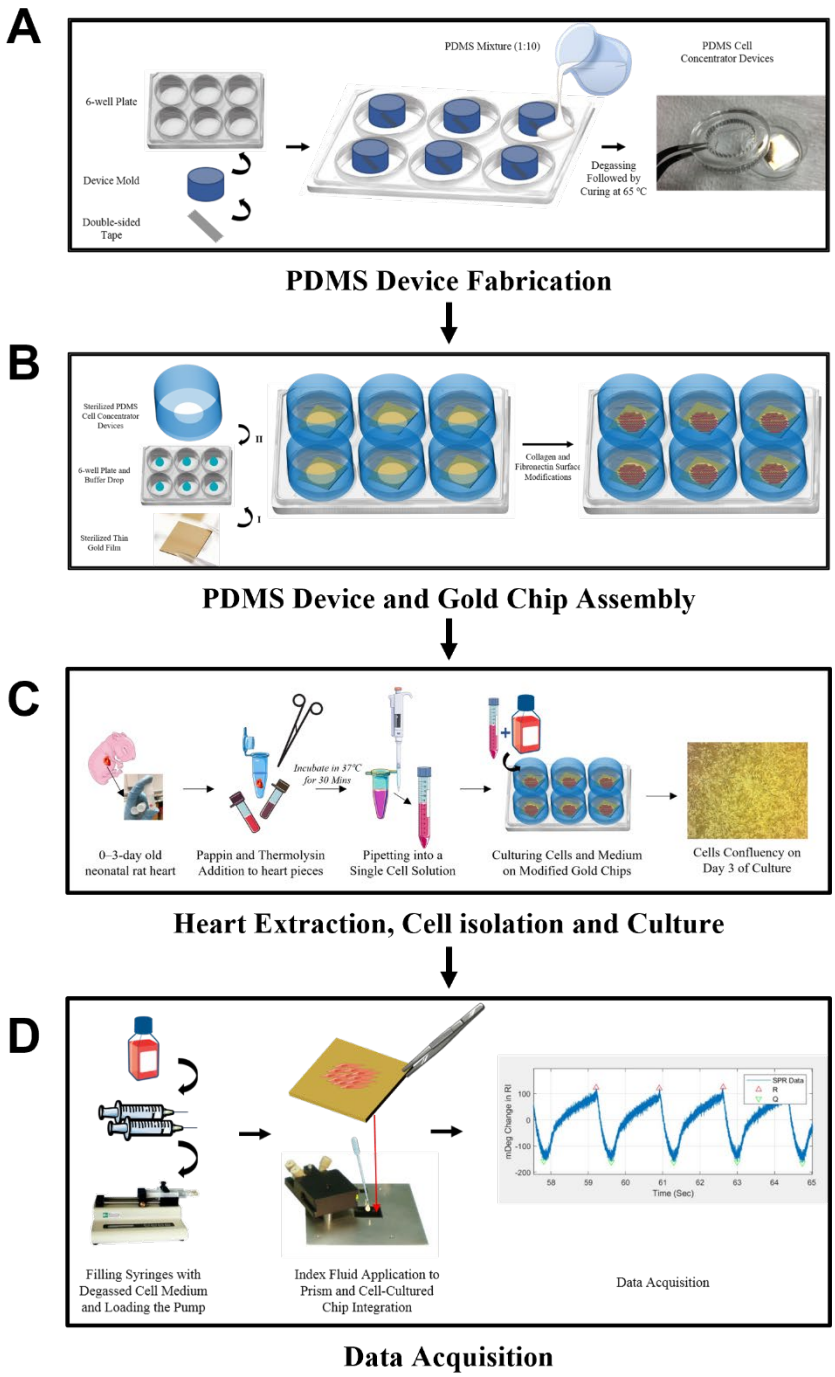

Figure 3. Flowchart of the experimental protocol. A. Illustration of PDMS cell concentrator devices fabrication (note that sterilization step of gold sensors and PDMS devices is not depicted here). B. Assembly steps for integrating devices to gold sensors are shown. Collagen and fibronectin surface modifications are followed by device integration. Finally, sensors are ready for culture. C. CM isolation protocol from neonatal rat hearts is depicted in this section. Cells are maintained for seven days before getting tested with SPR. D. Experimental setup of monitoring contraction profile of CMs on gold sensors using SPR is illustrated.

Sensor surface modification

Gold has a substantially higher Young's modulus than biological substrates such as collagen or fibronectin (~ 3 orders of magnitude higher), making it a less suitable environment for myocyte attachment and functionality. Therefore, to explore the effects of different substrates on CMs development and viability, we cultured isolated CMs from neonatal rat hearts on substrates of 1. pure gold sensors, 2. gold treated with fibronectin, 3. gold treated with collagen, and 4. gold treated with gelatin.

Sensor surfaces were initially washed after the sterilization protocol three times with phosphate buffer saline (PBS). Then, fibronectin surface modification was carried out by coating the gold sensor surfaces with a 1:100 diluted fibronectin (Sigma Aldrich) solution, incubated on a shaker for 1 hour at 37°C, and left to dry for 1 hour before cell seeding. Gelatin surface modification was done using a sterile 2% (w/v) gelatin solution (Sigma-Aldrich). Ten microliters of gelatin solution per square centimeter of culture plate were used to cover the gold sensors and left to dry in a sterile biological hood at room temperature for two hours before seeding cells. For sensors treated with collagen, type I collagen from a rat tail (Sigma-Aldrich) was diluted in PBS and 0.1% (w/v) acetic acid. Sensor surfaces were coated with the minimum level of collagen solution and left overnight at 4°C. The next day, sensors were allowed to dry at room temperature before seeding cells under a sterile biosafety hood.

2.3.2 PDMS Cell Concentrator Devices

Polydimethylsiloxane (PDMS) cell concentrators avoid the cells slipping off the surface to the edge of the sensor and maintain their population in the center (at the focal

reading points of our SPR device). Polydimethylsiloxane (PDMS) cell concentrators were developed to be inserted on top of surface-treated gold sensors before cell culture.

Device fabrication

Devices are fabricated through the following steps, as illustrated in Figure 3A: 1. Using a FabPro 3000 SLA printer, a device mold is designed and printed. 2. The mold is then glued to the center of a well in a 6-well plate, using double-sided tape. 3. The surface of each well with the mold integrated is sprayed with mold release spray. 4. A 1:10 ratio of curing agent/PDMS is used to create the concentrator devices. The PDMS mixture is poured into the prepared molds and is transferred to a level vacuum chamber for degassing. It is then cured for 2 hours at 65ºC or until 95% cured (the adhesive property of a 95% cured PDMS can help with a sealed integration to the 6-well plates later before cell culture). 5. After being cured, devices are removed from their mold, sterilized with 70% ethanol and UV exposure, and integrated into gold sensors in well plates for experiments. It is recommended that the PDMS devices be incubated in a 10% Bovine Serum Albumin (BSA) for 1 hour at room temperature before integrating them onto sensors. This step will limit the nonselective attachment of cells to the walls of the PDMS device, concentrating them at the bottom center and on SPR's reading points.

2.3.3 Primary Cardiac Cell Isolation

Here we outline a technique adapted from a Fischer Scientific CM Isolation Protocol[120] with slight adjustments for fast and highly reproducible CM isolation from neonatal rats 0-3 days old (Figure 3C*)*.

Animal model and breeding

Long Evans rats aged 8-36 weeks (Charles River) are housed in standard cages at a 12h-12h light-dark cycle with free access to food and water. Each male is paired with two female rats and alternates between female groups every two weeks. Pregnant females give birth to 8-15 neonatal rats, 7-10 days after the male's transfer (given conceiving has occurred). If the adult rats are close to retiring, the required substitute number of animals are kept from the neonatal rats. The kept neonates will stay with the mom for two weeks before moving for breeding purposes. Any other neonatal rats aged 0-3 days old are then collected for heart extraction. We recommend using the hearts on the earlier days of their birth (0 and 1, rather than 2 and 3), which corresponds to the higher viability of isolated cells due to our observations (such observation has not been quantified.)

Heart collection and CM isolation

All necessary solutions and sensor surface modifications are prepared before being used for heart extractions. It is essential to limit the process of heart extraction to 2 hours or less using this protocol to achieve 65% and higher cell viability post isolation. 1. Complete cell media solution is prepared with kit-provided DMEM, 10% FBS, and 1% penicillin-streptomycin. 2. All dissection instruments are sterilized using 70% ethanol before organ extraction. 3. Neonatal rats (ages 0-3 days old) are transferred to the euthanization station. Animal's chest is sprayed with 70% ethanol. 4. Using surgical scissors, the animal is rapidly decapitated. 5. A median sternotomy opens the animal's chest cavity and sternum. The aorta is then cut using smaller scissors to release the heart, then removed using forceps. 6. Each dissected heart is put into a separate microcentrifuge tube, immediately adding 0.5mL of ice-cold HBSS. The heart-containing tubes are kept on ice until use. 7. Animal carcasses are then disposed of in a biohazard bag.

Culture conditions and maintenance

A detailed procedure of cell isolation from extracted hearts is presented in the protocol provided by Thermo Fischer Scientific (Pub. Part No. 2162550.0). Neonatal rat CMs were isolated from newborn 0–3-day old rat pups following this protocol. Briefly: 1. Each heart is transferred into a 2ml tube and washed twice with 500µL of ice-cold HBSS. This wash step removes any fat and attached blood vessels from the hearts. 2. Hearts are then trimmed in each tube with surgical scissors into small pieces (1–3mm^3). 3. The cardiac tissue is then digested by adding 0.2mL papain and 10µL thermolysin to each tube. 4. Tubes containing hearts and enzymes are incubated for 35 minutes in a 37°C and 5% CO_2 incubator. 5. Digested tissue is removed from the incubator and immediately washed twice with the addition of 500µL ice-cold HBSS to stop the enzyme activity. 6. 500µL of complete DMEM warmed to 37°C is added to each tube. 7. Tissue is then broken down to its cellular constituents using a 1000µL pipette into a homogeneous single cell solution. 8. All microtubes containing 2mL of single-cell solution are combined in a 50mL conical tube to determine cell concentration and viability. 9. Using a hemocytometer, a mix of 1:1 ratio of 25µL trypan blue with cell solution is counted for determining cell concentration (cell/mL) and viability. 10. Isolated cells are then cultured on each prepared SPR gold sensor, fixed in 6-well plates with a density of 250,000 cells.cm^{-2}. Enough complete DMEM for primary cell isolation is added to raise the culture volume to the well's media capacity (0.8-1mL for PDMS opening wells, equivalent to a 12-well plate). 11. After 24 hours, the medium is substituted with complete DMEM containing CM growth supplements for CM purification over fibroblasts and endothelial cells. After this, the medium is changed every three days for cell function maintenance.

2.3.4 Preparations For Excitable Cell Integrated SPR Experiment

It is highly recommended that the SPR device is calibrated at least once every six months, using sequential injections of ethanol dilutions in DI water (e.g., serial injections of 1%, 0.5%, 0.25%, 0.125%, and 0.0625% ethanol)[121]. We must also emphasize cleaning the device's microtubing after experiments to avoid future tube clogging and a failed experiment.

As the experiments conducted include housing of live cells for the duration of the investigation in an uncontrolled environment (e.g., 25°C as compared to 37°C temperature), considerations should be given in the data analysis for the possible effects of such variants. Temperature is known to drastically impact a cardiac cell's action potential duration through modification of their calcium ion channels' permeability and gating property. Also, the conductance of Na^+ ion channels is known to increase steeply with temperature increase[122–124]. Variations in physiological pH are also highly alarming for cell culture conditions. Non-physiological pH for cellular studies (pH<7.0-7.2 and pH>7.8) might inhibit the peak amplitude of voltage-dependent potassium channels, affecting the depolarization state of the action potential of excitable cells[125]. Our BI2000 device does not allow for physiological temperature control of cells. Consequently, we have validated our results with literature that has reported contraction data acquired at room temperature.

In this unit, successful contraction profile acquisition from spontaneously beating CMs on gold sensors using SPR is presented. The experiment day differs depending on the source of isolated cardiac cells. For example, we observed day 7 of culture being a suitable experiment day, due to CM maturity, for neonatal rat primary isolated CMs. However, in cases of induced pluripotent stem cell-derived cardiomyocytes (iPSC-CMs), the maturity

of differentiated cells may take up to 12-14 days[126], so one must consider each specific cell line's maturation properties. Data extraction, processing, and analysis are briefly mentioned in this section; we will have a much-detailed elaboration of data processing in chapter 3. Thus, the protocol depicted here applies to most commercial or lab-made SPR devices for investigating CM activity under chemically stimulated conditions and is not limited to our commercial device.

Preparations before data acquisition

One day before the experiment, the cell medium to be used as running buffer is loaded into 5mL injection syringes and kept in the 5% CO2 incubator overnight for maintaining a pH-balanced solution. The presence of contractile CMs on-chip is validated on each sensor using microscopy. All non-viable sensors, such as non-connected CM clusters, low CM culture density, and non-synchronized contraction across cells, are removed from the selected batch for the experiment. SPR tubing is tested for leak-free flow, clogs in microtubing and injection port, and bubble-free buffer flow through the system. On experiment day (as followed in Figure 3D*)*, 1. The device is turned on for warm-up. 2. A temporal resolution of 1000Hz sampling rate is selected in data acquisition software, previously recommended for sensitive contraction analysis of cardiac cells in comparison with 100Hz and 10Hz sampling rate[127]. 3. Flow pump is then connected to the device, and media-filled syringes stored in the incubator are immediately coupled to the injector heads (shown in Figure 3D). The flow rate is set to 50μL/min for experiment initiation. 4. One CM-cultured gold sensor is removed from the incubator as the flow is set up and the software runs. The non-gold surface of the sensor is dried gently using a nitrogen (N_2) gun (Cleanroom World, CO), and the sensor is immediately inserted on the device's

prism using matching index fluid. 5. The microfluidic module is then integrated and sealed on top of the cell-cultured gold sensor, and cell medium flow is instantly initiated using the injection pump at 50μL/min. 6. After a few minutes and as soon as the medium fills all microtubing and contacts the cells on-chip, flow speed is changed to 10μL/min, and recordings are initiated. 7. The baseline is allowed to stabilize for 10 minutes. Usually, after 2-5 minutes, a cyclic time-series signal is observed. 8. Using built-in software tools, the amplitude of the cycles is manually examined. Suppose the signal's amplitude is lower than ten mDeg response units (RU). In that case, the experiment is terminated since we observed that data recorded with signal amplitudes lower than ten mDeg are unreliable for analysis. More elaboration will be presented in the results section.

2.4 Results and Discussion

A healthy mammalian cardiac cell is a complex organism defined by its four main properties: Rhythmicity, Excitability, Conductivity, and Contractility. Each of these properties can be exploited solely or simultaneously *in-vitro* using gold standard techniques such as fluorescent microscopy[128], patch clamping[129], electrochemistry[54], and MEMS-integrated microfluidic devices[107]. We sought to explore the feasibility of SPR for recording these major properties of excitable cells such as CMs.

2.4.1 Surface Modification Characterization

To ensure that our gold sensors provided a suitable platform for CMs' signal transduction, we sought to analyze their morphology and particular constructs using immunofluorescent staining. CMs were isolated from neonatal rat hearts and were cultured for seven days. Cells were then stained for their sarcomeric α-actinin, which is associated with cardiac cell contractility; Connexin-43, a gap junction protein that indicates the cells'

maturity of electrical coupling between electrical adjacent cells; and DAPI for cell nuclei. Images were taken using a Nikon Eclipse confocal microscope. Figure 4A shows the brightfield image of the contracting cells on days 1, 3, and 7 of culture. Figure 4B shows different staining for CMs cultured on fibronectin, collagen, gelatin, and bare gold sensors. Our observations show that between all the groups, sensors coated with fibronectin show the best results in terms of cell density (0.3 nuclei per mm^2 for fibronectin compared with 0.16 nuclei per mm^2 for collagen, 0.08 nuclei per mm^2 for gelatin, and 0.07 nuclei per mm^2 for bare gold), cell morphology and area (more towards rod-shaped rather than rounded) and presence of massive sarcomeric striations in comparison with their alternative surface treatments. Immunofluorostaining suggests the formation of a well-distributed CMs monolayer.

Higher expression of connexin-43 in collagen-coated gold sensors (Figure 4C) reveals a better environment for cells to communicate and transmit their electrical signals, which will also result in a more synchronized and stronger beat. The non-uniform presence of connexin-43 across different cell clusters within one substrate might be due to: 1. damaged cells after CM extraction from neonatal rat hearts, or 2. a disrupted network connection amongst the cultured cells as a result of non-ideal *in-vitro* culture. The nuclei count suggests fibronectin is a more suitable substrate for CM culture on gold surfaces concerning developing a monolayer (Figure 4D*).* The higher nuclei count for fibronectin-treated sensors might be due to fibronectin's interaction with integrins on CMs' plasma membrane, spreading out the cells across the sensor surface rather than forming cellular clusters. We have concluded that a surface modification of collagen, fibronectin, or both, will result in a more viable cardiac cell culture on gold sensors[56]. Collagen surface

modification is known to provide a softer surface with lower Young's Modulus (50 kPa[130]) compared to gold, which is favorable for CMs specifically[131,132]. Fibronectin surface modification results in a network assembly of cardiac cells in a monolayer of culture. Fibronectin binds to membrane integrins of cardiac cells, which assists with distributing the cells across a monolayer on the surface, avoiding making clusters. A network connection of cardiac cells will provide a more homogenous signal output, contributing to more accurate signal acquisition.

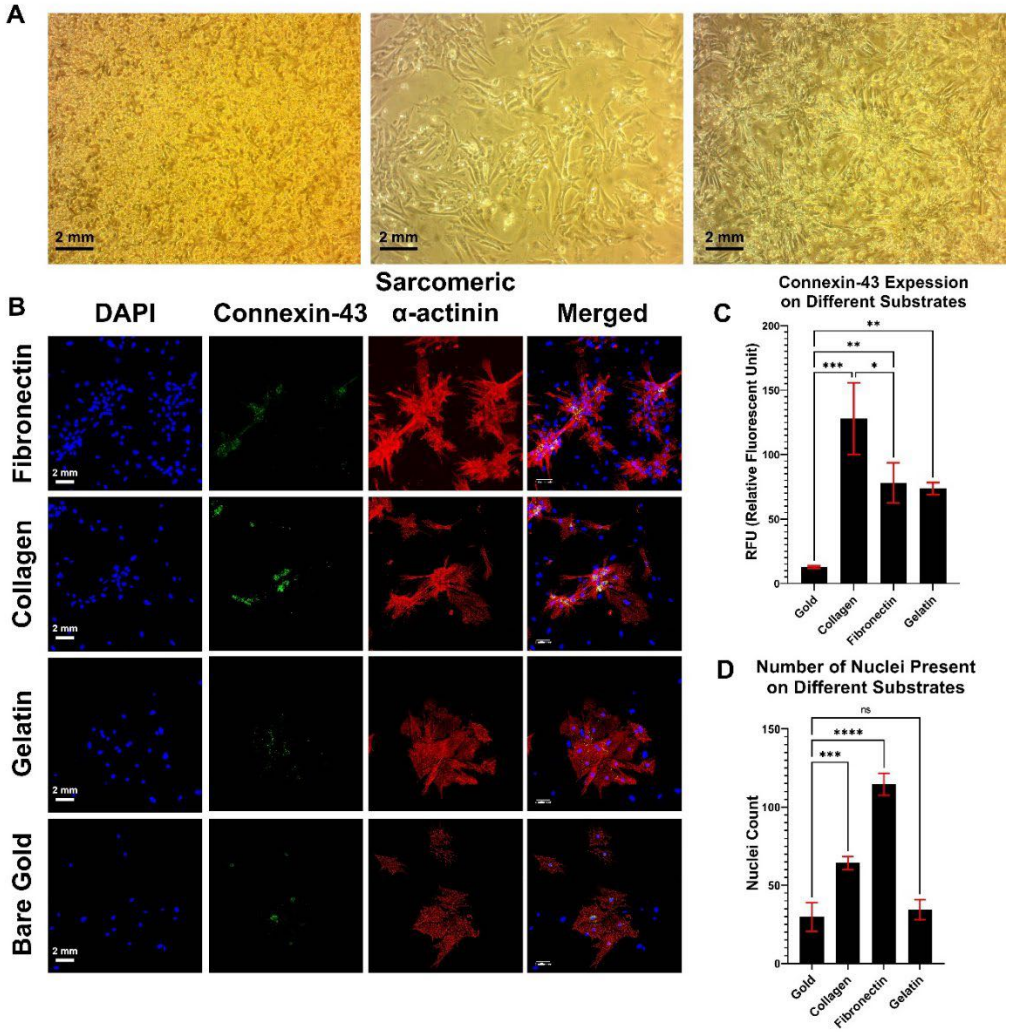

Figure 4. Cardiac cell culture on gold sensors with various surface treatments. A. brightfield images of CMs isolated from neonatal rat hearts on days 1, 3, and 7 of culture, respectively, are shown (bar shows 2 mm). B. immunofluorescent analysis of cardiac cells cultured on fibronectin, collagen, and gelatin treated gold sensors compared with a bare gold sensor. CMs are tested for contractile features, sarcomeric alpha-actinin, and a

membrane protein, connexin-43. C. Image analysis shows a higher connexin-43 presence for collagen treated sensors (n=3 sensors, average data is reported as mean ± std: 1-way ANOVA, $p<0.0002$). Tukey's multiple comparisons test shows the significance of conexxin-43 expression with respect to gold sensor to be: (***) for collagen, and (**) for fibronectin and gelatin. A significant difference of (*) was observed between collagen and fibronectin treated sensors. D. higher nuclei count across cells cultured on fibronectin-treated gold sensors in comparison with other surface treatments (n=3 sensors, Average data is reported as mean ± std:1-way ANOVA, $p<0.0001$). Tukey's multiple comparisons test shows the significance of nuclei presence with respect to gold sensor to be: (***) for collagen, and (****) for fibronectin.

2.4.2 Understanding the Obtained Signals Using the Mathematical Model

The output of SPR's real-time monitoring of CMs is depicted in mDeg changes in refractive angle. Therefore, understanding the source of the produced signal is vital for accurate and comprehensive data analysis.

We experimented with twelve CM-cultured gold sensors to explore the signal's source. A sample size of 12 gold sensors was tested for signal variability in excitable cells. Cells were tested for 10 minutes (blue area in Figure 5A) initially, during which the signal's wondering baseline was stabilized. After the baseline stabilized, recordings from cells continued to a maximum 45-minute duration, depending on the target of the study. The time block after stabilization and before any signal perturbations (e.g., drug injections) is denoted as the calibration section (orange area in Figure 5B). Although a rhythmic signal was also observed in the stabilization section, all data collected for analysis was extracted from the calibration section. The signal from the calibration section is transferred to MATLAB, where it is sectioned in 100-second intervals. Primary signal features of amplitude, full width half maximum (FWHM), beating rate, and inter-beat-interval were extracted as the mean and standard deviation for a total number of n peaks in each 100-second interval. Each sensor had six intervals collected from its calibration section (total of 10 minutes). A random selection of peaks from all intervals within each sensor was used as data points. A sample size of n=41 peaks was selected from all intervals for each sensor.

Each dot in Figure 5B represents a single peak value for each sensor, marked with numerical labels on the x-axis.

A significant variation in signal amplitude across different sensors was an alarming observation, which encouraged the expansion of our experimental data ($10 < \text{Amplitude} < 300$, $n=12$, $p<0.0001$ using a non-parametric Kruskal-Wallis test, in Figure 5B). This variability in amplitude is most likely explained by re-using sensors. Despite a thorough cleaning procedure for removing all previous chemical and biological residues on gold sensors, reusing the sensor is not recommended. Another explanation might be the presence of multiple types of CMs (e.g., ventricular, atrial, nodal) cultured on the sensor because of the isolation and culture protocol. Although the protocol includes a growth supplement for the purification of CMs over fibroblasts, it does not distinguish between CMs of different origins (e.g., ventricular, or nodal). Therefore, three further experiments were designed and conducted to explore the effect of cell variability. The cell culture protocol was adjusted to extract CMs from neonatal rat heart ventricles instead of the entire organ. To our surprise, no periodic signal was received from ventricular CMs. Recalling from developmental biology of the heart and as discussed earlier, lesser amounts of HCN4 are expressed in ventricular CMs of developed hearts than that of the developing ones in gestational period[117]. This protein expression will result in ventricular CMs losing their spontaneous contractibility and depend on the action potential signal sent from the SA node for contraction. Meanwhile, the CMs of nodal origin do express HCN4 protein on their membrane, which allows for their spontaneous contraction. Therefore, all experiments were continued using the original protocol for digestion of the entire heart, rather than

excising its ventricles. Nevertheless, a more in-depth analysis is required to confirm whether the signal is coming from different types of cells within the heart, discussed later.

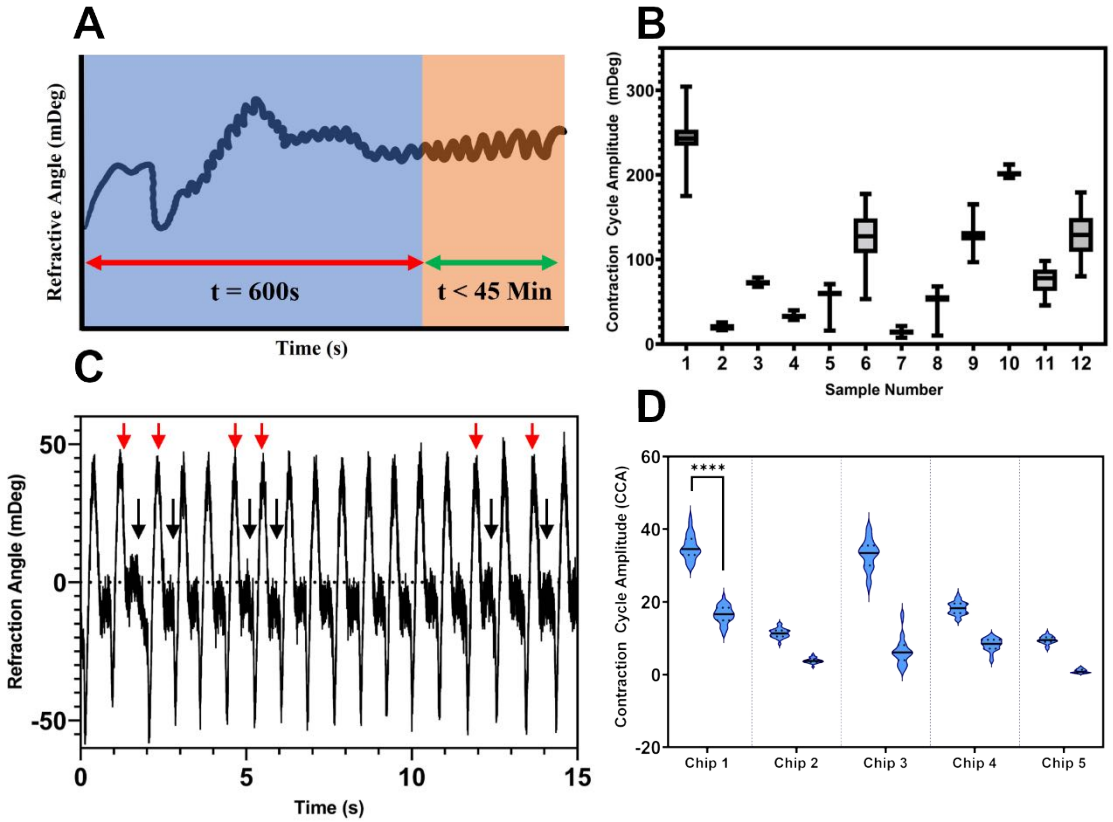

Figure 5. Preliminary observations of the signal. A) Blue is the wondering baseline before stabilization. Orange is the initiation of the calibration section, where the signal is selected for analysis. B) Box plots represent the amplitude distribution of a randomly selected 100-second epoch extracted from the sensor (sample number) n. C) Double-peak signal sample. Black arrows mark the location of a few of the secondary peaks, while the red ones mark the primary peaks. D) Significant differences between primary and secondary peak amplitudes of double peak samples were observed across all five sensors. (n=5, average data is reported as mean ± std: one sample Wilcoxon test, $p<0.0001$, 95% CI). Results show a significant difference between signal's primary and secondary peaks for all five sensors to be (****).

Furthermore, a distinctive double-peak trend was observed in the signals obtained from five separate sample sensors than those presented in Figure 5B, where a significant difference was observed between the first and the second peak in each signal (Figure 5C-D). First, the signal source is vital in understanding the double peak. Second, the model presented here must also consider that force of contraction might affect the signal obtained from the CMs (see Figure 2C). Although microscopic in SPR, force of contraction has an

elemental turbulence kinetic energy (TKE) that should be included for a complete comprehensive mathematical model of energy conservation. For the scope of this dissertation, the effect of such turbulences is consciously ignored in developing the model. However, the importance of including the TKE of the disturbed medium due to cell contraction in future works must be emphasized. Third, the second peak in the SPR signal can also be a marker of early after depolarization (EAD), which is a well-known marker of arrhythmia in cardiomcyoytes[133]. Lastly, the effect of calcium-induced calcium release (CICR) from the sarcoplasmic reticulum of CMs might serve as a cause to this secondary peak, which is unlikely based on the fact that CICR occurs within the cytosol and might not affect the sensitive range of evanescent field's detection[118].

From the analysis of another twenty CM-cultured sensors, signals were categorized based on their peak amplitudes, into tall (Amp>100 mDeg, 129.37 ± 10.92 mDeg, n=5), medium (25<Amp<70 mDeg, 58.73 ± 8.11 mDeg, n=11), and short (10<Amp<15 mDeg, 14.23± 3.99 mDeg, n=4) amplitude signals. All tall peaks were recorded from new sensors, confirming that sensor reusability is not recommended to achieve the best signal output. Also, as signal reproducibility on new sensors is highly efficient, it is recommended that the complete set of data points be extracted from excitable cells cultured on new sensors for future experiments. Moreover, we observed a scattered data distribution amongst the FWHM obtained from reused sensors. Signals with amplitude above 100mDeg have the most stable signal parameters (e.g., amplitude, FWHM) across different sensors. Although the shape of medium and short amplitude signal periods was consistent across different sensors, their FWHM changed from sensor to sensor. While excessive biological and chemical residues from previous experiments can affect the signal amplitude, the FWHM,

representing action potential/contraction duration's variability, might suggest other possible causes. As mentioned before, because our isolation protocol consists of digesting a whole heart, the presence of different types of CMs with different origins of development on the sensor is highly possible.

The mathematical model of excitable cell-SPR using the charge-angle correlation function (equation 20) depicts the number of charge variations near the cell membrane as a point charge distribution. We have overlayed mathematical values of charge variations near the cell membrane of CMs (solid red line Figure 6) and corresponding three periods of a sample signal recorded from SPR in mDeg (dotted blue line in Figure 6) to see event correspondence between refracted angle light variation and charge distributions. It is noticeable that the events of the mathematical model line up well with locations of fast-acting voltage-gated channel activities, where the most ion flux occurs (as is shown in Figure 6 with arrows). The shaded area in Figure 6 shows half of a contraction period. A zoom-in graph of this half-period is extended from the shaded block in Figure 6. The first spike in charge variation might relate to fast opening Na^+ channels in depolarization. On the other hand, the second spike may indicate the CICR stage of CM action potential and contraction, or in the case of an EAD, it might be the opening of fast opening Na^+ channels in an early afterdepolarization effect. Manipulating ion channels' activity using inhibitor or promotor chemicals can shed more light on developing the correct understanding of each event's causes.

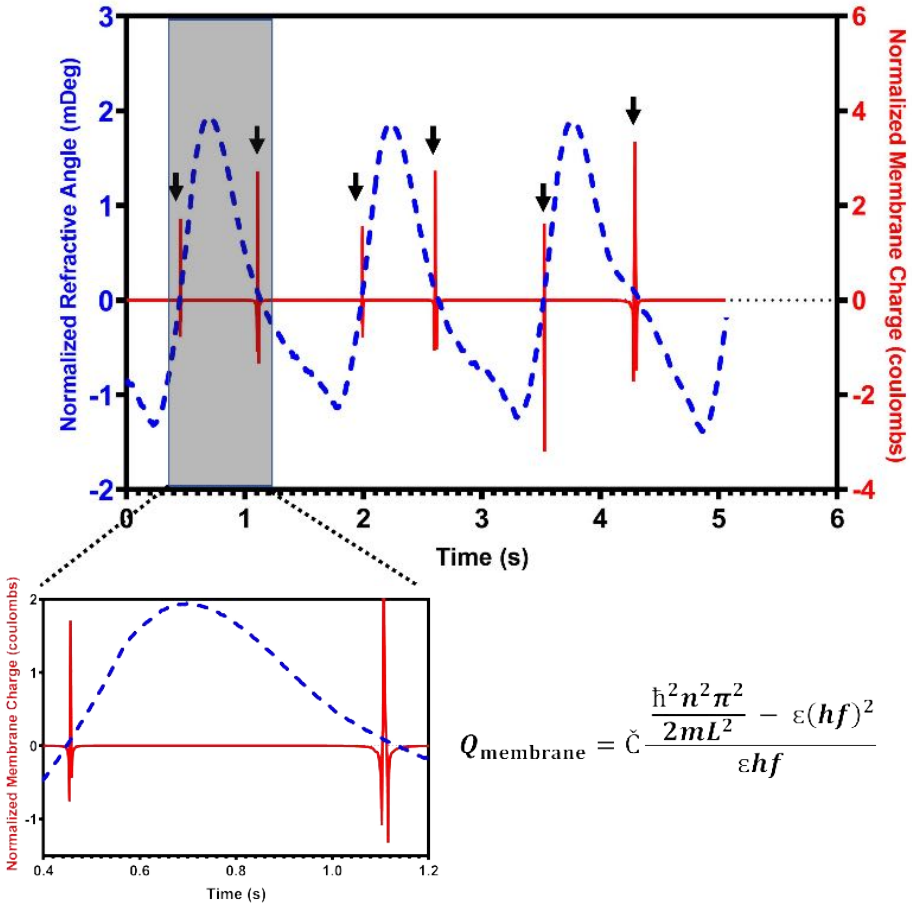

Figure 6. Computed charge variation near CM plasma membrane. The blue dotted line is the normalized contraction signal of three periods from tall amplitudes plotted on the left y-axis. The red line shows a simulated signal from its corresponding values from the mathematical model shown below the graph (Eq. 20).

2.4.3 Effect of Flow Rate on Cell Behavior and Signal Profile

A microfluidic module is provided in the BI2000 SPR device, which allows the dynamic flow of media on top of the cell-cultured gold sensors. The pump, which drives the fluid flow, can be adjusted to provide different flow rates depending on the experimental design. We sought to explore the effect of different rates of medium flow on signal acquisition from beating cells on-chip. Several researchers have used flow rates of 10-50µL/min for best molecular interaction response, giving the injected chemicals enough time to react with their cellular targets on the sensor for more accurate kinetic

response[102,134–136]. As mentioned in the previous section, a higher flow is associated with higher fluid speed. The fluid velocity will affect the kinetic energy of redistributing microscopic fluid filled pockets between the cell membrane and sensor surface. We have shown in chapter two that this kinetic energy will contribute to the total energy loss or gain of the refracted light in SPR, changing the light's angle of refraction. The turbulence kinetic energy of the medium moving between cells and the sensor's surface (see Figure 2C) is proportional to the square of the fluid's velocity. Therefore, an optimized flow rate must be established for future experiments to avoid the effect of fluid speed interfering with signal output. We must also consider the flow that provides minimal stress to the cells while adequately providing nutrients and oxygen. CMs are very sensitive to any external stress, including those of a mechanical source; hence are shielded from direct contact with turbulent physiological blood flow through several vascular lumens of the blood vessels body[137].

To have the cells in their most suitable environment, initially, 37ºC media was flown over cells continuously. Temperature is known to have a drastic effect on the action potential duration of cardiac cells through disrupting the permeability and gating property of their calcium ion channels; conductance of Na ion channels is also known to increase steeply with temperature increase[122–124]. Later, we discovered that due to the length of micro tubing for media delivery to cells, a rapid thermal dissipation occurs from the tube (100µm in diameter and 50cm long). This fast dissipation of the medium's heat implied that warming the flow buffer in advance is unhelpful. Therefore, all experiments were conducted with a medium at room temperature.

Furthermore, baseline stabilization took longer while using heated solutions as flow buffer instead of room temperature buffer. Recall that the refractive index of material changes with a change in temperature resulting in a different angle of refraction. More specifically, in liquids like DMEM, which contains several amino acids, the temperature change will primarily affect the liquid's density, leading to θ alterations. As a result of the fast drop in temperature and DMEM's constituents, we saw a drifting baseline in the signal of experiments done with warmed DMEM. Therefore, we conducted the rest of the experiments with room temperature medium (25 °C), and data gathered is compared to that of the cells tested under room temperature conditions and not typical physiological temperature. Seven different flow rates (2, 5, 7, 10, 20, 30, and 40μL/min) were used. These flow rates are well-known in SPR experimental designs for molecular binding studies or for administering the most negligible shear stress to cells in drug analysis[28,34,138,139].

Data points are selected from a100-second interval from each sensor and correlated to each flow rate. A sample size of n=8 CM-cultured gold sensors was tested to compare amplitude, FWHM and signal-to-noise ratio, due to different flow rates (2, 5, and 7μL/min). Results are shown in Figure 7. No significant differences were observed in signal features across different flow rates of 2, 5, and 7μL/min (Figure 7A). The high variations in data (large standard deviations) are likely due to the sensor-to-sensor variability. A sample signal collected after 2, 5, and 7μL/min (black, blue, turquoise) are shown in Figure 7B. The slight difference in signal amplitude of the sensor shown in Figure 7B, related to flow rates of 2, 5, and 7μL/min (271.54±15.77, 238.85±20.37, 210.53±10.70, respectively; n=62), is negligible as is seen in the graph. However, the variation in beating rate with different flow rates is unlikely to be linked to the variations in flow. The beating

rate is mainly related to fast inward current amplitude due to the opening of voltage-gated Na^+ channels, which will be investigated further in chapter 3 of this dissertation. Since no significant differences between signal features were observed due to variabilities in flow rates below ten μL/min, we sought to explore the effect on signal output with higher flow rates; 10, 20, 30, and 40μL/min. It is also noteworthy that flow rates below ten μL/min are not recommended for SPR binding kinetics experiments due to the fact that mass transfer is directly correlated with flow rate[140–142].

In the case of higher flow rates of 10, 20, 30, and 40μL/min, we sought to explore the same feature variation in signal output as those with lower flow rates by testing 3 CM-cultured sensors. Distinct and significant differences between signal's amplitude, FWHM, and signal to noise ratio were observed (Figure 8*)*. The significant difference in signal features as the flow speed increases can be due to multiple reasons. The first cause can be attributed to the increased turbulence kinetic energy (TKE) of fluid portions trapped between the cell membrane and sensor surface (see Figure 2C). An increase in flow speed will substantially increase the kinetic energy in these medium pockets between the plasma membrane and the sensor, where the value of K'_1 in Eq. 15 is no longer negligible. The addition of K'_1 will shift the equilibrium values to the right side of Eq. 15. The excitable cell-SPR model changes as a result and the inclusion of fluid's kinetic energy will shift the energy distribution from potential to kinetic, in which charge differences are then unnoticeable and undetectable with refraction angle changes. In other words, stronger redistribution of charge as a result of cellular contraction in comparison with non-contractile excitable cells, brings a stronger factor (kinetic) into the excitable-cell SPR model than cellular field potentials. Figure 8A shows a significant difference between

amplitude, FWHM, and SNR features of the periodic signal at 10µL/min compared to 20, 30, and 40µL/min. In Figure 8B, a sample representative of contraction profiles with different flow rates is shown. The 10µL/min flow shows the highest signal-to-noise ratio in detecting charge variabilities near the cell membrane of excitable cells. Therefore, the flow rate was set at 10µL/min for all further experiments of this study as a likelihood of an optimized value for flow rate.

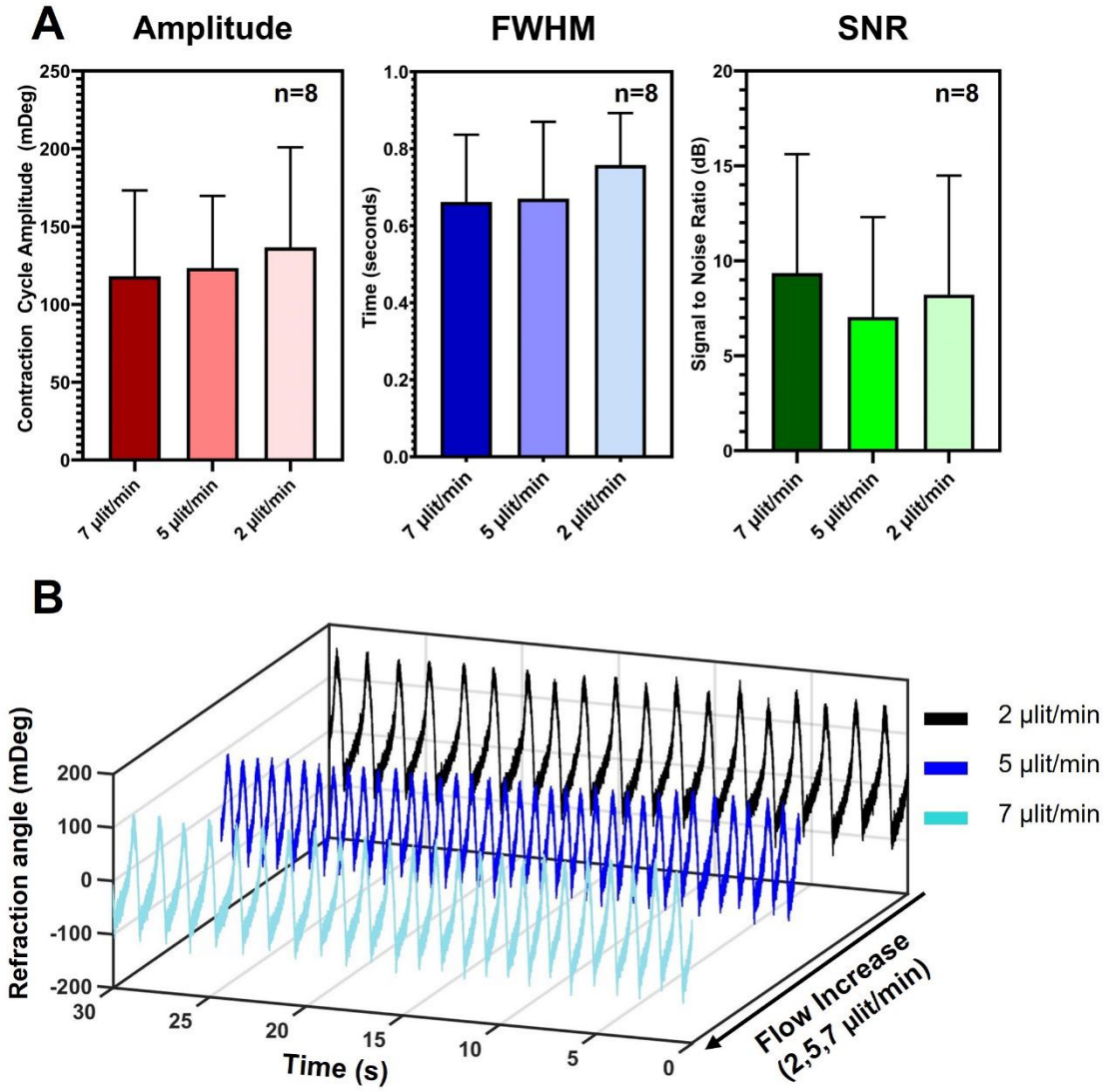

Figure 7. Effect of flow rates lower than 10 µL/min on contraction profile of cultured CM. A. Graphs of amplitude, FWHM, and signal-to-noise ratio changes across different flow rates are shown (n=8 sensors). No significant difference between signal features of 2, 5, and 7 µL/min flow rate was observed (using one-way ANOVA test, $p < 0.05$). High standard deviation values are due to sensor variability of signal output. B. A

waterfall graph of contraction profiles produced from 2, 5, and 7 µL/min flow rates are shown. A slight decrease in signal amplitude as the flow increases is observed, which is insignificant.

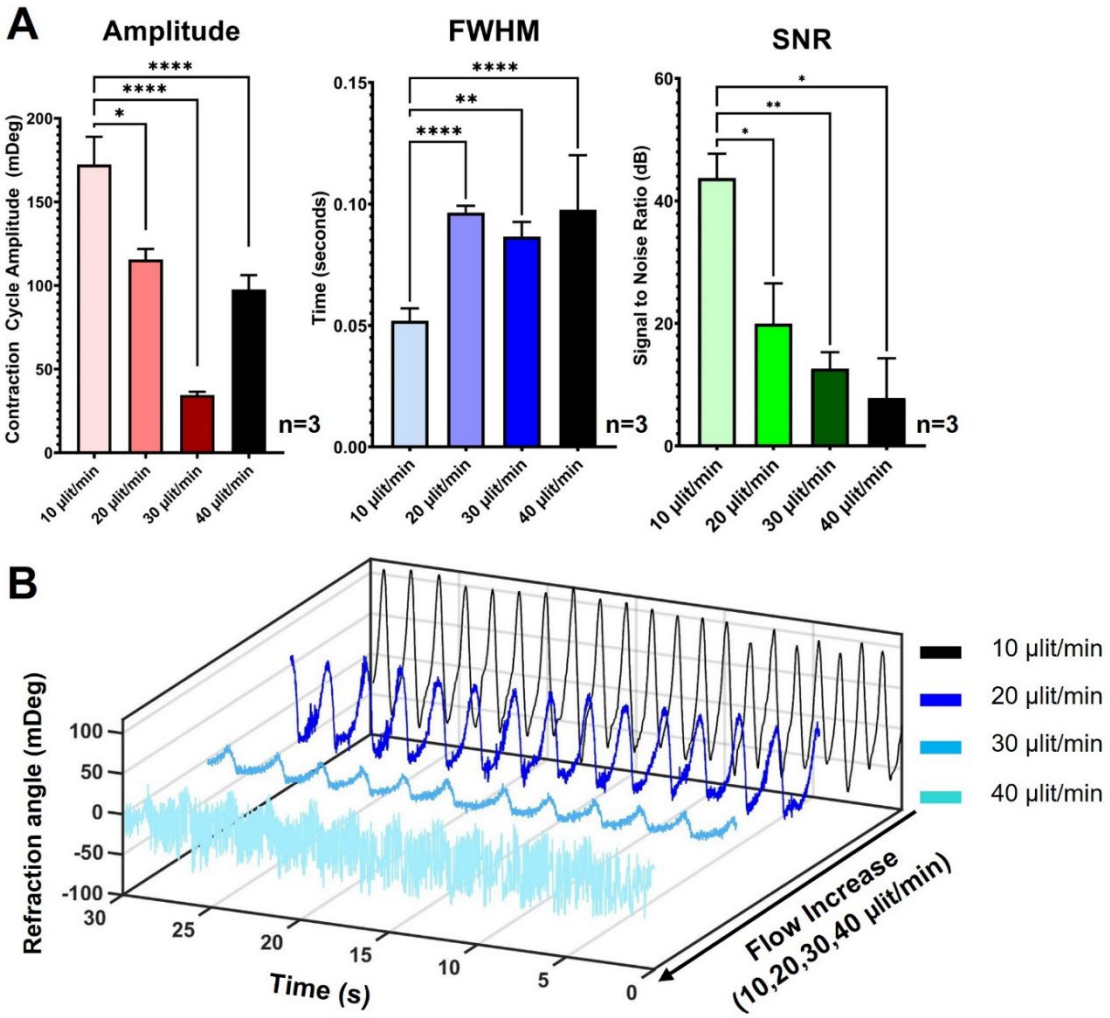

Figure 8. Effect of higher flow rates on contraction profile of cultured CM. A. Graphs of amplitude, FWHM (n=3 sensors using Kruskal-Wallis test, p <0.0001), and signal to noise ratio changes (n=3 sensors using Brown-Forsythe ANOVA test, p <0.0007) across different flow rates are shown. Values of amplitude, FWHM, and SNR of 10 µL/min flowrate (172.351±16.178, 0.052±0.005, 43.742±3.966 respectively) was significantly different from those of 20, 30, and 40 µL/min flow rate. B. A waterfall graph of contraction profiles produced from 10, 20, 30, and 40 µL/min flow rates is shown. A distinctly more potent signal with higher signal to noise ratio is observed for a flow rate of 10 µlit/min.

2.4.4 Cell-Substrate Strain Study Using Digital Correlation Analysis

We mentioned earlier that in our excitable cell-SPR model, part of the variations in signal amplitude across different sensors could be due to cellular motion factor contributing to refractive index variations of the medium. However, such input must be rhythmic and

synchronized across the sensor surface to extract the signal's contraction contribution force. Thus, the presence of spontaneously contracting well-networked CMs on the sensor is vital for developing a mechanical input in SPR sensograms from excitable cells. As a result of sensor reusability, our specific isolation/culture protocol, and experimenting in non-physiological conditions (e.g., 25ºC), exploring force of contraction from CM-cultured gold sensors was not practical using this setup. However, we have probed the strain of cell clusters' contraction on gold sensors, which were visually examined under a bright-field microscope for synchronized contraction across the sensor. A disk area of 6μm in diameter is selected as the region of interest for computing the strain effect in SPR's sensitive area (in theory, plasmon's sensitive wave propagation parallel to the surface is expected to be ~3.1 μm in length from each direction using a light source of 638nm wavelength on gold[62,108]). Using digital image correlation (DIC) analysis, the contraction strain is calculated from video recordings of beating CM clusters. The parameters we will be targeting are the strain of contraction and duration of relaxation/contraction periods. Although finding a direct correlation between SPR's sensograms and contraction profile is yet to be defined, it provides an understanding of the mechanical effect of cells on refractive index variations of the medium in confined spaces.

Contraction of a cardiac muscle cell happens in three known phases: latent period, contraction period, and relaxation period. The latent period is when the stimulus for contraction (i.e., CICR event in CMs) is initiated until the first indication of contraction. The contraction period is marked as the duration in which the force of contraction goes from 0 to maximum force (F_{max}); the relaxation period is the duration in which the force of contraction goes from F_{max} to resting state. The cycle is then followed by another latent

phase, completing a full contraction of a CM (Figure 9A). Recorded videos of contracting CMs cultured on gold sensors are analyzed using a DIC method in MATLAB for computing the displacement field of a region of interest in the video. The open-source software, Ncorr[143], has these features built-in and was thus used alongside in-house MATLAB code for video and image processing. First, strain is calculated based on the displacement acquired (ΔL) and the original cell position (L). Then, using the estimated stiffness of the electrode's modified surface (collagen/fibronectin treated gold) and the force-exerting area (A), the force can be computed according to the following equation:

$$F = E * A * \frac{\Delta L}{L} \quad \text{(Equation 21)}$$

E is Young's modulus for rat tail collagen fibers (60 MPa[142]), and A is SPR's sensitive disk region ($28.27*10^{-12}m^2$). Results are depicted in Figure 9. First, a section of video with high contrast between the cell and the background is selected (Figure 9B), where beating is continuous. Videos are taken with 30 frames per second rate. Then, the same section is analyzed over the video for similarity and correlation analysis using MATLAB. The analysis output was an x-y strain profile (ΔL/L) exerted by the cell in the selected region shown in stacked heat map graphs (Figure 9C).

The total force exerted on the sensitive area is calculated from the strain profile resulting in a force profile given in Figure 9D. Fmax for cells is calculated as 29.52±14.50μN. The contraction and relaxation periods are measured as 0.59±0.04s and 0.60±0.04s for the selected region of interest. We observed a decrease in the contraction force measurements and a prolonged contraction-relaxation period compared with results presented in the literature, most likely due to previously mentioned cell exposure to non-physiological conditions.

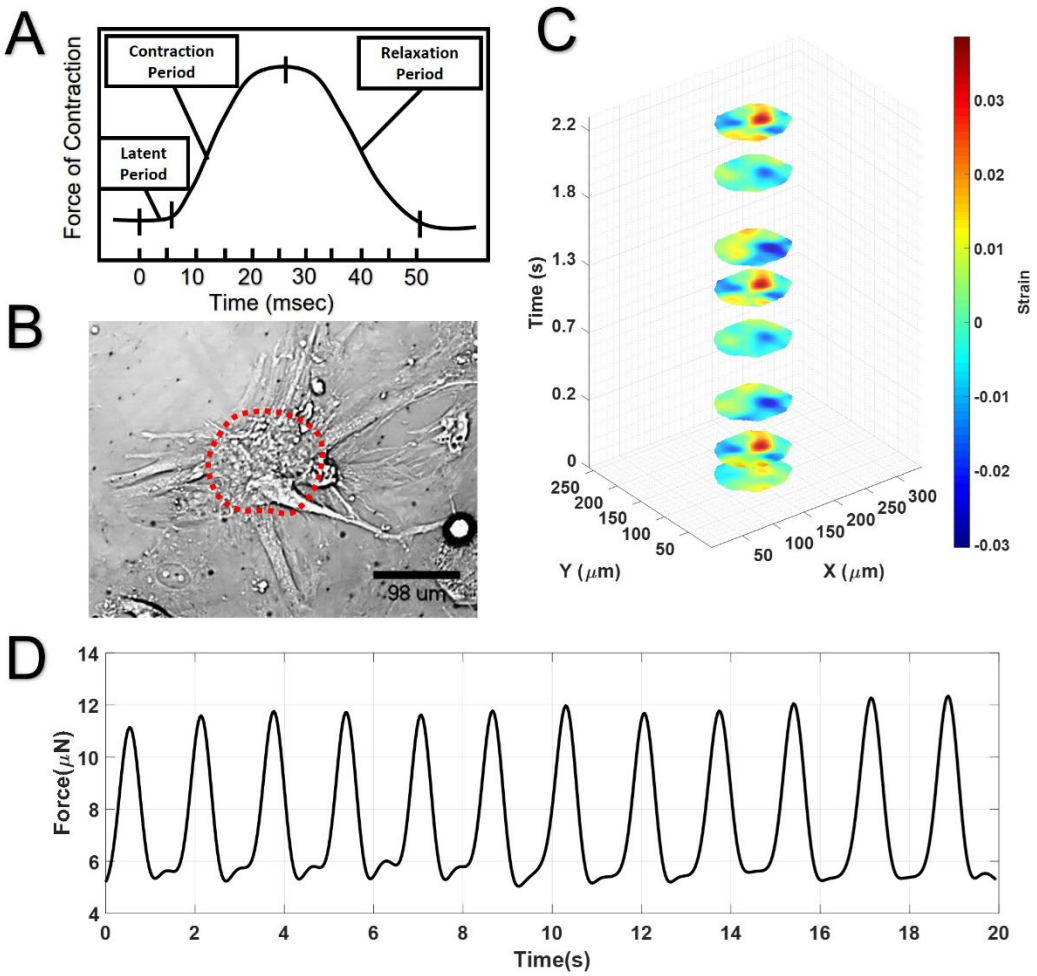

Figure 9. Digital Image Correlation Results from Ncorr. A. muscle contraction phases across time (latent, contraction, and relaxation) B. example snapshot of cardiomyocyte from a sample sensor to show region of interest (ROI, red dotted curve) used for digital image correlation. C. strain heat map at various significant time points that correlate to periods of lowest and maximum contraction. D. force profile taken by first averaging a smaller sub region of the ROI across time and then converting from strain to force.

2.5 Chapter Outcome

Information obtained from live cardiac cells using SPR has rarely been exploited for extracting outputs representing a cell's primary features, such as contractility and conductivity. In recent years, however, an increase in the interest in exploiting the potential of plasmonics for monitoring excitable cell behavior has been observed[109–113]. Nevertheless, there is still a gap in the literature for true live cell-plasmon interactions, which lead to variations in detected light's refraction angle using SPR. Such a gap can

inversely affect efficient data analysis and accurate clinical translation of plasmonics as a new modality for extracting a cardiogram. Thus, a more in-depth investigation of an excitable cell-SPR model is crucial. We have shown that viable CM-integrated gold SPR sensors are developed using our methodology, and cellular function is tested using this optophysical phenomenon. Furthermore, with our in-house algorithm for signal analysis and feature extraction, a single cardiac cell's action potential response in a network of CMs can be traced by its ion channel activities, using surface plasmon resonance.

The BI2000 SPR device allows acquiring a contraction profile from two different cardiac cells, each under one of the device's microchannels, 4 millimeters apart. The detection depth of the propagating SPs is <200nm in height perpendicular to the sensor's surface and ~3.1μm parallel to the sensor's surface in all directions. Thus, the detection volume of each channel of the BI2000 constitutes a cylinder of ~6μm in diameter and 200nm tall. The average size of neonatal rat CMs on day seven of culture (day of the experiment) varies substantially. From circular-shaped cells of 10-50μm in radius to rod-shaped ones of 100-500μm in length, we can estimate that the detection field of this SPR instrument not only reaches CMs' plasma membrane but also penetrates their cytosol[101].

Contracting CMs on SPR gold sensors change the refractive index of the dielectric medium they are beating in (as dropping a rock in a pond). This change in refractive index causes a shift in the refracted light's angle ($\Delta\theta$) detected by the BI2000 SPR instrument as a periodic time series, while the physical contributors to the signal are unknown. Several causes can be considered as underlying reasons for the cyclic plasmonic signal received from contracting CMs. Such causes include charge fluxes, spatial differences in cell membrane lipids, the presence of various proteins, filaments, and organelles in the cytosol

near the membrane, and the rhythmic mechanical motion of the cell. Immediately, a concern can be raised whether the cell membrane remains within the 200-nanometer SPR detection window during a contraction in the case of cardiac cells. This question was resolved by other groups using the SPR Imaging (SPRi) technique[61]. They showed that surface modifications (e.g., collagen) contributed to less than 10% of the sensitive plasmonic field of detection (<20 nm). They also concluded in their study that CMs' cell-substrate distance varies between 10nm and 80nm through contraction-relaxation periods, which again resides within the spatial sensitivity of SPR[61,62]. Our mathematical model uses an extrapolation of the measured CM membrane-substrate distance in Kreysing et al. study as the (r) value in equation 20[61].

Our results are consistent with the leading theory in the literature, suggesting the periodic SPR signal acquired from contracting CMs is partially due to continuous dynamic redistribution of charged ions across the cell membrane[61,62]. By overlapping empirical and theoretical results of the excitable cell-SPR model, a well-correlated outcome between events of a possible cardiac action potential (obtained empirically) and the effect of the bio-charge distribution of excitable cells on the resonance of SPs (obtained theoretically) was observed. The correlation between refractive index change to charge variations of contracting CMs suggested that the shift in light's refraction direction is due to the change in surface plasmon's energy as they interact with varying charge distributions near the CMs' plasma membrane. Speculation is also given to a mechanical cue in the signal.

Based on the data presented here, we propose that the surface plasmon resonance technique combined with a flow micro-fluidic-based module can be used as a non-intrusive and label-free methodology to comprehensively monitor excitable eukaryotic cells'

function, such as CMs. We propose to name the technique used here as a "Plasmonic Cardio-eukaryography," or abbreviated as P-CeG, and to be referred to in the future chapters as such. Further investigation into signal features and clinical importance, such as early afterdepolarization events (EADs), is continued in chapters three and four of this dissertation. Chapter four will most specifically focus on several physiological pathways of CMs using inhibitory and excitatory pathways to study the source of the signal further, improving our sensor's selectivity for P-CeG.

CHAPTER 3. HIDDEN SIGNAL INFORMATION OF PLASMONIC CARDIO-EUKARYOGRAPHY: A CASE STUDY OF THE P-CeG SIGNAL

3.1 Introduction

Physiological events, such as the contraction of the human heart, are complex. From the microscopic machinery of ionic channels to contraction and relaxation of the heart muscle, physiological events are nonlinear yet co-dependent. For example, the expression of a specific potassium/sodium hyperpolarization-activated cyclic nucleotide-gated channel (HCN4) is vital for the production of spontaneous contraction of induced pluripotent stem cell-derived cardiomyocytes (iPSC-CMs)[117]. This nonlinear codependency of physiological events with submicron scale components (e.g., ion channels, biomolecules) calls for a more comprehensive analysis of physiologically driven signals.

More specifically, when a newly developed physiological signal (e.g., Plasmonic Cardio-Eukaryography signal (P-CeG)) is presented, it is necessary to dedicate a comprehensive study to exploring its potential output parameters. Furthermore, tailoring the extraction of these parameters towards producing clinically valuable information must also be considered. For instance, due to advancements in cardiac tissue engineering, the application of fully differentiated iPSC-derived CMs in grafting of damaged ventricular myocardium has been recently successful in both pre-clinical[36,144] and clinical studies[145]. However, research shows that differentiated CMs express a full range of physiological cardiac phenotypes, including a spontaneous contraction in the absence of pacemaker cells[117]. In addition, scholars have shown that despite the improvement of the viability of the infarcted cardiac tissue post-implementation of iPSC-CM cellular grafts[145], there is

evidence of post-surgical cardiac arrhythmias. The source of these arrhythmias was found to be early afterdepolarization (EADs) events or pacemaker activity of the cellular grafts[144]. Therefore, comprehensive, non-intrusive, and label-free functional and structural characterization of CMs using the P-CeG signal prior to implementation might help with providing a comprehensive electrophysiological image of these grafts.

The famous electrocardiogram (ECG) is a highly reliable non-invasive method to provide an assessment of a patient's heart function. ECGs are the product of an inverse problem of electrocardiography[146,147] from four different electrodes placed on the human body. A patient's ECG records variations of the relative electric field at each electrode's location as the heart completes a contraction cycle. Despite the ECG being developed over a century ago, researchers continue to explore different linear and non-linear data analysis techniques to improve ECG data quality and extract more in-depth information of a patients' cardiac physiology using this technique[146–151]. ECG's advancements over many years only reinforces the complexity of cardio-specific physiological signals, especially those acquired using non-invasive means. Although our P-CeG signal is collected from a monolayer of cardiac cells and not the whole heart, signal complexity must not be underestimated.

On the other hand, recent progress in monitoring physiological feedback from excitable cells using plasmonic means has focused chiefly on sensor development and miniaturization[112,113], signal enhancement[109–111], and signal validation using visual bright field cell images[61,62]. Current studies are missing a comprehensive signal analysis of the plasmonic readouts from excitable cells. The complexity of light-matter interaction in the P-CeG signal should be considered carefully while investigating the signal. Hence, typical

analysis and signal processing methodologies of such newly developed signals, such as by root mean square for signal denoising, can result in significant data loss and errors in data analysis. Moreover, as surface plasmon resonance and its associated biosensors are relatively newly developed (the first SPR immunosensor was built in 1983[152]) and due to its complex working mechanism, most researchers using SPR have resorted to using its classical sensogram in their studies. The classical SPR sensogram depicts kinetic parameters of binding events between two small molecules[105] (e.g., protein-protein, antibody-antigen), which won't be the initial target of our data analysis, and will be later used in chapter 4 for drug studies.

This chapter explores the buried information of cardiac cells' action potential production and propagation using our plasmonic-based empirical and analytical studies. After elaborating on the signal acquisition, pre-processing, and processing modalities used, we explored the details of signal complexity using short-time Fourier transform (STFT). Concluding from complexity studies, we reduced the P-CeG signal noise before using the data to compute charge variations near the CM cell membrane. Results of charge variations were explored for their correspondence to a CM's field potential profile and field parameter extraction. The correlation of the analytical and empirical studies facilitates the grasp of the P-CeG signal production mechanism, strengthening our objective of using SPR as a tool for monitoring excitable cells' functionality. Hence, a commentary on the possibility of further extracting CMs' main properties (contractility, conductivity, excitability, and rhythmicity) from the P-CeG signal under ideal experimental conditions is presented. Finally, we extract the most common signal features of CMs' contraction from the SPR sensogram according to parameters previously reported in the literature (Table 3.1).

Table 3.1. Common Extracted Physiological Parameters of Cardiomyocytes

Signal's Extracted Features	Technique Used	Clinical Relevance	Ref.
Systolic and diastolic peak time, peak amplitude analysis, beat rate	Brightfield microscopy	Chronic toxicological studies on CMs, drug effect analysis on cardiac cells	120,188,189
Current density, action potential, action potential velocity	Patch clamp, fluorescent microscopy	Direct ion channel characterization for understanding cardiac channelopathies	190–192
Action potential plateau amplitude, resting membrane potential, APD20, APD50, APD90, voltage-gated ion channel activity	Whole cell patch clamp, dynamic patch clamp	Testing novel antiarrhythmic drugs	111,122,155,193
Field potential duration, action potential, APD30, APD80, upstroke velocity, decay velocity	Multielectrode arrays	Cardiomyocyte functional maturation, developmental, pathological, and pharmacological studies	153,164,194,195
Contraction velocity, relaxation velocity, beat rate, peak-peak interval	Microscopy video recording and motion tracking analysis	Relationship of contractile physiology of CMs and dynamic complexity of pharmaceutical studies	196,197
Beating frequency analysis of cardiac cell and tissue	Cardiac cell and tissue microscopy video recording	Beating rate variability of CMs in response to chemical (drugs) and physical (electrical fields) stimulations	198,199
Force of contraction, beat frequency, contractile frequency	Micro-machined cantilever sensor with embedded deflection-sensing element	Pharmacological and developmental studies of cardiac cells	200
Tension and cross-sectional tissue stress, contraction duration, spontaneous beating frequency	Microfabricated cantilever platform for cardiac tissue	Influence of chemical and biomechanical cues on the structure and function of engineered myocardial tissue	119

3.2 Methodology

3.2.1 P-CeG Data Acquisition

For detailed instruction and troubleshooting on the P-CeG signal acquisition, please refer to sections 2.3.1-2.3.4 of this dissertation. Briefly, SPR gold sensors and polydimethylsiloxane (PDMS) concentrator devices were cleaned and sterilized using 70% ethanol and UV exposure prior to cell seeding. After PDMS device-to-sensor integration, isolated cardiac cells from neonatal rat hearts were cultured on each sensor with a density of 250,000 cells.cm^{-2} in the center of the gold sensors. Cells are then maintained for seven days in a 37ºC and 5% CO_2 incubator, changing the medium solution every three days. On day seven of culture, sensors are visually examined for the presence of contractile CMs prior to SPR experiments, using a brightfield microscope. Immediately before each SPR experiment initiation, a cell-cultured sensor is removed from the culture plates. The sensor is gently air-dried on its non-gold surface using a nitrogen gun and is immediately transferred to the SPR setup. Our SPR instrument (BI2000, Biosensing Instruments, AZ) allows for the addition of a microfluidic module, where oxygen and nutrients are delivered to cells using two injector syringes. The signal is collected as a .txt file using the instrument's software, which shows light's refractive angle changes due to contracting CMs. A flow chart demonstration of the signal processing procedure is shown in Figure 10.

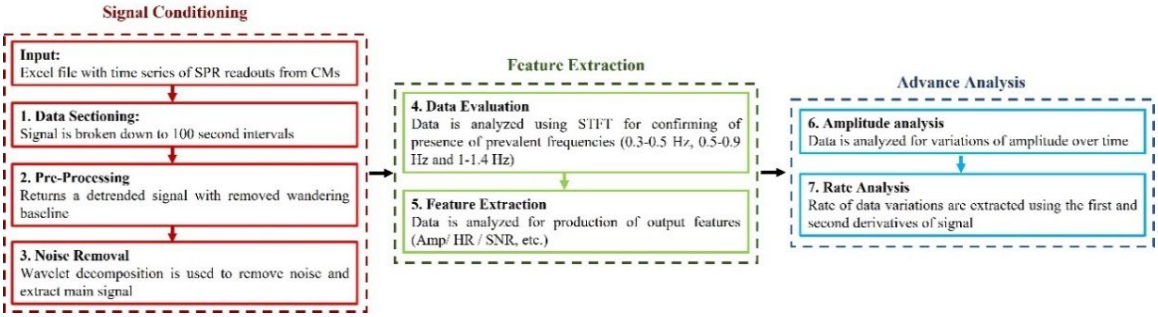

Figure 10. P-CeG signal processing flow chart. STFT: Short-Time Fourier Transform. AMP: Amplitude. HR: Heart Rate. SNR: Signal to Noise Ratio.

The entire duration of the signal is broken down to epochs of 100-second intervals. Each epoch is subjected to pre-processing and feature extraction (Signal Conditioning block in Figure 10). A sample signal of raw data collected from a new (Figure 11A) and used (Figure 11B) CM-cultured gold sensors is shown in Figure 11. Please note that the word "used" is employed for sensors that have been used previously for CM cell culture through the same protocol, at least once. We will follow the same sample presented in Figure 11 through signal pre-processing and processing methods in the following few sections. The comparison between CMs' contraction profile of cells cultured on new and used sensors is presented to investigate whether the employment of used sensors will result in significant data loss.

3.2.2 P-CeG Signal Artifact Removal and Pre-Processing

The text file containing SPR signals of CM contraction profiles are transferred to excel for further processing using MATLAB. As mentioned earlier, the main signal is broken down to 100-second interval signal epochs. Outlier rejection is performed using a cutoff threshold of 10 mDeg in signal's peaks amplitude for signal selection. The full cycle of the signals with average peak amplitudes of less than 10 mDeg in each 100-second interval are removed from the dataset. Such low amplitudes are likely due to sensor reuse, low cellular viability post cell isolation, culture contamination, or even combinations of these. The remaining signals are detrended by removing the best straight-line fit from the signal. A wandering baseline is observed in some experiments as a low-frequency artifact, which is removed through high-pass filtering using a 0.5-0.6 Hz passband frequency. The noise shown in Figure 11A and Figure 11B signals is then reduced using a built-in wavelet transform function in MATLAB, as recommended by previous studies of cardiac action

potential detection of noisy recordings[153]. The sampled signal after pre-processing is shown in Figure 11C and Figure 11D.

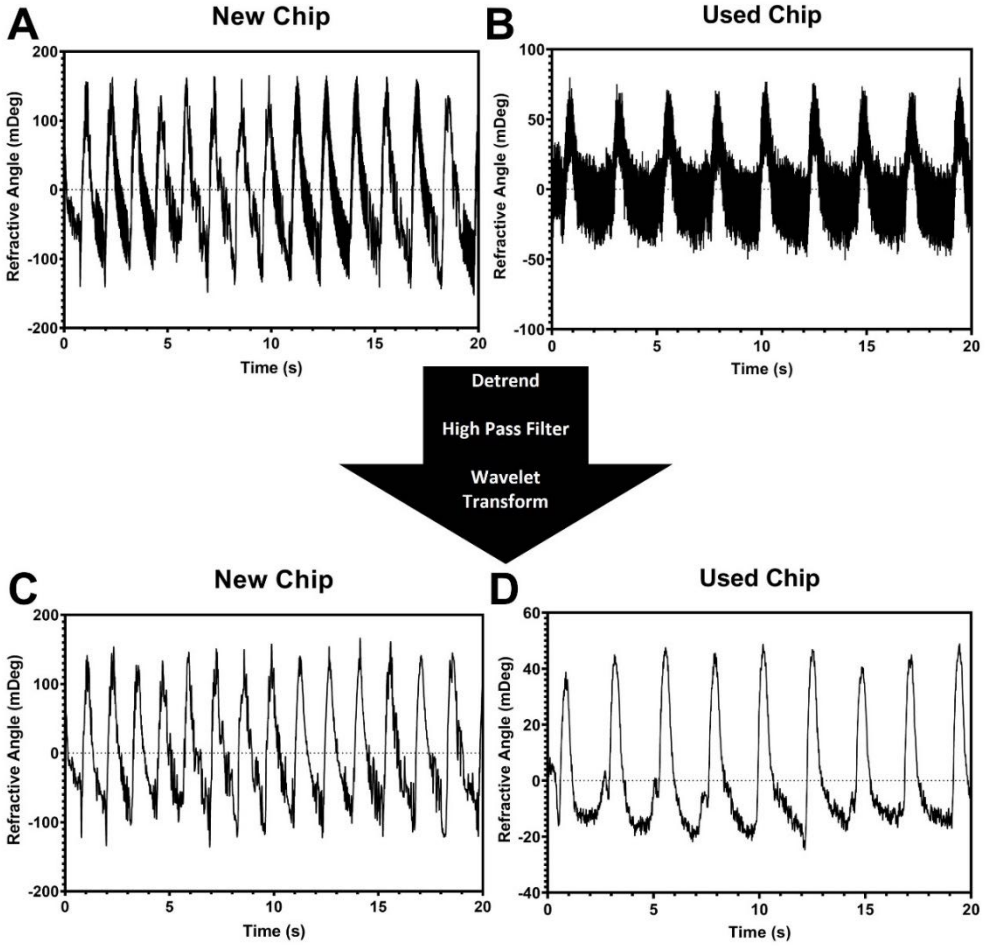

Figure 11. A and B. Raw signal acquired by measuring contracting CMs' activity using P-CeG for new (A) and used (B) gold sensors. C and D. Pre-processed signal using detrending, high pass filter of 0.5-0.6 Hz to remove the wandering baseline and signal denoising using wavelet transform.

3.2.3 P-CeG Signal Feature Extraction

The pre-processed signal is then analyzed for spike detection using a built-in MATLAB command (peakfind) and automatic thresholding. Spike detection results are plotted and visually inspected at the end of each 100-second interval's feature extraction. Intervals with missing selected spikes are manually adjusted to include accurate data through peak selection's threshold improvement. Next, each peak's location, amplitude

(Amp), and full width at half maximum (FWHM) values are consecutively recorded in separate arrays. The recorded arrays are then used for computing the mean and standard deviation of the signal's amplitude, FWHM, beat-beat interval, and beating rate across 100-second epochs. Figure 12A and Figure 12B show the output of spike selection and signal feature extraction. Computed features are then exported into GraphPad Prism version 9.2.0 for Windows for further statistical processing.

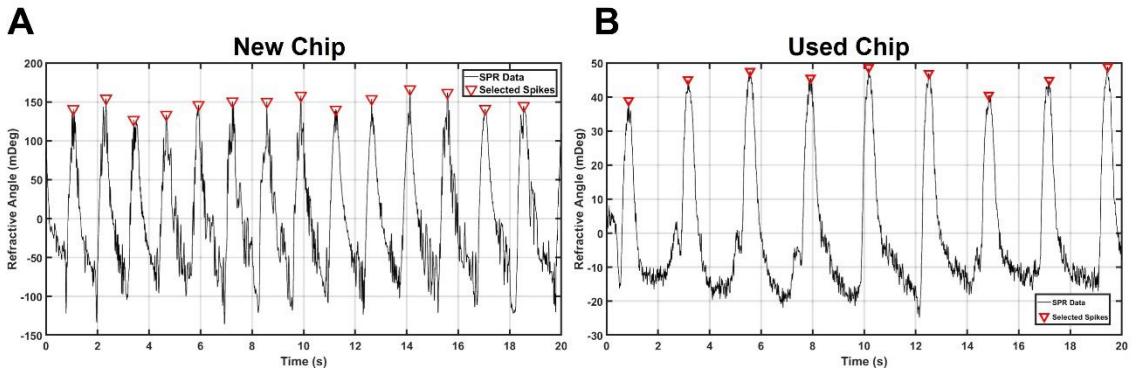

Figure 12. Visual examination of automated spike selection of signals from new (A) and used (B) gold sensors. The inverse red triangles mark the location of the selected peak's time and amplitude (mDeg) values.

3.2.4 P-CeG Signal Byproducts

For extracting signal byproducts such as field potential, all pre-processed signal values are inserted into our previous charge-angle correlation function (equation 20) for conversion of mDeg changes in the refractive angle of the light to coulombs of charge transfer near the cell membrane (Q):

$$Q = \check{\mathrm{C}}\frac{\frac{\hbar^2 n^2 \pi^2}{2mL^2} - \varepsilon(hf)^2}{\varepsilon hf} \qquad \text{(Equation 20)}$$

Where ħ is the reduced Planck's constant ($1.054*10^{-34}$ J.s), n is the number of the electron's shell, m is electron's mass ($9.109*10^{-31}$kg), L is the length of the enclosed space in which the charge distribution is calculated ($4*10^{-3}$m), ε is the dielectric of the medium which is

empirically extracted from the P-CeG signal, h is the Planck's constant ($6.626*10^{-34}$kg/s), f is the frequency of light with λ=630 nm, and Č is calculated as:

$$\check{C} = \frac{r}{3.52*10^{-20}k}$$

Where r is the distance between the electron density cloud and the cell membrane (~100nm)[61], k is the coulomb's constant ($8.988*10^{9}$N.m^2/C^2). Although r has been considered a constant value in our calculations (r=50nm), it is a function of the probability wave function amplitude of the electron density cloud ($|\Psi(x)|^2$) once the effect of kinetic energy is included in advancing the development of the P-CeG signal. Q values calculated in the charge-angle correlation function (equation 20) are used to depict the profile of charge variations near the CM's cell membrane during an event of contraction. Over time, changes in Q values are denoted as the first derivative of charge, which defines the current flow in an enclosed system. The first derivative of Q values identifies current events that propel the action potential of contracting cardiomyocytes (e.g., depolarization, repolarization, hyperpolarization). Q values and the current flow during a cardiac cell's contraction for the original signal's data (Figure 11A and 11B) are shown in Figure 13A-D. Furthermore, measures of variations in refractive angle change (the P-CeG dataset) over time are marked as the first derivative of the P-CeG signal. The first derivative of the P-CeG signal can be used to compute a few clinically essential features such as action potential durations (e.g., action potential duration at 90% repolarization (APD90)) and action potential upstroke and decay velocities.

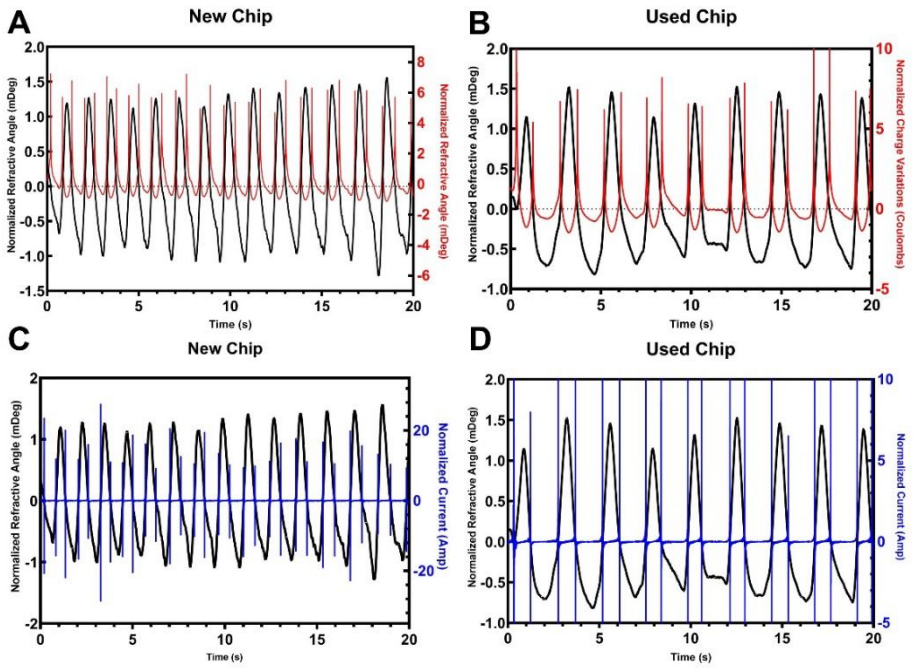

Figure 13. Parts A and B show the charge variations (red line) near the cell membrane of CMs cultured on new and used sensors, respectively. The black line demonstrates the P-CeG signal after pre-processing. Parts C and D of this figure show the derivative of charge variations, which correspond to the current flow within the enclosed space between the cell membrane and the sensor of new and used sensors.

3.3 Results and Discussion

The data presented in this study constitutes a sample size of twelve CM-cultured gold sensors (n=12). The P-CeG signal of each sensor is processed for signal complexity, signal correlation to the mathematical model, and CMs' physiological kinetic and dynamic feature extraction. The processing procedure is designed to minimize data loss and errors in analysis through an understanding of the plasmonic derived time-series of contracting CMs using gold sensors.

3.3.1 Signal Noise Reduction and Complexity Analysis

A time-series signal acquired from a complex biological system (e.g., the heart), must be accompanied by a detailed signal analysis study. Moreover, if the methodology to acquire the biological time-series signal is newly developed (e.g., P-CeG signal), the

signal's complexity must be carefully investigated. Here we have resorted to measures such the short-time Fourier transform (STFT) technique to understand signal complexity.

Signal's Spectrogram (STFT):

A spectrogram, otherwise called the STFT of a signal, is a visual method for analyzing time-varying frequencies in a signal. To see how the frequency content changes over time, we can cut the signal into blocks of the desired window size and compute each block's power spectrum (dB). The blocking process of the signal (i.e., windowing) uses the concept of wavelet transforms, a common technique for the extraction of valuable signals from noisy datasets[153]. Signal's STFT is a good representation of the most repeated frequencies in a time-series signal and serves as a measure of the signal's complexity. STFT has shown promise in identifying frequency variations in physiological signals (e.g., electroencephalography) of normal and diseased patients[154]. In the case of our P-CeG signal, STFT helps define the most prevalent frequencies in the signal. Our effort to understand the signal correlates these detected frequencies to their underlying electromechanical cause of CM contraction.

We have used a built-in MATLAB function (modwt) to utilize wavelet transforms of a window length of 1000 samples per second for each signal. It should be noted that the P-CeG signal samples used in this analysis section have been detrended and subjected to a highpass filter for removing the wandering baseline. No further pre-processing was carried out on the signal. A sample P-CeG signal with its corresponding spectrogram is shown in 14A and 14B, respectively. We can distinguish the three most potent and repeated signal frequencies over time through visual inspection (Figure 14B, turquoise, red, and yellow horizontal lines). To extract the values of these prevalent frequencies, each signal's fast

Fourier transform (FFT) was computed and plotted for peak detection. Each peak represents one predominant frequency of the signal. .

Figure 14C shows the three frequencies detected from the signal's spectrogram as three distinct peaks. Each peak in the graph is denoted as Freq1, Freq2, and Freq3, where their values are extracted for our sample signals (n=12 CM-cultured sensors). For all CM-cultured gold sensors in this analysis, two dominant low-frequency events and one dominant high-frequency event are detected (Figure 14D, Freq1=0.67±0.20Hz, Freq2=1.35±0.39Hz, Freq3=201.37±103.31Hz). In addition, a significantly high standard deviation was observed in frequency variations of the high-frequency event across different sensors (green box in Figure 14D), suggesting one possible source of the high-frequency event being signal noise. Thus, the signal's noise was reduced using a wavelet decomposition.

Using the MATLAB built-in wavelet transform function (modwt, considered a cautious denoising procedure), we decomposed the signal into its components as suggested in a recent study[153]. We used an orthogonal wavelet to preserve the energy at each analysis stage to ensure that data loss is strictly limited to signal noise. The word "energy" here refers to time-series energy, defined as the area under the squared magnitude of the target signal's amplitude at each point in time. The decomposed signal components through eight levels of an orthogonal wavelet transform in MATLAB are shown in Figure 15A. An expansion of timepoints between 50 and 60 seconds (red dashed block in Figure 15A) of decomposition levels 5 through 8, along with the signal's approximate reconstruction, is depicted in Figure 15B. Note that only components of levels 5 through 8 are included in the reconstructed signal since all previous levels of the signal's decomposed components

(levels 1-4) showed high-frequency events with a non-distinguishable periodic pattern. The denoised signal (solid red line in Figure 16A) is then overlayed with the original dataset (solid blue line in Figure 16A), where the reconstructed signal is composed of the summation of levels 5 through 8 of the signal's wavelet decomposition components. The same method is applied to all our samples (n=12 CM-cultured sensors).

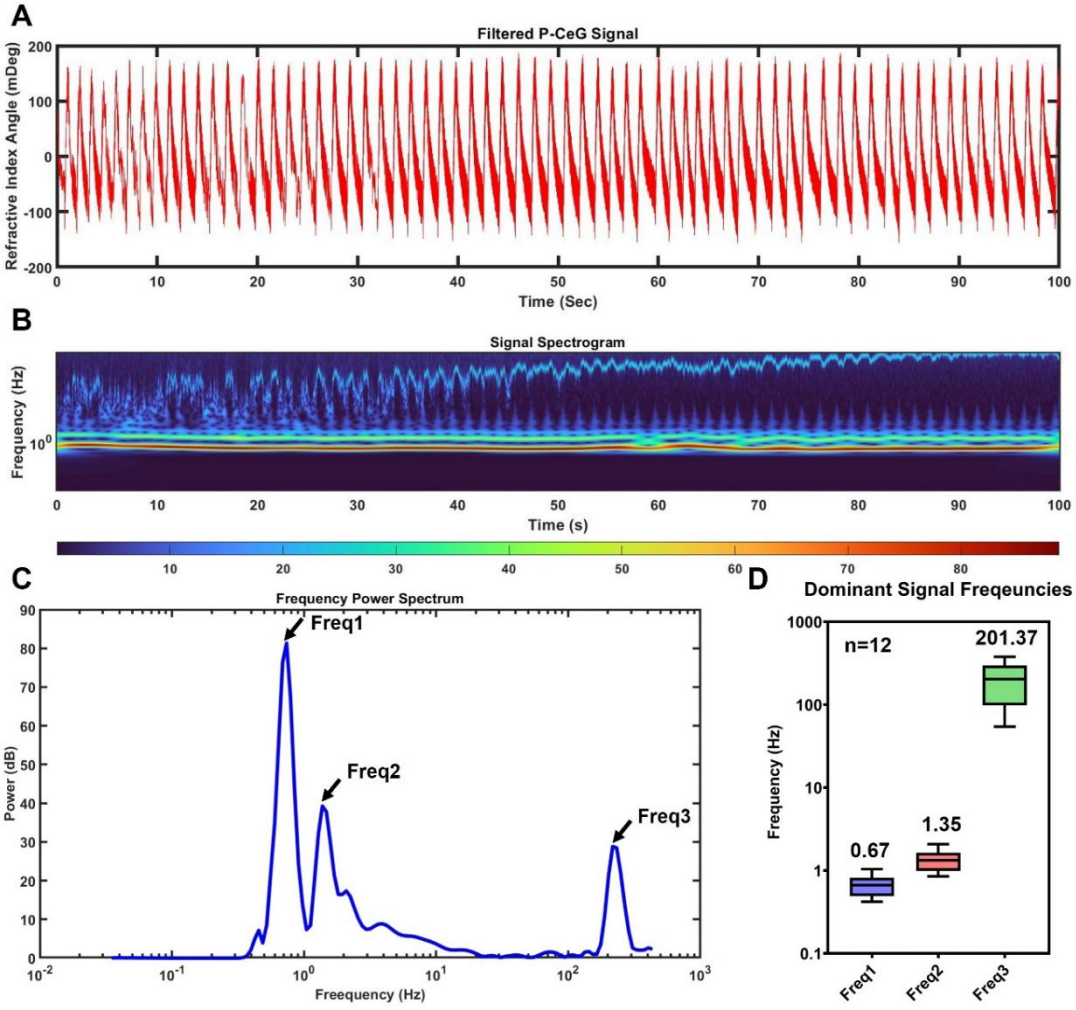

Figure 14. The P-CeG signal complexity analysis using short-time Fourier transform (STFT). A) the detrended P-CeG signal with its removed wandering baseline of a sample CM-cultured gold sensor is shown. B) spectrogram (STFT) of the signal shown in part A is depicted. The color bar shows the potency of each frequency in dB. C) The signal's most prevalent frequencies are detected using the Fourier transform of the signal. D) Freq1=0.67±0.20, Freq2=1.35±0.39, and Freq3=201.37±103.31 (mean ± standard deviation) of n=12 sample CM-cultured gold sensors are graphed. A high variation in Freq3's standard deviation and its high value of ~200Hz suggests the source of this frequency to be signal noise.

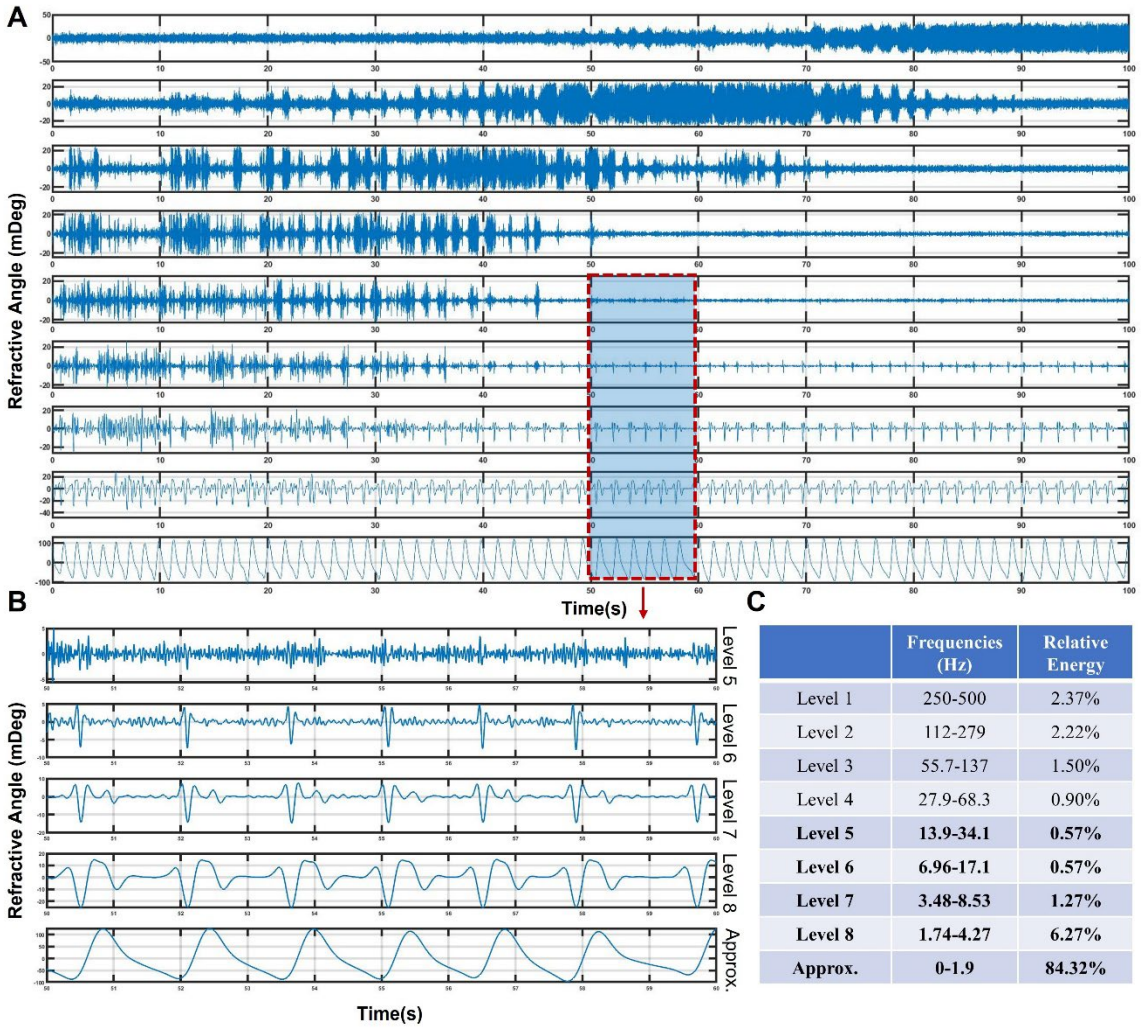

	Frequencies (Hz)	Relative Energy
Level 1	250-500	2.37%
Level 2	112-279	2.22%
Level 3	55.7-137	1.50%
Level 4	27.9-68.3	0.90%
Level 5	**13.9-34.1**	**0.57%**
Level 6	**6.96-17.1**	**0.57%**
Level 7	**3.48-8.53**	**1.27%**
Level 8	**1.74-4.27**	**6.27%**
Approx.	**0-1.9**	**84.32%**

Figure 15. Wavelet decomposition of a P-CeG sample signal. A) results of orthogonal wavelet decomposition of 8 levels (from top to bottom, 1 to 8 respectively) are shown. The first four levels show a noisy activity within the signal, which alters with no distinguishable pattern. B) An expansion of the blue block in part A is graphed, showing levels 5 through 8 of signal decomposition between 50 and 60-second timepoints. The approximate reconstruction of the denoised graph is depicted in the bottom graph as the summation of the four levels illustrated in graphs above it (levels 5-8). C) the table here presents a range of frequencies in each signal's decomposition level with their corresponding energy level. The relatively higher energy level of high-frequency events (levels 1 and 2) might be correlated with signal noise, which is later removed in this data analysis.

From level 5 to level 8 of the signal's decomposition, we observed similar periodic events of closely related shapes but varying amplitudes and durations occurring within the signal (Figure 15B, levels 5 through 8). The similarity between the peaks' frequency in levels 5 through 7, might suggest that one major frequency is chiefly associated with the electrophysiological activity of CMs (voltage gated ion channel activity). Differences in a

single period shape of signals of level 5 through 7 might be the effect of different ion channel activities (e.g., Na^+ channels, Ca^{2+} channels, K^+ channels); although channels opening and closing occurrence fall within a similar frequency (e.g., Freq1), yet each signal level's physiological cause might differ. For example, while opening and closing of voltage-gated Na^+ channels may be the underlying cause for the level 6 signal, major calcium transient events might be the lead for the decomposed signal of level 7. An increase in the amplitudes of these periodic events from decomposition levels 5 to 8 suggests that one possible correspondence of the level 8th event can be due to the cells' contraction. The extended duration of level 8th periodic events further suggests their close correlation to cellular contraction and relaxation episodes. The mechanism behind the detection of mechanical wave propagation using SPR has been rarely investigated previously[155,156]. In 2018, Kolomenskii et al. developed a multilayer model for an SPR-based optical transducer to convert mechanical waves of an acoustic source to optical ones[156]. They developed a theoretical model to show that an acoustic wave's interaction with surface plasmons (SPs) alters the dielectric properties of the medium where light refracts, resulting in a change in the light's refraction angle. The variation in the dielectric property is caused by the displacement of SPs in the close vicinity of the gold film as a result of acoustic waves induction on the sensor's surface[156]. However, a few critical initial conditions were considered in their study prior to initiating the acoustic inductions. Firstly, a several microns thick medium layer was studied in their model, where the thickness of the layer exceeded the penetration depth of SPs (<200 nm) to a large extent. The medium layer's relatively "semi-infinite" thickness accounts for a significant displacement in SPs near the metal film, altering the dielectric properties and changing the light's refractive angle. In

our CM-cultured gold film model, each cell serves as this semi-infinite thick layer (average CM's thickness is 10μm). Contraction and relaxation of cells result in the medium's displacement. As throwing a rock in a calm pond will distort the reflection of surrounding scenery, the contraction of CMs will also induce a rhythmic fluidic displacement, which results in alterations of the refracted light's direction. In nanometric scales near the sensor's surface, where SPs are propagating (between the inner Helmholtz plane and the outer Helmholtz plane of the electrical double layer), the medium movement might cause stress to be applied to ionic particles in between these planes. As a result of the scale change, this stress might cause a fast redistribution in not only charged particles but also other constituents of the medium (e.g., metabolites), leading to changes in refractive index. The fast displacement of matter as a consequence of cell contraction might account for our level 8^{th} decomposition having higher duration and a higher amplitude for each cycle. Moreover, Kolomenskii et al. suggested that the designed transducer model for converting mechanical waves to optical ones is only responsive under optical wavelengths of 633nm and 800nm[156]. Our SPR device's incident laser light wavelength is 630nm, which falls very close to the model developed by Kolomenskii's group. The correspondence of cellular

contraction to the P-CeG signal was further investigated using our drug studies and is presented in the next chapter.

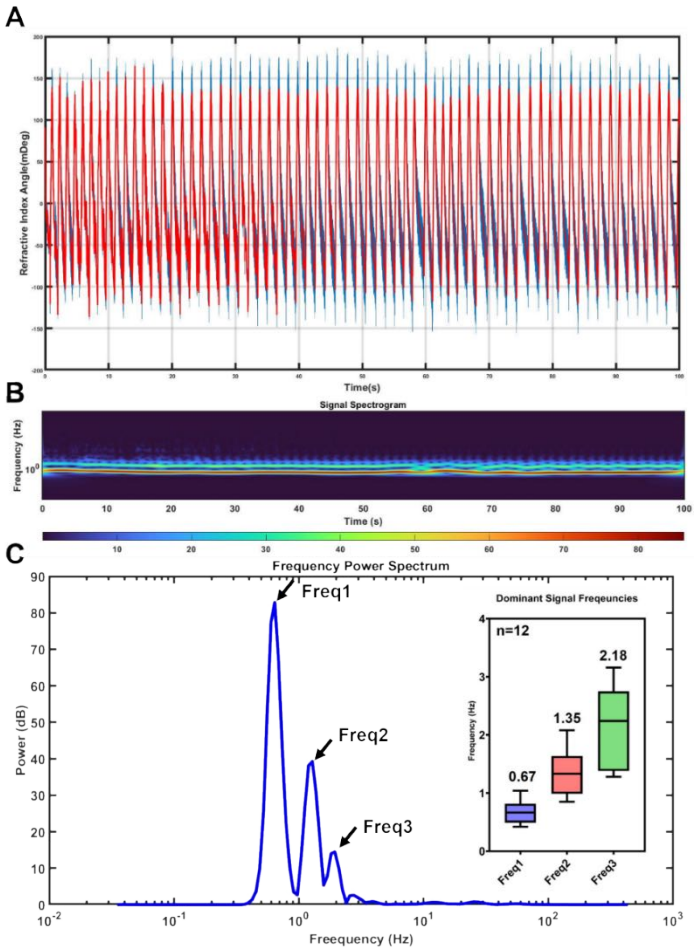

Figure 16. Denoised signal using wavelet transforms analyzed for complexity. A) Reconstructed signal after wavelet decomposition (solid red line) is overlayed on the original dataset (solid blue line). B) The STFT of the sample signal shown in part A is illustrated. The color bar shows a range of frequencies' potencies in dB. C) Updated predominant frequencies present in a sample P-CeG signal from contracting CMs are shown. The box plot depicts the mean and standard deviation of the three frequency values for our n=12 CM-cultured gold sensors (mean ± standard deviation, Freq1=0.67±0.20, Freq2=1.35±0.39, and Freq3=2.18±0.67).

After the signal's noise is reduced using wavelet transform, the reconstructed signals of all of the sensors are subjected to STFT analysis. A sample signal's three dominant frequencies, defined as Freq1, Freq2, and Freq3, are shown in Figure 16B and Figure 16C. Values of the first two dominant frequencies have not changed before and after signal reconstruction. On the other hand, the high-frequency noise event is removed and

replaced by a lower frequency event (Freq3=2.18±0.67 Hz, Figure 16C). Therefore, we identify a CM's contraction profile using SPR as a periodic signal with at least three predominant frequencies, Freq1=0.67±0.20 Hz, Freq2=1.35±0.39 Hz and Freq3=2.18±0.67 Hz. The results of the signal complexity study increase the level of certainty with which P-CeG datasets are analyzed.

3.3.2 P-CeG Field Potential Measurements

Careful yet comprehensive extraction of signal elements is essential to provide an accurate interpretation of a physiological signal. A cardiac cell's contraction constitutes both electrical and mechanical activities. Electrical activities include both their intracellular action potential and extracellular field potential propagations. The former is commonly measured using patch clamping techniques, while the latter can be measured using microelectrode arrays[157–161]. On the other hand, the mechanical activity is measured separately from these techniques, using fluorescence microscopy or microcantilevers[162,163]. In the case of the P-CeG signal, where the source of the signal collection is optical, three distinct frequencies are present within the signal. We hypothesize that one of these frequencies are related to CMs' contraction rate, while the other two frequencies are effects of different ionic channels' electrophysiological activity (Figure 16C*, e.g.,* opening of fast opening voltage-gated Na^+ channels, and the activity of Na^+/Ca^{2+} exchanger and Na^+/K^+ pumps). The relatively higher spread of datapoints of the third frequency (Freq3) might also suggest that this frequency could be as a result of the return wave of the fluidic motion in sub-micron pockets.

The waveform received using SPR from contracting CMs resembles a cardiomyocyte's action potential. However, it should be noted that a cell's action potential

is propagated within the cells' cytosol, while the field potential is an extracellular propagation of charge variations[164], although the two have been closely correlated[157,159]. The P-CeG signal is a real-time measure of refractive index changes of a medium within 200nm of the CM-cultured gold sensor's surface. Therefore, it encompasses both the cytosol and the extracellular electrical activity of the CMs (red highlighted block in Figure 1). Nevertheless, the contraction profile from the P-CeG signal is a summation of ionic redistributions inside SPR's sensitive field at each point in time, including intracellular and extracellular electrical activities. Moreover, referring to the inverse-square law in physics, the intensity of plasmonic wave propagation decays in all directions as the distance from the light's incident point increases. Hence, the P-CeG signal may be received mostly from the electromechanical events between the sensor's surface and CM's plasma membrane (Figure 2C).

We have previously shown that charge variations in the close vicinity of a contracting CM cell membrane may be computed using equation 20, based on SPR's principal mechanism and the law of preservation of energy. Figure 13A and Figure 13B show the overlay of charge variation data (red line, in coulombs) of a given P-CeG signal (black line, in mDeg) from contracting CMs. This correlation is a depiction of energy transformation between the electromechanical activity of CMs in close vicinity (<200nm) of a plasmonic gold sensor and the light's electromagnetic wave's direction of travel (i.e., refraction angle). To the best of our knowledge, no previous report correlating cardiomyocytes' electromechanical activity to SPR's refractive angle variations has been given in the literature.

Here, we have sought to explore the possibility of depicting our computed charge variations near the CM's plasma membrane as field potentials. Results are illustrated in Figure 17. First, the P-CeG signal from a sample sensor (black line in Figure 17B) is overlayed on its corresponding changes of charge over time (red line in Figure 17B and Figure 17C) computed using our previously derived equation (eq. 20). Next, an enlarged scale of the charge variations near the cell membrane is shown in Figure 17C, where it is then fitted manually with a curve, defined by us here as the P-CeG derived field potentials (blue line in Figure 17C). Our manual curve fitting is only presented to depict the overall plausible shape of the P-CeG derived field potential graph. In order to present quantifiable field potential values from the P-CeG signal, a mathematical fit is required. Previous analytical modeling of CM's field potential suggested a rational function with two separate cost functions as its numerator and denominator fit CMs field potential data[159], which should be investigated in future studies.

Two significant events are observed in each period of the P-CeG signal (red spikes in Figure 17B). The peaks at which charge variations occur overlap dominantly with phase one and phase two of the P-CeG signal (Figure 17A). Phase one in a CM action potential entails the depolarization event of CM contraction (Figure 17A). It shows the activity of fast opening Na^+ channels, allowing the inside of the cell to become more positive, initiating depolarization. In the P-CeG signal, phase one seems to correspond well with the depolarization event of CMs' contraction, also known as the depolarization amplitude (DA, Figure 17D bottom graph). The second event of the P-CeG derived field potential overlaps with the second and third phases of the P-CeG signal (Figure 17A and Figure 17D). The second phase in a CM contraction profile correlates to the opening of K^+ and Ca^{2+} channels,

and phase three correlates to the contraction initiation of CMs (Figure 17A). Opening of the potassium channels allows K+ ions to leave the cell, initiating cellular repolarization and getting the cell ready for the next contraction cycle. In phase two, the dynamics of fast and slow calcium channels launch a cascade of events, one of which is the calcium-induced calcium release (CICR) of the sarcoplasmic reticulum, resulting in CM's contraction episodes (phase three, Figure 17A). Phase three in CM action potential is called the repolarization phase and the amplitude of the peak in the field potential graph is denoted as the repolarization amplitude (RA, Figure 17D bottom graph).

It is noteworthy to mention that phase two and three of the P-CeG signal are most likely constructed from electrical and mechanical contributor elements to the signal, respectively. The electrical contributor to phase 2 of the P-CeG signal is the charge redistribution near the sensor surface because CM's K^+ and Ca^{2+} channels are opened. The mechanical contributor to the P-CeG signal's phase three is possibly the effect of the kinetic energy of fluid movements resulting from cell contraction on refractive index variations of the flow medium. Interestingly, we observed that the value of RA extracted from CM's P-CeG derived field potentials are higher than that of their DA across sample sensors (Figure 17E); although, it is expected for the DA to be larger than that of the RA in a given field potential graph of contracting CMs[159] (Figure 17D, bottom graph). The reason might be the three different frequencies within the P-CeG signal as extracted previously (Figure 16C). We hypothesized earlier that one of these frequencies is closely associated with CM's rate of contraction. A higher RA in the P-CeG derived field potential profiles suggests the possible overlap of two consecutive physical events (electrical and mechanical) read by SPR during phase 2 and phase 3 of the P-CeG signal. The

corresponding frequency to the mechanical event must be separated from the original P-CeG signal using a bandpass filter to distinguish between the two physical causes. However, to quantify which frequency corresponds to the cellular contraction, a complete mathematical model of the biophysical events of Cell-SPR must be presented, which will be one of the goals of our future studies.

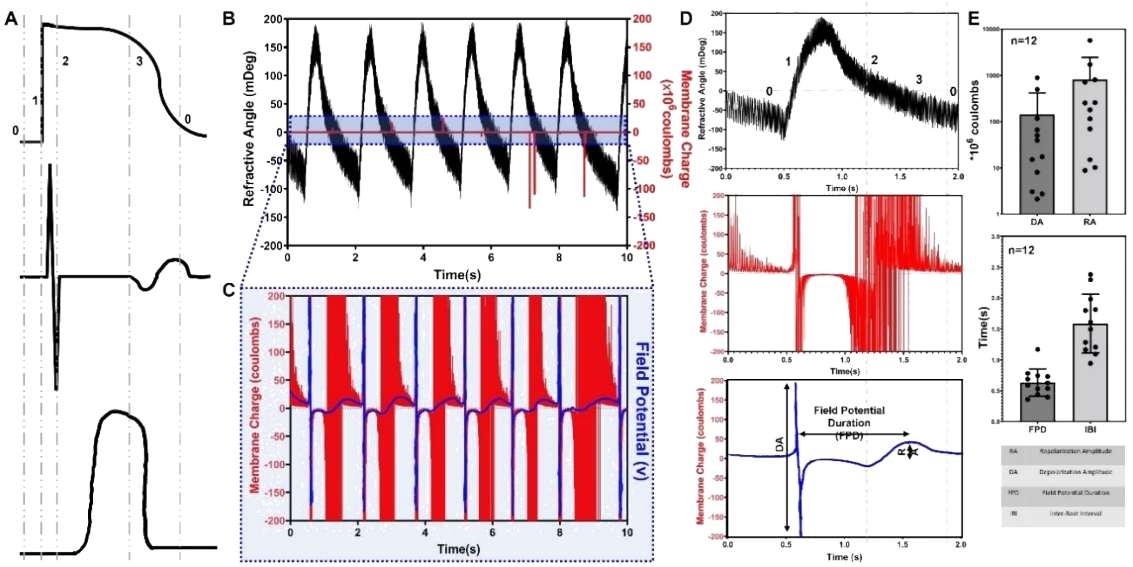

Figure 17. Correlation of empirical P-CeG data to the mathematical model of charge distribution near a CM's cell membrane. A) The illustration here depicts the four phases in a CM's action potential, field potential, and force of contraction profile (top to bottom, respectively) over time. The grey dashed lines show phases 0, 1, 2, and 3 of the CM's electromechanical activities. B) Raw data of the P-CeG signal in black are graphed on the left y-axis in mDeg changes of refractive angle of light. The corresponding charge variations near the CM cell membrane in red are graphed on the right y-axis in megacoulombs. Values are extracted using equation 20. C) An expansion of the blue block in section B is shown, where the charge variations in red are graphed on the left y-axis in coulombs, with a manual curve-fitting of the blue line, depicting a possible field potential near the cell membrane. D) From top to bottom: a single period of the P-CeG signal (black, mDeg), its corresponding charge variations (red, coulombs), and an illustration of the possible corresponding field potential (blue) are shown. Arrows from left to right in the bottom graph depict the depolarization amplitude (DA), field potential duration (FPD), and the repolarization amplitude (RA) as the main features of a CM's field potential. E)

Field potential variables (e.g., DA, RA, FPD) are crucial factors determining a drug's cardiotoxicity[157]. Recently, state-of-the-art cardiac cell studies and *in-vitro* drug testing platforms such as heart-on-chip devices used field potential parameters as their primary measure for characterizing CM electrical activity[157,159]. In addition, several researchers have carried out non-invasive detection of field potential alterations of

contracting CMs for observing CM electrophysiology by developing MEAs[109,111,113,163]. Since the signal received through MEAs is from field potential values of CMs, relating the signal obtained to CM's action potential is challenging. To attain the cells' action potential profile, some of these MEA data collection algorithms solve a biological inverse problem, where field potential values and ion channel conductivity are employed in obtaining the cells' action potential[159]. Moreover, none of the abovementioned MEA designs were able to extract CMs' contraction force, an essential parameter in cardiac cell characterization.

Here, we have shown that the P-CeG derived FP of contracting CMs might serve as an alternative to currently existing MEAs for monitoring the electrical activity of CMs. The variation in field potential variables (RA, DA, FPD and, IBI) across different sensors is likely due mainly to the non-physiological experimental conditions (Figure 17E). The suboptimal conditions were due to a limitation with the SPR instrument available. One advantage of using plasmonic reading of FPs is the plasmon's independent source of signal recording that those of an MEA or a patch clamp from CMs field potentials. In either of the latter techniques, cells' electrophysiological signal is invasively obtained (by applying electrical stimulus to the cells in the case of MEAs, and through a physical seal with cells' plasma membrane for patch clamp studies). The non-intrusive nature of SPR in gathering electrophysiological data provides it with a modular design that can be fitted for a holistic characterization of a cell or a monolayer of cells.

Given that the CMs' frequency of motion (contraction) embedded in the P-CeG signal is identified and extracted from the original signal, the rest can be used to compute charge variations, leading to more accurate P-CeG derived field potential data. On the other hand, the separated motion's frequency illustrates the motion waveform of contracting

CMs. The area under the curve of the motion waveform is denoted as the average deformation distance (ADD), a measure of CMs' force development on the substrate on which they are attached (force of contraction)[133]. This measure might be an accompanying factor to the electrical component, presenting a comprehensive simultaneous characterization of CMs for their electromechanical activities in real-time.

3.3.3 "Is This a Cardiac Cell" Analysis Using the P-CeG Signal

Progress in cell and tissue engineering over the past few decades has led to successful pre-clinical and clinical applications of stem cell-derived grafts in cases such as post-infarct myocardial regeneration[36,144,145]. As the *in-vivo* application of patient-specific cellular therapies increases, the need for faster cell characterization rises as well.

Comprehensive live-cell characterization is a complex procedure of connecting the dots between several techniques for monitoring cell morphology, internal organelle construction, functionality, and genetic expressions, amongst other cellular characteristics. In a future where cellular characterization will be needed at each hospital offering cell therapy to its patients, a comprehensive characterization platform will prove more effective than a combination of multiple conventional techniques. Moreover, with advancements in nanotechnology and molecular sciences, there has been a hopeful increase in novel drug development for non-invasive treatment options. A comprehensive cell characterization platform will provide higher throughput in drug testing experiments, which will propel pre-clinical and clinical trials for faster market availability of the target drug.

In the case of cardiac cells, where a complex combination of the electrical and mechanical cycle of events drives cellular functionality, measuring cellular properties using an all-in-one device is even more necessary in preserving data accuracy and limiting

error production. Furthermore, an all-in-one model in cardiac cell characterization should have the capability of identifying the main properties of healthy and viable cardiomyocytes, including contractility, rhythmicity, excitability, and conductivity. A few studies used cumbersome fabrication techniques to develop MEA-integrated microfluidic devices for recordings of both electrical and mechanical signals from CMs to extract all of the above-mentioned cellular properties[86,165]. Although such designs can assist in presenting a more comprehensive picture of CMs' behavior compared to microscopy or patch clamps, the low practicality in device reproduction forms a challenge in the universal application of their technique across different hospitals and laboratories.

We have shown so far that the plasmonic cardio-eukaryography signal received from contracting CMs is composed of three dominant frequencies. Two of these frequencies are likely to be from an electrical cause resulting from CMs action potential propagation and consequent ion channel activity, while the other frequency might contain information on cellular contraction rate. Separation of the mechanical and electrical cues from the signal requires a mathematical model including kinetic energy in the enclosed system of the excitable cell-SPR model. In our model (chapter 2 of this dissertation), it was stated that for ease of calculations we assumed the cell-SPR system is stationary, allowing the kinetic energy transfer to be zero. Realistically, in a contracting CM-SPR model, fluid displacement of small pockets between the cell and the sensor surface (Figure 2C), will most likely contribute to the changes in medium's refractive index. Action potential propagation produces an extracellular field potential, causing a redistribution in charge content near the sensor's surface. This spatial redistribution of charge might change the energy of the resonating plasmons, resulting in a shift in the angle of refracted light.

When a cardiac action potential reaches a cardiac cell, it depletes its sarcoplasmic reticulum of calcium through the process of calcium-induced calcium release, providing the actin and myosin heads with adequate Ca^{2+} for initiation of contraction. The subsequent contraction rapidly redistributes the medium-filled pockets between the cell membrane and the sensor surface, where surface plasmons propagate relatively potently. The force of contraction in the rapid displacement of these small fluid contents contributes to the kinetic energy loss or gain (depending on the direction of contraction force and action potential propagation, eq. 4 through 20). Therefore, the refracted light will contribute to its shift in angle from a mechanical source. Therefore, an updated model with kinetic energy vectors is essential to explore a CM's main properties using the P-CeG signal. First, however, a concise commentary is presented here for future researchers interested in this study.

The main properties of CMs include contractility, excitability, rhythmicity, and conductivity. A single CM's contractility is an all or none phenomenon, which means cellular contraction will not cease or get initiated until one cycle is completed. CM contraction relies on enough Ca^{2+} to initiate and maintain it. Therefore, the contractile event overlaps with phase 3 shown in the illustration of Figure 17A, where repolarization is also in progress. Contraction frequency, the force of contraction, and direction of force propagation can be extracted from a complete and updated cell-SPR model from the P-CeG signal.

Cellular excitability in CMs can be evaluated with genetic profiling and electrical stimulation studies of CMs[166–168]. In genetic profiling, one will be looking for the expression of sodium-potassium pumps such as HCN4, responsible for maintaining the hyperpolarization phase (phase 0 in Figure 17A*)* in contracting cardiomyocytes[117]. On the

other hand, in electrical stimulation studies, excitability is determined by measuring the differences between the threshold membrane potential and the resting membrane potential of the stimulated CM, depending on the duration of stimulation[168].

The third property of a CM is its conductivity, which suggests signal transduction capability from one cell to another. Expression of gap junctions, desmosomes, and tight junctions in isolated CMs from neonatal rat hearts will result in a tight network formation of homogenously contracting CMs[169]. This network formation is essential in carrying out action potential conduction studies. We have previously investigated the effect of possible gold substrate modifications, where collagen provided the most ergonomic bedding for forming the CM network on gold[56]. For cellular conductivity, the action potential propagation velocity of the P-CeG signal from a contracting cardiac syncytium on a gold sensor must be measured. These measurements in real-time provide a powerful tool in tracking the activity of membrane proteins responsible for cell connection formation, an essential indicator of CM maturity[36].

Last but not least, the rhythmicity of the CM beating profile, which serves as a factor of cellular homeostasis, can also be extracted from the P-CeG signal. In a healthy human body, cardiac rhythmicity is the relatively balanced rhythm between the heart's systolic and diastolic events. However, in a cell study, several internal metabolic cascades that maintain a cell's functional behavior must be investigated before providing an accurate physiological interpretation of cellular rhythmicity[116,170]. Nevertheless, in its simplest term, we can refer to rhythmicity as the beat rate variability in the cell-SPR model[171]. Extracting beat interval variability from the P-CeG signal allows the target CM's rhythmicity analysis.

As mentioned earlier, this section only serves as a commentary for future studies, suggesting the possibility of cell characterization using plasmonic means. SPR has a versatile configuration in cellular characterization, which is supported in this thesis using experimental and analytical models.

3.3.4 The P-CeG Signal Feature Extraction

An essential aspect of a newly developed signal is its feature definition and extraction. For example, a cyclic biological signal's period amplitude and duration are commonly used to characterize the time series spatiotemporal features. Furthermore, for contracting CMs', the Inter-Beat-Interval (IBI) is an important variable in disease model studies, where its variability is analyzed for detecting arrythmia[151,172,173].

The P-CeG signal of twelve samples of CM-cultured gold sensors is subjected to feature extraction for amplitude and full width at half maximum (FWHM) of each period, within 100-second epochs. In addition, depolarization amplitude, repolarization amplitude, and field potential duration for the signal are extracted from the charge variation graphs of contracting CMs. Variations in the amplitude, FWHM, and IBI of the P-CeG signal across these twelve sensors (Figure 18A) are likely attributed to the sensor's reusability and cell isolation methodology. On the other hand, the variation in the abovementioned features extracted for a single sensor is due to non-ideal experimental conditions for live-cell studies using SPR. It is expected that carrying out live cell-SPR experiments at ideal physiological environment, besides using new sensors for each experiment, greater consistency of the extracted P-CeG signal features within a single sensor and across different sensors, might be achieved

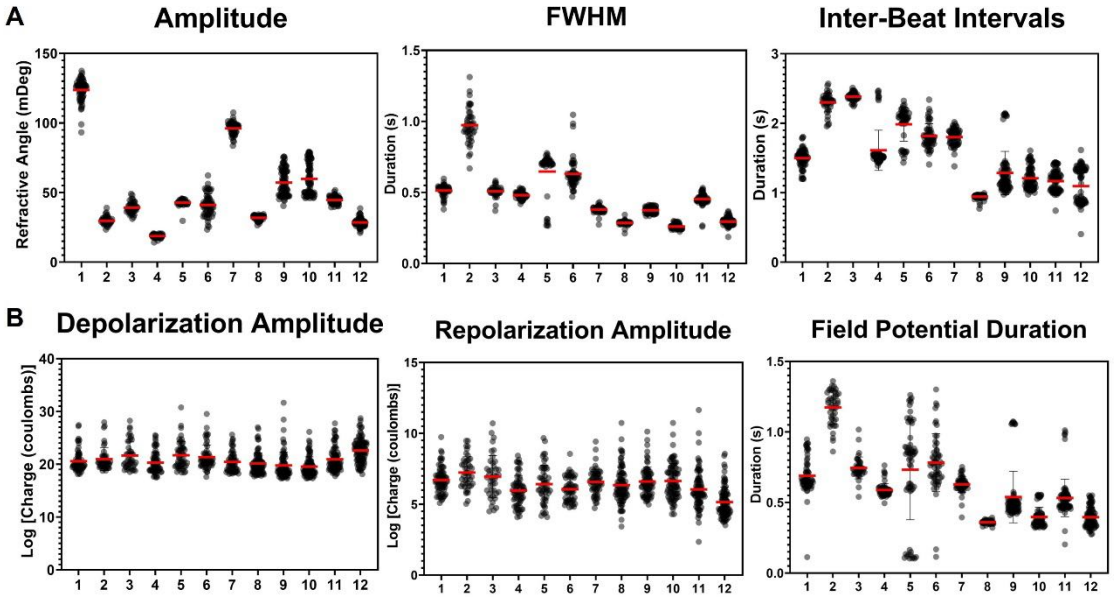

Figure 18. Feature extraction from the P-CeG signal and its correlated charge profile of contracting CMs. A) amplitude, full width at half maximum, and inter-beat intervals for a 100-second epoch from the P-CeG signal obtained from 12 CM-cultured gold sensors. The high variability of values across different sensors is due to our selected methodology for cell isolation and non-ideal experimental conditions (room temperature and without CO2). B) depolarization amplitude (DA), repolarization amplitude (RA), and field potential duration (FPD) of contracting CMs was obtained from their charge profile.

Moreover, we observed that each sensor's DA and RA features of contracting CMs' charge have less variability and more consistent distribution across different sensors (Figure 18B, left and middle graphs). One reason for such observation might likely be due to the omission of the kinetic energy and lack of cellular mechanical input from the excitable cell-SPR model developed. The cellular contraction will not affect charge data variability since RA and DA values are solely extracted from charge variations of contracting CMs' plasmonic signal. However, the FPD of the signal varies significantly between different sensors as a result of the previously mentioned unfavorable experimental conditions for live-cell studies. Feature extraction sensitivity to external stimulations (e.g., drugs) for the P-CeG signal are investigated and elaborated in chapter four of this dissertation.

3.4 Chapter Outcome

Introducing a new method for extracting electrophysiological information from live CMs requires an elaborate investigation into the signal's main characteristics. The P-CeG signal from contracting CMs is a novel plasmonic methodology developed in this dissertation for monitoring live cardiac cell activity. The label-free and non-instrusive approach of plasmonic methodology is a beneficial feature of the SPR technique for studying live cells, reducing experimental time and cost. This chapter explores the P-CeG signal for signal complexity, signal byproducts, and signal feature extraction.

The signal's short time Fourier transform revealed the presence of three dominant frequencies in the P-CeG time series. One of these dominant frequencies might be attributed to the voltage-gated ion channel activity of live CMs, which are responsible for the depolarization, plateau, and repolarization phases of cardiac action potential. Another frequency of the P-CeG signal might be associated with cellular contraction rate. The third frequency was from an unidentified source and is speculated to arise from the medium's return wave after cellular contraction, or the activity of exchanger pumps in CMs plasma membrane, along other possible explanations (e.g., cell membrane deformation). We will explore the underlying cause of these dominant frequencies in chapter four using drug stimulation studies.

The P-CeG signal's byproduct includes the variation in charge distribution near the CMs' plasma membrane, computed from our mathematical model of excitable cell-SPR. We have temporarily denoted this charge variation graph as CMs' discrete field potential profile and have extracted relevant features from the graph (DA, RA, and FPD). Acquiring a field potential profile from live CMs is advantageous in its ability to provide information

on cardiac cell subtypes[157], CM development[157], CMs' inotropy[173], cardiotoxicity and safety[157,173]. Another byproduct of the signal is the derivative of the P-CeG signal, where kinetic features such as upstroke velocity and inward/outward current flow from CMs might be extracted.

The P-CeG signal has shown some promise in simultaneously monitoring the electrical and mechanical function of contracting CMs. Exploring CMs' signaling pathways with drug promoters and inhibitors will shed more light on the P-CeG signal's characteristics, presented in chapter four.

CHAPTER 4. CHARACTERIZATION OF CHANGES IN THE P-CEG SIGNAL WITH EXTERNAL CHEMICAL PERTURBATIONS

4.1 Introduction

In previous chapters, we successfully extracted profiles from live contracting CMs using SPR (i.e., Plasmonic-Eukaryography (P-CeG))[56]. Since the source of the signal production (mechanical or electrical activity of CMs) was not known, a mathematical model of the excitable cell-SPR was developed in chapter two of this dissertation to correlate the SPR response unit to the electrical activities of contracting CMs. Despite the simplicity of the model developed, our results of measuring changes of extracellular charge over time using experimental data and the charge-angle correlation function (equation 20) presents a good correlation to an expected CMs' field potential profile. Our mathematical equation supports the effect of ion transport and extracellular field potentials from contracting CMs on the P-CeG signal. Thereupon, we cautiously investigated the charge-angle correlation of the cell-SPR model through a comprehensive data analysis study in chapter three. Results from signal decomposition suggested the presence of three dominant frequencies in the P-CeG signal. Our speculation as to the cause of these frequencies will be investigated more in this present chapter using external chemical perturbations. Blebbistatin, verapamil, and caffeine are used in this study for manipulating CM's signaling cascades. The P-CeG signal features before and after drug induction are compared.

from different ionic concentrations inside and outside the cell. The difference in K^+ ions inside and outside the cell dominates the resting membrane potential. After that, voltage-gated sodium channel (e.g., $Na_v1.5$) activation in cardiac cells are responsible for the action potential upstroke, initiating the depolarization stage of cardiac action potential[174]. Sodium channels are the key driver of action potential conduction.

The basics of the myocyte contraction are an influx of Ca^{2+} from outside the cell through calcium ion channels, allowing a pathway for more calcium release from inside the cell. The primary membrane proteins involved in moving Ca^{2+} into CMs are the L-type Ca^{2+} channels and the Na^+/Ca^{2+} exchanger pumps (NCX). A fundamental intracellular structure involved in the cycling of Ca^{2+} is the sarcoplasmic reticulum (SR), responsible for Ca^{2+} storage, Ca^{2+} uptake, and Ca^{2+} release. Ca^{2+} entering the cell is taken up by the SR via a Ca^{2+} pump called SERCA (sarco-endoplasmic reticular Ca^{2+} ATPase). To provide sufficient Ca^{2+} for the actin-myosin complex to initiate the contraction, SR discharges its storage of Ca^{2+} in response to activation of ryanodine receptor proteins (RyRs) expressed on SR's lumen. T-tubule microstructures assure the rapid distribution of Ca^{2+} ions throughout the cell. The binding of internally released Ca^{2+} to the troponin complex on the actin filament (one-half of the contractile protein unit in a CM) initiates the actin-myosin motility. The binding of adenosine triphosphate (ATP) molecules to the other half of the contractile protein, myosin, relaxes the muscle and ends the contraction period.

A common substance for blocking CM's contraction is blebbistatin, which has been used for optical recording of Ca^{2+} transients[118,175–177]. Blebbistatin is a myosin inhibitor and thus obstructs cellular contraction. Blebbistatin interferes neither with the binding of myosin to actin nor with ATP-induced actomyosin dissociation. Instead, it blocks the

myosin heads from complexing with low actin affinity[178]. The addition of blebbistatin in the culture medium of contracting CMs allows for the continuous conduction of their action potential while temporarily halting their contraction. Here, to study the P-CeG signal without the mechanical cue from contracting CMs, five different blebbistatin concentrations (1, 3, 5, 7, and 9 μM, based on previous studies[36,54]) were applied to CM-cultured chips. Analysis of the P-CeG signal features before and after blebbistatin addition confirms whether the P-CeG signal contains any effects from the CMs' mechanical activity.

Verapamil, an L-type calcium channel blocker, was used in this study to stop the inward flow of extracellular Ca^{2+} ions. Here, we used concentrations of 50, 100, 200, and 500nM of verapamil to block the inward current of Ca^{2+} ions and observed the variations of signal features prior to and post chemical addition. Finally, caffeine was used in our study to exacerbate CMs' force of contraction. Caffeine is known to produce a transient increase of resting Ca^{2+} concentration attributed to the release of Ca^{2+} ions from the SR[179]. This resting concentration of calcium ions is the amount present inside the cytosol due to SR calcium release. Calcium release is a positive feedback mechanism in CMs that will result in more calcium release; an event called calcium-induced calcium release (CICR)[179]. Studies have shown that caffeine concentrations above one millimolar causes a transient 5-12% increase in contraction amplitude of CMs[180,181]. The increase in contraction amplitude happens through depletion of the SR of Ca^{2+} in response to caffeine binding with the RyRs proteins, causing an increase in the isometric contractile force. We used caffeine concentrations of 2, 4, 6, and 8mM in testing the P-CeG signal's sensitivity to changes in

the force of contraction. Figure 19 illustrates CM's internal molecular pathways relevant to this study.

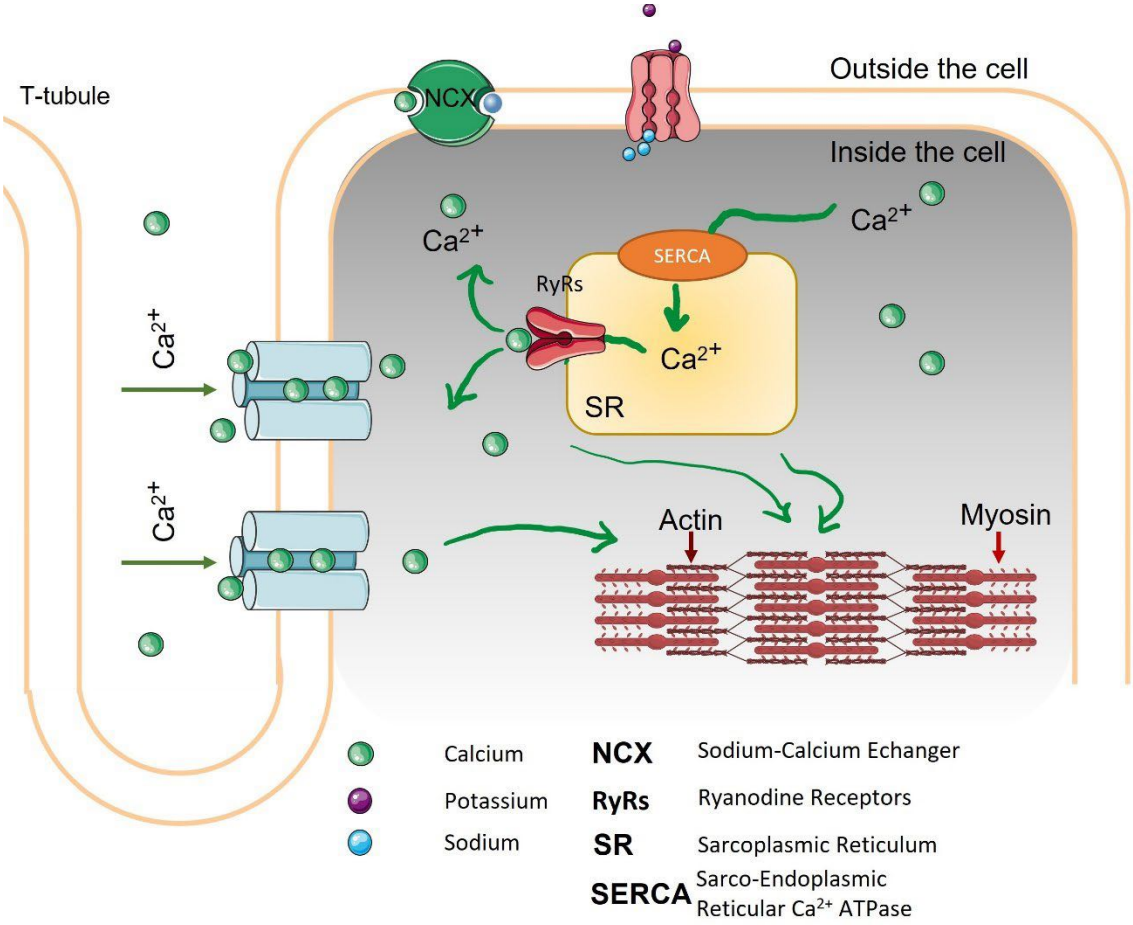

Figure 19. Calcium signaling pathways of cardiomyocytes.

4.2.2 Sensor Preparation and Cardiomyocyte Culture

Detailed procedures of SPR sensor preparation and CM isolation from neonatal rat hearts have been presented in chapter two of this dissertation. Cultured CMs are maintained for seven days before their plasmonic functionality analysis. On day seven of culture, gold sensors housing cardiomyocytes at confluency are mounted on the SPR prism (Biosensing Instruments, BI2000) after all desired injectable chemical concentrations are prepared.

4.2.3 Experimental Procedure

Plasmonic experiments of contracting CMs are done at room temperature under non-ideal cell culture conditions. According to their provided datasheets, drug concentrations for blebbistatin, verapamil, and caffeine (Sigma Aldrich, MO) is freshly prepared on the same day as the experiment. Prior to insertion of the cell-cultured sensors on the BI2000 prism, injection syringes are loaded with room temperature DMEM and are connected to the SPR system. After chip insertion the microfluidic gasket, which directs media and drug through two channels to the cells, is fixed on top of the sensor's surface. DMEM is immediately perfused at 10μL/min over both channels, providing the cells with nutrients throughout the study.

The signal's baseline is allowed to stabilize for 10 minutes. Once the baseline is stabilized and a contraction signal above 10mDeg change in refractive index (RI) has been established (through visual examination), drug injections are initiated. Each drug concentration injection is repeated three times to ensure statistical relevance of the results. Temporal studies of injecting consecutive drug concentrations were conducted separately on freshly developed cell-cultured sensors. Three samples of cell-cultured sensors were used for each drug. After signal stabilization, 120μL of sample drug, according to the manufacturer's manual, is injected through the injection port of the SPR device. To allow for an efficient binding event of the drug molecule with CMs, the flow rate is temporarily increased to 50μL/min, which is lower than the previously used 200-300μL/min flow rate by other groups performing plasmonic live cell studies[182]. After the baseline is established the flow rate is returned to 10μL/min again until the next injection. The reason for this flow rate alteration is the nature of our experimental design, combining recommended

experimental conditions for SPR binding kinetics (Biosensing Instruments, AZ, 50µlit/min) and those of live Cell-SPR studies (10µlit/min) established in chapter two of this dissertation. Data are recorded as Excel documents, later used for analysis and feature extraction. Each signal is separated into its drug injection epochs, and signal features before and after the injection are evaluated.

Features of amplitude (AMP) and full width at half maximum (FWHM) for each drug concentration before and after injection is extracted from the P-CeG signal (changes in RI with time). Charge variations near the cell membrane for each signal before and after drug injection are computed using equation 20. Depolarization amplitude (DA), repolarization amplitude (RA), and field potential duration (FPD) for each signal is acquired from the charge variation data and compared for each concentration. Statistical analysis was carried out using the non-parametric method of Kruskal-Wallis (i.e., one-way ANOVA) with a confidence interval of 95% (* $P < 0.05$ versus control).

4.3 Results and Discussion

4.3.1 The P-CeG Signal Characterizes Cardiomyocytes Electromechanical Function

Blebbistatin Outcomes:

Concentrations consisting of 1, 3, 5, 7, and 9µM blebbistatin were prepared in Hank's Balanced Salt Solution (HBSS, Thermo Fischer Scientific, MA) and used to block CM's contraction. P-CeG signal amplitude and FWHM of CMs treated with different drug concentrations were extracted and compared with controls. Data shows a drop in signal amplitude with the injection of the lowest blebbistatin concentration (1µM), suggesting the presence of a mechanical cue in the P-CeG signal (Figure 20A and 20B). Blebbistatin stops the binding of actin to myosin by blocking the myosin head without disturbing the CM's

calcium signaling pathways. Our results showed a continuous periodic activity in the P-CeG signal, even after injections of five increasing blebbistatin concentrations (Figure 20A). This persisting rhythmic signal confirmed the possibility of recording CMs' field potential using SPR in the absence of contractile motion, showing SPR's sensitivity to functional analysis of live excitable cells. No significant difference in the signal's period duration was observed, except for an increase in its variability (increased standard deviation in FWHM with increased blebbistatin concentration in Figure 20B). The weakened capability of CMs action potential conduction and maintenance is observed in the P-CeG signal as a change in the shape of signal periods with increasing blebbistatin concentrations (Figure 20A). Due to the non-ideal experimental conditions of our study, the shape change can also be attributed to the alteration of the cells' microenvironment. Minor changes in temperature and pH of the cellular microenvironment can affect molecular binding affinity and membrane protein conformation, thus disrupting CM's calcium handling.

On the other hand, using the charge variation computed from the excitable cell-SPR mathematical model, contracting CMs' signal features are compared as blebbistatin concentration increases. Figure 20A depicts the extracted signal features of the P-CeG signal (amplitude, FWHM, and cell signaling rate), and Figure 20B shows those of the field potential signal (DA, RA, and FPD). There was no significant difference between DA and RA of the charge variation. Since the development of the cell-SPR model in this dissertation requires more development, no further assumptions will be presented on DA and RA changes.

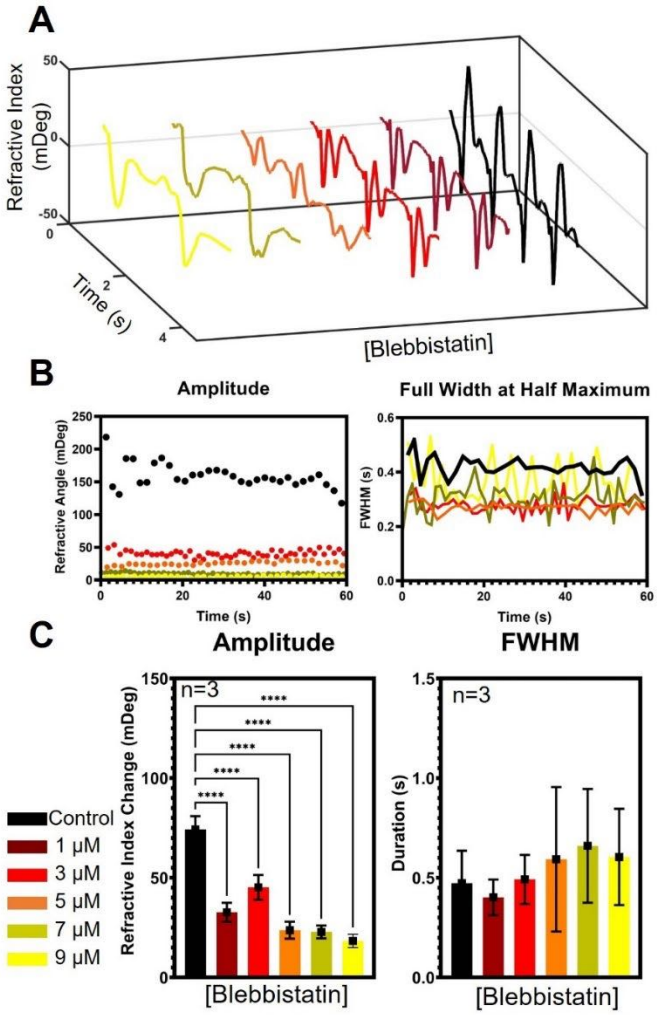

Figure 20. Blebbistatin studies on the P-CeG signal. A) Consecutive injections of 1, 3, 5, 7, and 9μM blebbistatin (maroon, red, orange, light green, and yellow, respectively) are shown. A continuous decrease in signal amplitude with the increase of blebbistatin concentration suggests the removal of a mechanical cue from the signal. B) Amplitude (left) and FWHM (right) for one CM-cultured sensor over time. A decrease of the control sample's (black circle markers) amplitude and high variability in the FWHM of data with time indicate decreased cellular functionality, presumably due to non-ideal experimental conditions. C) quantification of the P-CeG signal's amplitude and FWHM with increasing blebbistatin concentrations (n=3). Average data is reported as mean ± std: 1-way ANOVA, $p<0.0001$, 95% CI. Tukey's multiple comparisons test shows the significance of each concentration comparison with control to be (****).

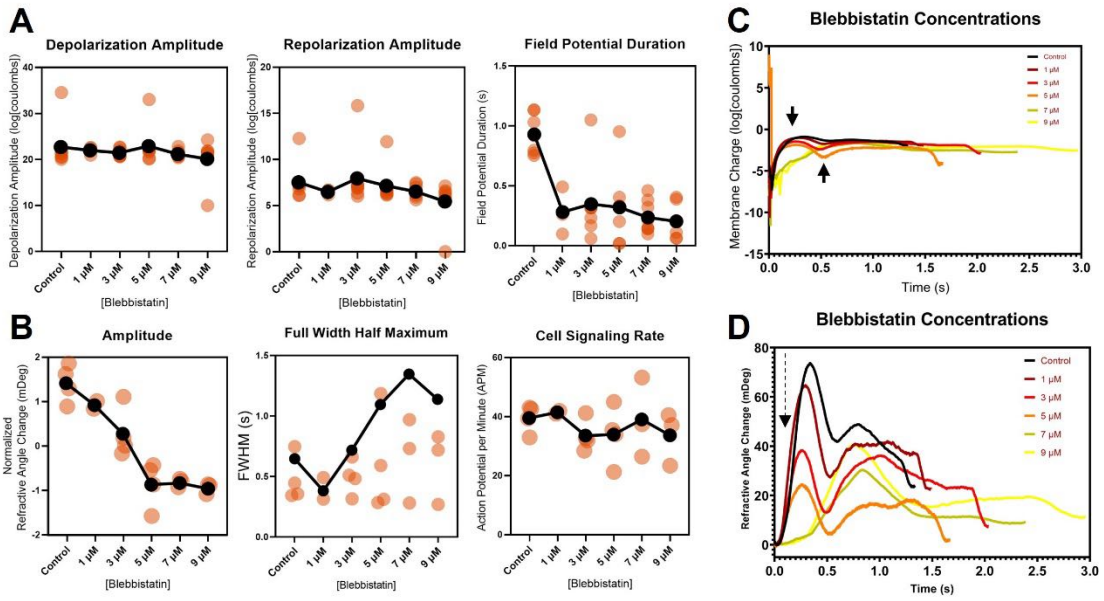

Figure 21. The P-CeG signal and the charge signal features during blebbistatin injections of 1, 3, 5, 7, and 9µM. A) Depolarization amplitude (DA), repolarization amplitude (RA), and field potential duration (FPD) of the charge. Orange circles are single datapoints from CM-cultured sensors' charge signal. Black circles are the mean for each feature data at its corresponding concentration. The black line depicts the trend of feature variation with increasing blebbistatin concentrations. No significant difference in DA and RA features was observed with increasing drug concentrations. On the other hand, FPD showed a decrease as blebbistatin concentration increased. B) Amplitude, FWHM, and cell signaling rate (left, middle, right, respectively) features of the P-CeG signal. While the signal's peak amplitudes decreased and FWHM showed higher variability, the cell signaling rate was relatively unchanged after subjecting the cells to five concentrations of blebbistatin. C) Charge graph of a single period from contracting CMs. Solid black arrows mark the location of extracellular membrane charge alteration with increasing blebbistatin concentration. D) The P-CeG signal of a single period from contracting CMs. Dashed black arrow shows the direction of amplitude decrease in the P-CeG signal with increasing blebbistatin concentrations.

Therefore, DA and RA variables of the signal must be analyzed using a complete mathematical model of excitable cell-SPR, where electrical and mechanical contraction effects can be extracted from the signal and studied separately. The FPD, on the other hand, is a temporal representation of the main ongoing events of contracting CMs under drug conditions; hence it is appropriate to analyzed based on the model presented. A sudden decrease in the duration of the field potential of contracting CMs with increased variability of the datapoints (Figure 21A*)* is consistent with the development of arrhythmias in CMs due to uncontrolled cellular microenvironment and interruption of CMs' calcium signaling. An overlay of increasing blebbistatin concentrations from both the field potential signal

(Figure 21C) and the P-CeG signal (Figure 21D) suggests the high sensitivity of SPR in characterizing excitable cell activities.

Verapamil Outcomes:

Verapamil limits the flow of Ca^{2+} into the CMs' cytosol through L-type Ca^{2+} channels. Blocking the L-type Ca^{2+} channels of contracting CMs will affect their action potential conduction, and hence, cellular contraction. Concentrations of verapamil injections were prepared from a stock solution of 2μM verapamil in ethanol. Concentrations of 50, 100, 200 and 500nM verapamil were selected for studying its effect on the P-CeG. Interestingly, we observed a sudden and sharp drop in the P-CeG signal amplitude even after addition of the lowest verapamil concentration (50nM, Figure 22A and 22C). This sharp drop in the signal's amplitude emphasizes the importance of Ca^{2+} in CMs' electromechanical functionality. An increase in the amplitude of the control data (black circles in Figure 22B, left) and a highly stable period duration for the control data (black line in Figure 22B, right) shows the presence of a relatively healthy cardiac syncytium on the sensor. Full width at half maximum (FWHM) data for contracting CMs post exposure to verapamil is not available due to a high signal noise after injections and

absence of a periodic signal. Verapamil injections confirm the sensitivity of SPR to membrane charge variation of contracting CMs.

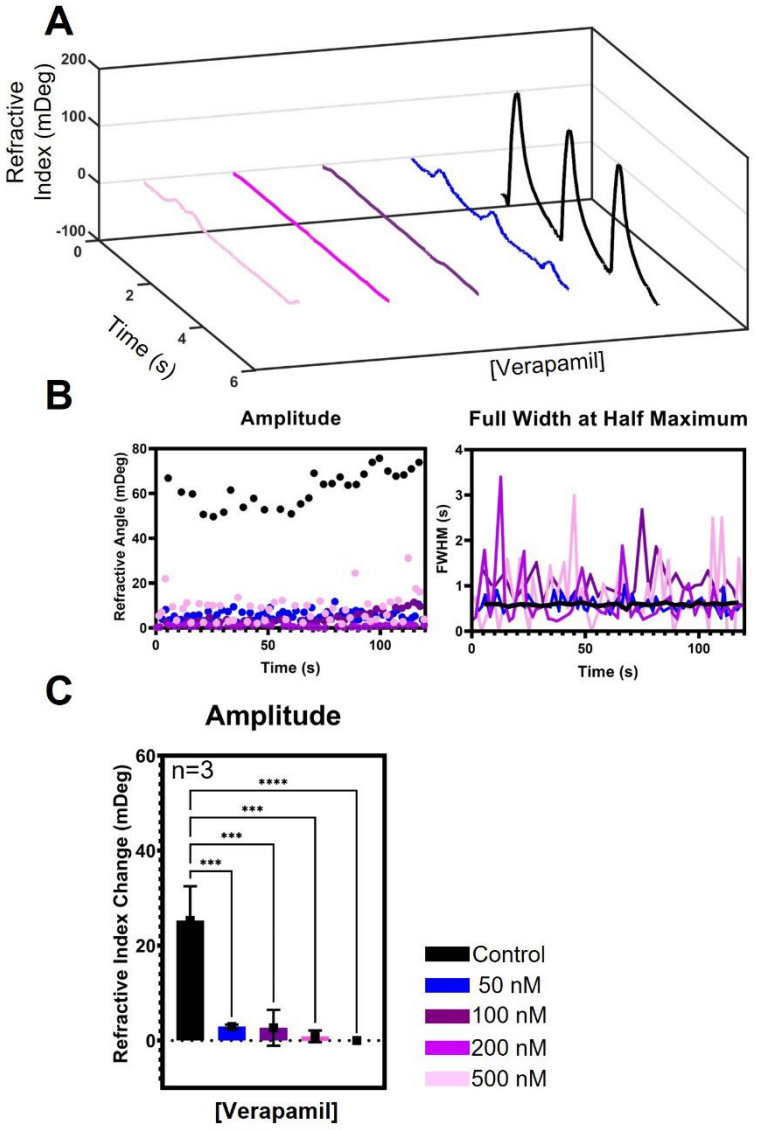

Figure 22. Studies on effects of Verapamil on the P-CeG signal. A) Consecutive injections of 50, 100, 200, and 500 nM verapamil (blue, purple, magenta, and light pink, respectively) are shown. Sharp decrease in signal amplitude with the increase of verapamil concentration shows the P-CeG signals' sensitivity to charge variations near CMs' plasma membrane. B) Amplitude (left) and FWHM (right) for one CM-cultured sensor over time. An increase of the control sample's (black circle markers, left) amplitude and a highly stable FWHM (black line, right) indicate the presence of a relatively healthy cardiac cell on the sensor. C) Quantification of the P-CeG signal's amplitude while increasing verapamil concentrations (n=3). Average data is reported as mean ± std: 1-way ANOVA, $p<0.0001$, 95% CI. Tukey's multiple comparisons test shows the significance of each concentration comparison with control $p<0.001$ (***), except for the 500 nM concentration, $p<0.0001$(****).

Feature extraction was conducted for the same variables as those of the blebbistatin injections. DA, and RA were relatively unchanged, while the field potential duration slightly increased (Figure 23A and 23C). This increase is consistent with exposure of contracting CMs to an antiarrhythmic drug like verapamil. A decrease in flow of Ca^{2+} into the cells extends the duration of cellular action potential conduction and hence their contraction. Moreover, decreased signal amplitude, increased FWHM, and cell signaling rate for verapamil injections on three CM-cultured sensors is consistent with the previously reported studies on CMs under verapamil injections (Figure 23B and 23D)[160].

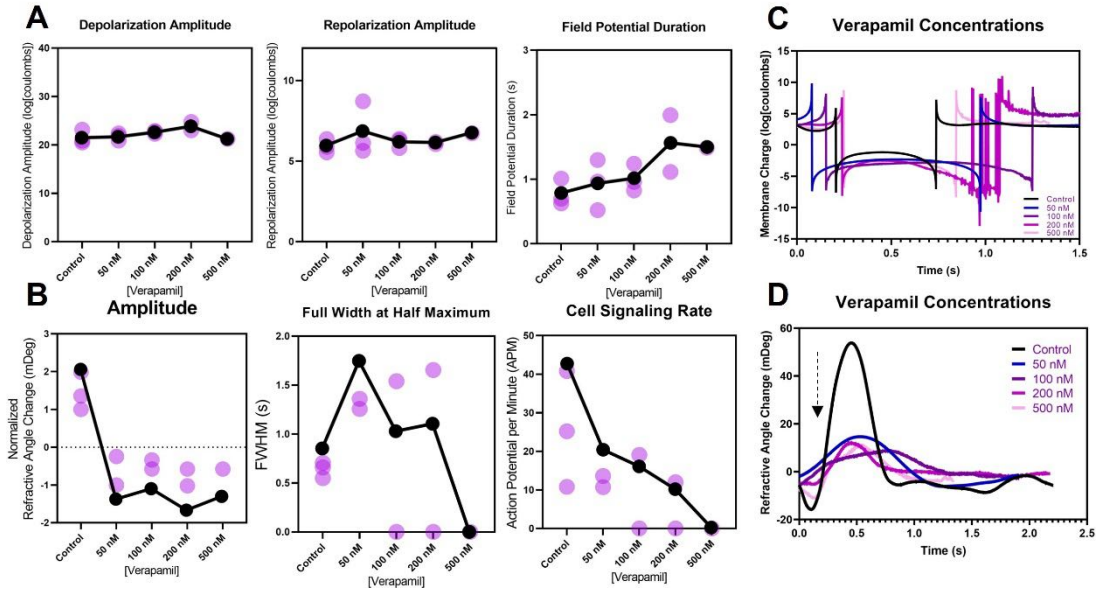

Figure 23. The P-CeG signal and the charge signal features during verapamil injections of 50, 100, 200, and 500nM. A) Depolarization amplitude (DA), repolarization amplitude (RA), and field potential duration (FPD) extracted from the field potential graph. Purple circles are single datapoints of each CM-cultured sensors' charge signal. Black circles are the mean for each feature data at its corresponding concentration. The black line depicts the trend of feature variation with increasing blebbistatin concentrations. No significant difference in DA and RA features was observed with increasing drug concentrations. On the other hand, FPD showed an increase as verapamil concentration increased. B) Amplitude, FWHM, and cell signaling rate (left, middle, right, respectively) features of the P-CeG signal. Signal's peak amplitudes and cell signaling rates decreased with increasing verapamil concentration, while the FWHM slightly increased before becoming undetectable and thus counted as zero. C, D) Charge graph and the P-CeG signal of a single period from contracting CMs. Increase in FPD and FWHM of the signals is distinctly observable with increasing verapamil concentrations (C and D, respectively).

Caffeine Outcomes:

Exposure of CM-cultured sensors to different caffeine concentrations was done to test whether the P-CeG signal is sensitive to changes in the contractile force of the CMs. Caffeine causes a decrease in rapid sarcoplasmic reticulum (SR) Ca^{2+} uptake, leaving the cytosol with less total exchangeable calcium content and then a fast increase in Ca^{2+} efflux from the SR[36,183]. As a result, this depletion of Ca^{2+} in the SR produces a stronger contractile force, given that an action potential has reached and stimulated the target CM. Four concentrations of caffeine (2, 4, 6, and 8 mM) were freshly prepared in HBSS buffer to test its effect on contracting CMs.

Serial caffeine injections of the abovementioned concentrations to CM-cultured gold sensors showed a sustained signal amplitude after 2mM. However, a decreased amplitude was observed for 4, 6 and 8mM caffeine in comparison with control data, which is likely due to non-ideal experimental conditions. Nevertheless, we do see a maintained signal amplitude, even after long experimental durations (30 minutes), which is consistent with depleting the SR of its Ca^{2+} storage in response to caffeine (Figure 24B and Figure 24C, left). No significant difference was observed amongst period durations (Figure 24B and 24C, right) with caffeine. The relative stability of a contraction period's duration over time is consistent with the depletion of Ca^{2+} from the SR and maintenance of cellular contraction. On the other hand, the rate of Ca^{2+} uptake through SERCA by sarcoplasmic reticulum is weakened due to caffeine stimulation. As a result, more time is needed for the sarcoplasmic reticulum to store and release adequate calcium for initiation of the next contraction cycle. The slight increase in the contraction period duration and the drop in the final concentration amplitude (Figure 24B and 24C) of the P-CeG signal might be due to

the weakened ability of CMs' SR in storing Ca^{2+} as well. Our results for the effect of caffeine on contracting CMs is consistent with previously reported studies[175,184] and we can conclude that the P-CeG signal is likely to be sensitive to both changes in membrane charge alterations and contraction force of live CMs. Feature extraction from the charge and the P-CeG signals of CMs' treated with caffeine (Figure 25A left and middle, respectively) showed a slight increase in the FPD, consistent with decreased availability of Ca^{2+} in the cytosol for cellular contraction (Figure 25A right and 25C). Furthermore, because of decreased Ca^{2+} availability over time, cell signaling rate (Figure 25B right) also decreased significantly as the concentration of caffeine increased.

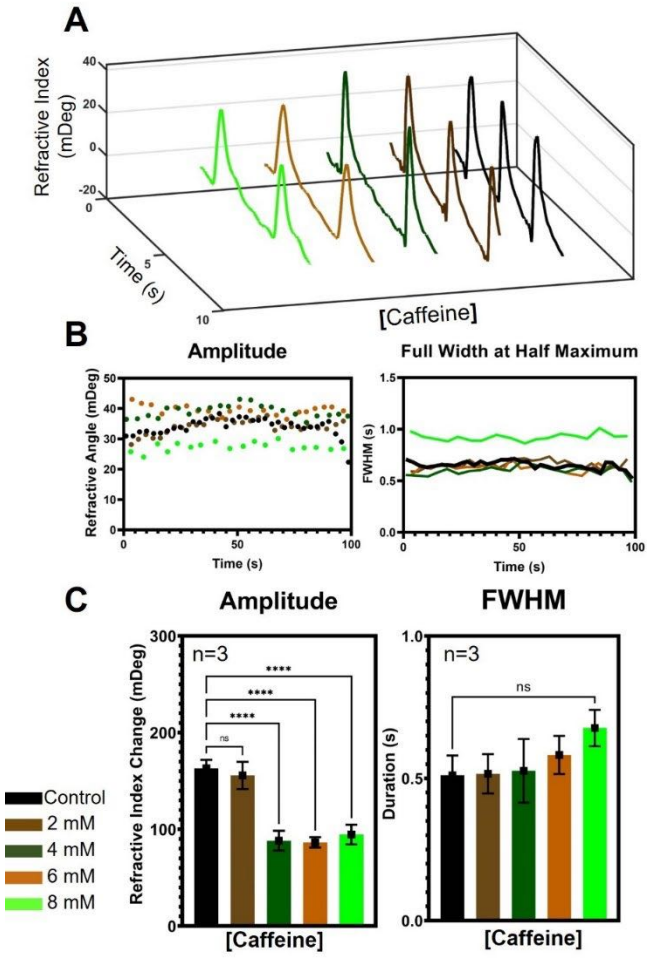

Figure 24. Caffeine studies on the P-CeG signal. A) Consecutive injections of 2, 4, 6, and 8-mM caffeine (dark brown, dark green, light brown, light green, respectively) are shown. Presence of a detectable signal amplitude with the increase of caffeine concentration shows the P-CeG signals' sensitivity to CM's force of contraction. B) Amplitude (left) and FWHM (right) for one CM-cultured sensor over time. C) Quantification of the P-CeG signal's amplitude for increasing caffeine concentrations (n=3). Average data is reported as mean ± std: 1-way ANOVA, $p<0.0001$, 95% CI. Tukey's multiple comparisons test shows the significance of signal's amplitude for all caffeine concentrations to be $p<0.0001$ (****), except for the nonspecific difference for 2mM caffeine.

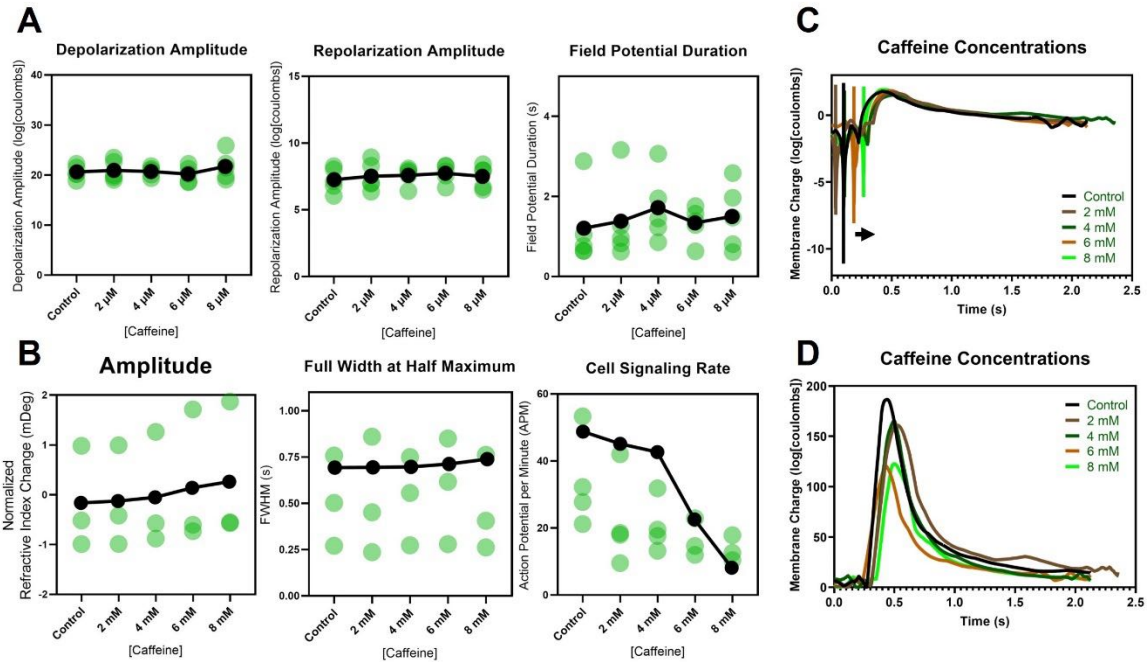

Figure 25. The P-CeG signal and the charge signal features with caffeine injections of 2, 4, 6, and 8mM. A) Depolarization amplitude (DA), repolarization amplitude (RA), and field potential duration (FPD) of the charge graph. Transparent green circles are single datapoints from CM-cultured gold sensors' charge signal. No significant difference in DA and RA features was observed with increasing drug concentrations. A slight increase in FPD might be due to non-ideal experimental conditions as well as the long-term effect of caffeine on CMs. B) Amplitude, FWHM, and cell signaling rate (left, middle, right, respectively) features of the P-CeG signal. Signal's peak amplitudes and FWHM is relatively unchanged with increased caffeine concentrations, while the cell signaling rate has decreased. C, D) Charge graph and the P-CeG signal of a single period from contracting CMs.

4.3.2 Drug-Cell Affinity Studies

SPR was designed originally for quantifying molecular binding kinetics. Here, we also took advantage of SPR's capability in quantifying molecular binding events for evaluating binding kinetics of different drugs with contracting CMs. A one-to-one Langmuir binding kinetic model was used for curve fitting purposes and computing binding variables. A one-to-one binding model assumes that the reaction between

immobilized ligand (L) and the target analyte (A) follows a first order kinetics equation[185]. The association rate constant, k_a, describes the rate of complex formation per second in a one molar solution of L and A. The dissociation rate constant, k_d, is the rate at which L and A get separated and is determined by the analyte and ligand's properties, temperature and buffer conditions. R_{max} is the maximum feasible SPR signal between a ligand-analyte pair, determined by the number of binding sites and the size of the ligand and analyte molecules. Last but not least, the equilibrium constant, K_D, is a ratio of analyte and ligand concentrations to that of the complex formations' concentration.

Results of verapamil, caffeine and blebbistatin binding to contracting CMs using SPR are depicted in Figure 26A-C, respectively. The so called SPR sensograms (Figure 26, left graphs) from experimental drug binding to CMs (black lines) and those from a fitted Langmuir model (red lines) suggest that another kinetic model (e.g., mass transfer) might be required for providing a better fit for verapamil and caffeine binding to their corresponding receptors. Nevertheless, an increase in analyte concentration of all three drugs resulted in an increase in SPR response as expected, which is shown in Figure 26A-C, right graphs. Values of the binding kinetics are extracted from three sample SPR sensograms for each drug, shown in table 4.1. As k_a values for biological systems are usually within 10^3 to 10^7 $M^{-1}s^{-1}$[1102,186,187], the k_a values for caffeine were unexpectedly low, which will most likely get resolved with a mass-transfer model.

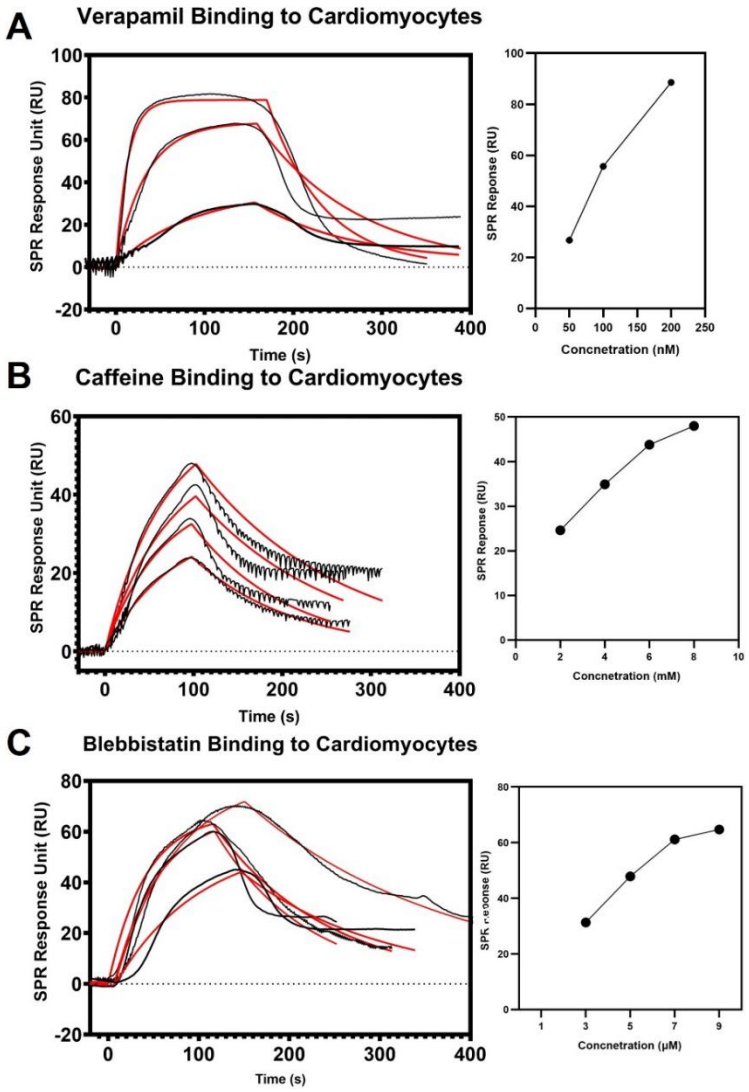

Figure 26. SPR bidning curves for drug studies. A, B, C left) Sensogram for binding of different concntrations of A) verapamil (from bottom to top: 50, 100 and 200nM), B) caffein (from bottom to top: 2, 4, 6, and 8mM), and blebbestatin (from bottom to top: 1, 3, 5, 7μM) to CMs. A, B, C right) SPR's response as a function of increasing analyte concnetration.

Table 4.1. Binding kinetics for verapamil, caffeine and blebbistatin using SPR

Substance	K_a ($M^{-1}s^{-1}$)	K_d (s^{-1})	K_D (M)	R_{MAX} (RU)
Verapamil	271797.57	0.012	$2.37*10^{-6}$	429.87
Caffeine	18.09	0.015	$0.97*10^{-3}$	860.57
Blebbistatin	6718.1	0.021	$3.77*10^{-6}$	3199.13

4.4 Chapter Outcome

The scientific community's demand is growing for a faster and more cost-efficient method for monitoring cell functionalities. Regenerative medicine using tissue engineering, novel drug development and drug toxicity studies are a few of the fields responsible for this demand. The Plasmonic Cardio Eukaryography (P-CeG) signal obtained from contracting CMs using SPR has previously shown promise in approaching this demand. However, uncertainties in signal's source, correlation to charge variability near CM's plasma membrane, as well as the cell-SPR studies being recently developed, makes SPR an unfamiliar method in cellular studies.

Therefore, we have explored the underlying events of contracting CMs using SPR through a mathematical model we developed for correlation of SPR response units to charge variations of contracting CMs. For better understanding of the live cell-SPR interaction, we explored the variability in CMs' function using blebbistatin, verapamil and caffeine as inhibitory and excitatory elements for CMs activity. We observed through drug studies that the P-CeG signal included inputs from both electrical and mechanical activities of CMs. These findings are critical not only in presenting a new perspective on live cell-SPR biophysical events, but also offering a more comprehensive sensing and stimulating platform compared to recent studies on plasmonic recordings of cell's electrical activity[188–190]. The previously established models of gold metal's electrical double layer for cell-SPR does not apply to spontaneously contracting cells and relies on a frequent electrical current induction to the surface of the gold metal for signal acquisition and analysis[109,111,189]. On the contrary, the platform developed in this dissertation is a label-free, standalone modality

for real-time recording of electrical and mechanical activities from spontaneously contracting CMs.

CHAPTER V. CONCLUDING REMARKS

5.1 Summary

Knowledge and information in cardiac medical sciences and cardiac bioengineering, from molecular to organ scale, have been growing rapidly since the 1980s with emerging new technologies. Since the new century, the exponential growth of information and technology increased hope in advancing therapeutics and diagnostics of cardiovascular diseases using novel drugs, regenerative medicine, and 3D printing of functional hearts. Nevertheless, safety regulations for the *in-vivo* application of such therapeutics and diagnostics play the most significant role in market availability. Failing novel drug safety regulations in clinical studies, leading to unsuccessful approval of the drug, comes from the discrepancies between the positive biological response in pre-clinical animal models to those of humans. To compensate for this gap and propel the successful translation of novel cardiac drugs to the clinic, heart-on-chip devices have emerged in the past couple of decades to assist with faster and higher throughput toxicity studies prior to clinical trials[83–87]. However, heart-on-chip devices are complex since providing a full cardiac tissue assessment chiefly requires monitoring cells' electrical and mechanical functionalities; thus, the complexity of designing a sensing device for simultaneously measuring CMs' electrical and mechanical functions. The work presented in this dissertation is the development of a novel on-chip sensing and stimulating technology for monitoring cardiomyocyte (CM) function using surface plasmon resonance (SPR) as a fast, label-free, and cost-efficient standalone methodology.

In Chapter 2, we explored the potential of the SPR instrument in extracting contraction profiles from live cardiomyocytes (CMs). Observing a rhythmic SPR signal

from contracting CMs cultured on gold sensors intrigued us to correlate the obtained SPR response unit (mDeg) to action potential associated charge variations near the cell's plasma membrane. Thus, we developed a mathematical model of the excitable cell-SPR, which showed the correlation between the SPR signal and CMs' charge variations over time. The contraction profile obtained from SPR was named the Plasmonic Cardio-Eukaryography (P-CeG) signal, as it is a relatively comprehensive method for monitoring a single cardiac cell or a monolayer of cells (i.e., cardiac syncytium) function. The P-CeG signal feature variations were analyzed with different cell culture medium flow rates, showing 10μL/min suitable for obtaining the highest signal-to-noise ratio. The force of contraction from CMs cultured on gold sensors was extracted using microscopy, offering a different route through SPR imaging for cardiac cell inotropy. The excitable cell-SPR correlation guided our further signal exploration in Chapter 3.

In Chapter 3 we delved into understanding the P-CeG signal's complexities, such as its dominant repeating frequencies. Three dominant frequencies were confirmed using short-time Fourier transform and signal decomposition using wavelet transforms. While one frequency might be closely correlated to cell beat rate, the other frequency suggests its possible cause to be the cells' ion transport driven action potential (opening of fast Na^+ channels and Ca^{2+} channels). We suspect the source of the third frequency being a few possible events; the return wave of medium displacement due to cell contraction, higher frequency physiological events of the plasma membrane (e.g., activity of exchanger pumps) and cell membrane deformations, to name a few. Furthermore, we extracted the byproducts of the P-CeG signal, such as current flow alterations during a CM contraction period, using the derivative of the charge variation profile. Current flow alterations are

specifically crucial to recording CMs' behavior in real-time, which will prove helpful in tracking cellular events of clinical importance, like the early afterdepolarization (EAD) phenomenon.

In chapter 4 we investigated the P-CeG signal's sensitivity to different drug stimulations, inhibiting or promoting CM activity. We also used this paradigm to further explore the underlying physiological cause of the three frequencies in the P-CeG signal. Blebbistatin, verapamil and caffeine were used as a myosin head inhibitor, Ca^{2+} channel blocker and force of contraction promoter, respectively. The blebbistatin results specifically supports the possible presence of a mechanical component of the CMs contraction in the P-CeG signal. Results from drug stimulation provided information on specific drug binding to cardiac cells and showed a detectable significant change in the P-CeG signal during drug exposure.

Although doubts persist in establishing a sensitive and selective SPR device as a standardized modality for recording live-cell activity, the results of this dissertation offer great promise in the field of comprehensive excitable cell analysis.

5.2 Future Directions

5.2.1 Evolving the Mathematical Model and the P-CeG Signal Study

The excitable cell-SPR model developed in this dissertation can serve as an elementary model in the initial understanding of the P-CeG signal and its cause. Our mathematical model is developed based on the law of conservation of energy in a selected confined space housing the CMs cultured on thin gold sensors. This confined space includes two major components: 1) detection area for a thin gold sensor and its electron density cloud and 2) a network of connected CM's plasma membranes and less than 50nm

of the cells' cytosol beyond the plasma membrane. The energy of the polarized light, which excites the surface plasmons and gives rise to the evanescent wave, is transformed into kinetic and potential energy for each of the selected confined spaces' components. For simplicity, we assumed the effect of turbulence kinetic energy to be infinitesimal and omitted it from the model. The alterations in the electrostatic potential due to the interaction of the two components of the confined space will affect the total return energy of the reflected light, hence changing its refraction angle. Quantitative CMs electromechanical activity using SPR requires the development of a mature mathematical model. The inclusion of kinetic energy vectors resulting from cell contraction in the excitable cell-SPR model will facilitate the measurement of contractile force with high spatiotemporal resolution directly from the P-CeG signal.

On the other hand, the complexities and components of the P-CeG signal need further investigation. For example, signal entropy measures, such as Shannon, spectral and sample entropy[191] will help determine the stability of the P-CeG signal variables across different sensors using SPR. Entropy measures are commonly used to minimize data loss in signal analysis after signal noise reduction[191,192]. Signal stability analysis using entropy can help identify missing points in the signal, clarify the signal's directionality and causality, and detect hidden signal features, such as a low-frequency contraction force event. For example, a sample entropy threshold application to uterine extracted electromyography datasets has successfully distinguished between pregnancy and labor contraction bursts[193]; the same concept can be applied to the force developed from healthy and diseased CMs. Furthermore, sample entropy and spectral entropy have been employed as a non-linear mean to discern between healthy and diseased electrocardiogram (ECG)

signal irregularities and electroencephalogram (EEG) sample datasets[194,195]. The entropy measures in signal processing of ECG and EEG samples have been used to diagnose cardiac arrhythmias and epileptic episodes, respectively[192,194,196]. Moreover, mathematical tools such as principal component analysis of the P-CeG signal's decomposed wavelets result in a more optimized reconstruction of the signal, which might be crucial for preserving signal components.

5.2.2 Cell Isolation and Culture Enhancements

The CM isolation protocol followed in this dissertation includes the extraction and digestion of neonatal rat hearts and promoting the proliferation of CMs over fibroblasts and endothelial cells[120]. The protocol does not distinguish between CMs of different origins (e.g., ventricular, or atrial). Cardiac cells of different developmental origins express distinctive genetic profiles and electrophysiological characteristics[106]. Sinoatrial and atrioventricular CMs, which are responsible for action potential generation and conduction in the heart, spontaneously contract, while the ventricular CMs rely on the nodal cells to provide them with the cue for contraction. Thus, a CM extraction protocol with cell-specific isolation methodology is recommended for future experiments regarding P-CeG signal acquisition[129,197].

Furthermore, intracellular organelles such as the mitochondrion and the nucleus indirectly contribute to the cellular contraction-relaxation event by accumulating calcium ions for gene expression regulations[183]. Therefore, electrophysiological studies of CMs using SPR might benefit from a more advanced sensor surface modification, sensor surface patterning, and single CM alignment on the sensor than presented in this dissertation.

Another critical factor in CMs' electrophysiology is the consistent provision of physiological level of oxygen to the cells. Oxygen is vitally important in the pathophysiology of myocardial injury. Ischemia effects on cardiac cells can be observed in beating frequency and beating force alterations, irregular beating profile, and tissue death[198]. In summary, obtaining the P-CeG signal under more physiological conditions (37ºC and pH=7.2-7.4) with a regulated oxygen supply might reveal more reliable information regarding real-time CMs electromechanical functionality.

5.2.3 Advanced Clinical Application

One of the essential measures of the voltage-gated ion channel activities obtained through patch clamping is the channels' conductance and their contribution to the cell's membrane potential at each point in time. Investigating cardiac channelopathies and their developmental pathway partially relies on the information provided from whole-cell patch clamps of different voltage-gated channels[199]. A plasmonic experimental design with drug inhibitors and promoters of the CMs' principal voltage-gated channels involved in their excitation-contraction event will provide complementary information comparable to those obtained through a patch-clamp regarding CMs electrophysiology. For example, using lidocaine and verapamil as Na^+ channel and Ca^{2+} channel blockers, respectively, will simplify the following membrane potential equation by removing the target channel conductance:

$$E_m = \frac{g_{Na}}{g_{tot}} E_{Na} + \frac{g_K}{g_{tot}} E_K + \frac{g_{Ca}}{g_{tot}} E_{Ca} \quad \text{(Equation 22)}$$

Where E_m is the total membrane potential, g_{Na}, g_K, and g_{Ca} are the electrical conductance for each corresponding ion, g_{tot} is the total membrane conductance, and E_{Na}, E_K, and E_{Ca} are equilibrium potential for each type of ion. Solving the matrix of equations based on the

abovementioned process can determine unknown values of membrane ion conductance in CMs using SPR. Measuring the electrical conductance of ions is beneficial in studying CM disease models, such as the Long-QT syndrome and Brugada syndrome[199].

Another important application of plasmonic-based cell behavior analysis is evaluating the cardiotoxicity of newly developed drugs. Incubating the cultured CMs on SPR gold sensors with different concentrations of cardiotoxic drugs such as Doxorubicin[54,200] for different durations will provide researchers with real-time and label-free data acquisition of CMs' electromechanical function in response to toxicity. Finally, extracting clinically valuable information from the P-CeG signal, such as heart rate variability (HRV), action potential durations (ADP) and upstroke velocity of the action potential will serve in determining the underlying cause of cardiac arrhythmias.

Overall, this dissertation sets a foundation for a comprehensive label-free, real-time, and quantifiable plasmonic characterization of live excitable cells, such as CMs, under normal and perturbed conditions. We hope that the results depicted in this work interest current and future scientists in advancing the applications of the P-CeG signal.

5.3 Proposed Future Experiments

5.3.1 Validating Excitable Cell-SPR Drug Stimulation Studies:

Chapter 4 of this dissertation suggests that SPR can possibly obtain a specific and sensitive electrophysiological response from live CMs stimulated with three drugs: Blebbistatin, Verapamil, and Caffeine. The specificity of the plasmonic response of CM-cultured sensors to different drugs comes from the target drug's molecular weight, solvent material composition and the drug's effect on CMs' electrophysiology. The sensitivity of the plasmonic response to electrophysiological alterations of cells under drug-stimulation,

however, should be further validated with a standard empirical methodology. For example, our P-CeG signal recordings from blebbistatin-treated cardiac cells shows a decreased amplitude and change in the periods' shape post exposure, with persistent occurrence of the rhythmic signal.

Blebbistatin halts CM contraction; hence, with increasing blebbistatin concentration from 1-9μM, we expect the cellular motion to be fully stopped and to not be a contributor to the produced signal. But since the presence of a rhythmic response persists, we initially assumed that it might be due to ongoing action potential activity in CMs, despite their ceased mechanical activity. We, therefore, initially hypothesized that the optical response from CMs using SPR might be obtaining both electrical and mechanical elements of CMs' contraction. Yet, another explanation can be associated with the saturation level of blebbistatin conjugation to the myosin head cleft across all sarcomeric elements in the SPR's detection area. The rhythmic response post blebbistatin exposure might be a result of single sarcomeres not being affected by blebbistatin and yet contracting in response to receiving action potentials across the cellular network.

A gold standard methodology in quantifying CM electromechanical activity is the combination use of microelectrodes and fluorescent microscopy. A single microelectrode or a configuration of microelectrode arrays can be used to quantify charge transfer across CMs' cellular network on gold sensors in a dish on top of a microscope's objective, where real-time recording of cellular contraction takes place. Based on the plasmonic response analysis of blebbistatin-CM interaction, we expect to see a time and concentration dependent decrease in force of contraction across the observation area with increasing blebbistatin concentration. Force measurements are exploited from real-time brightfield or

fluorescent recordings of cellular contraction fairly simply with currently available open-access software such as MUSCLEMOTION[201]. On the other hand, we expect the microelectrodes to demonstrate a continuous recording of CMs' action potentials before and after blebbistatin addition. We expect an increase in cardiac action potential time-dependent properties' variability (e.g., action potential duration) post blebbistatin exposure. Investigating the abovementioned experimental results can shed more light on the realistic effect of blebbistatin on a cardiac syncytium on gold sensors, hopefully fortifying our previous electrophysiological interpretation of the P-CeG signal.

Furthermore, a non-contractile excitable cell model, such as a neuron-on-chip, might serve as a simplified excitable cell-SPR, where possibly the majority of a rhythmic signal (if obtained) will be as a result of action potential propagation and its interaction with the free electron density cloud of gold metal.

5.3.2 Respiratory and Metabolism Characterization of CMs Using SPR

Distribution and uptake of oxygen differs within each cell based on the targeted organelle and is very difficult to track. The physiological healthy oxygen concentration varies between a limit of 1-10%, while oxygen concentration lower than 1% could indicate necrosis or inflammation of tissue[198]. Such distinct criteria make oxygen an accurate indicator of cell health. In case of cardiac cells, oxygen is vitally important in pathophysiology of myocardial injury. The effect of ischemia, or low oxygenation of cardiac cells, can be observed in terms of beating frequency and strength change, irregular beating profile and cell death[202,203].

As previously mentioned, the BI2000 SPR device provides a sealed environment after assembly of the sensor and microfluidic module that stops cellular gas exchange with

the outside environment. Our speculation suggests that if a static (i.e., no flow) excitable-cell SPR experiment is carried out, the P-CeG signal may show characteristics of cellular apoptosis, even in the early minutes of experiment initiation. The P-CeG signal's characteristics showing cell death might be a high variation in CM beat-rate variability over time, which is a marker of unhealthy calcium handling of CMs, or a sharp and continuous drift in the signal's baseline. The trend by which the P-CeG signal reaches its final hallmark of apoptosis might serve effectively in understanding ongoing cellular and subcellular events in CMs in response to oxygen deficiency. An excitable cell-SPR experiment using the microfluidic sealing module, with and without flow, can open a new line in grasping CM respiration. Furthermore, the BI2000 SPR device also includes an electrochemical module, which is sealed on top of the CM-cultured sensors from the bottom but is open on top for inserting working and counter/reference electrodes. Using the electrochemical module with our previously established experimental design can extend the knowledge of CM respiration under flow and static conditions in open gas exchange as well as sealed environments.

Moreover, to fortify the abovementioned speculation and forming a hypothesis, a previously established plasmonic experimental methodology[204] can be adapted with few modifications in our studies to quantify the release of hypoxia-induced factor (HIF) from CMs. Cardiac cells may be cultured in the channels of the microfluidic module, instead of on gold sensors. While microchannels facilitate CM growth and network formation due to the channel's rectangular and elongated structure, the P-CeG signal might not form, since cells are not directly linked to the gold sensor. However, the surface of the gold sensor can be modified with anti-HIF antibodies and SPR can be employed in its classic mode for

molecular interaction and quantification of HIF release from CMs under different flow conditions.

REFERENCES:

1. Shah, P., Zhu, X., Zhang, X., He, J. & Li, C. Z. Microelectromechanical System-Based Sensing Arrays for Comparative in Vitro Nanotoxicity Assessment at Single Cell and Small Cell-Population Using Electrochemical Impedance Spectroscopy. *ACS Appl. Mater. Interfaces* **8**, 5804–5812 (2016).
2. Singha, M. K. & Nagaraju, J. Design simulation and fabrication of 3D electrode for dielectrophoretic chip. *ISPTS 2015 - 2nd Int. Symp. Phys. Technol. Sensors Dive Deep Into Sensors, Proc.* 192–195 (2015) doi:10.1109/ISPTS.2015.7220110.
3. Alexander, F., Eggert, S. & Wiest, J. A novel lab-on-a-chip platform for spheroid metabolism monitoring. *Cytotechnology* **70**, 375–386 (2018).
4. Jung, J., Lee, J., Shin, S. & Tae Kim, Y. Development of a telemetric, miniaturized electrochemical amperometric analyzer. *Sensors (Switzerland)* **17**, (2017).
5. Bunge, F. *et al.* Microfluidic oxygen sensor system as a tool to monitor the metabolism of mammalian cells. *Sensors Actuators B Chem.* **289**, 24–31 (2019).
6. Jeong, S. H., Lee, D. W., Kim, S., Kim, J. & Ku, B. A study of electrochemical biosensor for analysis of three-dimensional (3D) cell culture. *Biosens. Bioelectron.* **35**, 128–133 (2012).
7. Bonk, S. M. *et al.* Design and characterization of a sensorized microfluidic cell-culture system with electro-thermal micro-pumps and sensors for cell adhesion, oxygen, and pH on a glass chip. *Biosensors* **5**, 513–536 (2015).
8. Wu, C. *et al.* Real-Time Evaluation of Live Cancer Cells by an *in Situ* Surface Plasmon Resonance and Electrochemical Study. *ACS Appl. Mater. Interfaces* **7**, 24848–24854 (2015).
9. Mirtaheri, E., Dolatmoradi, A. & El-Zahab, B. Thermally Assisted Acoustofluidic Separation Based on Membrane Protein Content. *Anal. Chem.* **91**, 13953–13961 (2019).
10. Akbar, M., Restaino, M. & Agah, M. Chip-scale gas chromatography: From injection through detection. *Microsystems Nanoeng.* **1**, (2015).
11. Ahrberg, C. D., Manz, A. & Chung, B. G. Polymerase chain reaction in microfluidic devices. *Lab Chip* **16**, 3866–3884 (2016).
12. Chiriacò, M. S. *et al.* Lab-on-chip for exosomes and microvesicles detection and characterization. *Sensors (Switzerland)* **18**, (2018).
13. Jeong, H., Adv, S., Jeong, H., Rogers, J. A. & Xu, S. Continuous on-body sensing for the COVID-19 pandemic : Gaps and opportunities. *Sci. Adv.* **4794**, eabd4794 (2020).
14. Gué, A. M., Tap, H., Gros, P. & Maury, F. A miniaturised silicon based enzymatic biosensor: Towards a generic structure and technology for multi-analytes assays. *Sensors Actuators, B Chem.* **82**, 227–232 (2002).

15. Ravikumar, S., Baylon, M. G., Park, S. J. & Choi, J. il. Engineered microbial biosensors based on bacterial two-component systems as synthetic biotechnology platforms in bioremediation and biorefinery. *Microb. Cell Fact.* **16**, 1–10 (2017).

16. Grattieri, M. & Minteer, S. D. Self-Powered Biosensors. *ACS Sensors* **3**, 44–53 (2018).

17. Endo, T. *et al.* Multiple label-free detection of antigen-antibody reaction using localized surface plasmon resonance-based core-shell structured nanoparticle layer nanochip. *Anal. Chem.* **78**, 6465–6475 (2006).

18. Ritzefeld, M. & Sewald, N. Real-Time Analysis of Specific Protein-DNA Interactions with Surface Plasmon Resonance. *J. Amino Acids* **2012**, 1–19 (2012).

19. Zhu, Y., Chandra, P., Ban, C. & Shim, Y. B. Electrochemical Evaluation of Binding Affinity for Aptamer Selection Using the Microarray Chip. *Electroanalysis* **24**, 1057–1064 (2012).

20. Ghaffari, R. *et al.* Soft Wearable Systems for Colorimetric and Electrochemical Analysis of Biofluids. *Adv. Funct. Mater.* **1907269**, 1–10 (2019).

21. Lee, Y. K. *et al.* Room Temperature Electrochemical Sintering of Zn Microparticles and Its Use in Printable Conducting Inks for Bioresorbable Electronics. *Adv. Mater.* **29**, 1–8 (2017).

22. Bandodkar, A. J. *et al.* Battery-free, skin-interfaced microfluidic/electronic systems for simultaneous electrochemical, colorimetric, and volumetric analysis of sweat. *Sci. Adv.* **5**, 1–16 (2019).

23. Endo, T., Kerman, K., Nagatani, N., Takamura, Y. & Tamiya, E. Label-Free Detection of Peptide Nucleic Acid-DNA Hybridization Using Localized Surface Plasmon Resonance Based Optical Biosensor. *Anal. Chem.* **77**, 6976–6984 (2005).

24. He, P., Liu, L., Qiao, W. & Zhang, S. Ultrasensitive detection of thrombin using surface plasmon resonance and quartz crystal microbalance sensors by aptamer-based rolling circle amplification and nanoparticle signal enhancement. *Chem. Commun.* **50**, 1481–1484 (2014).

25. Devadhasan, J. P., Kim, S. & An, J. Fish-on-a-chip: a sensitive detection microfluidic system for Alzheimer's disease. *J. Biomed. Sci.* **18**, 33 (2011).

26. Shah, P. *et al.* PC12 cell integrated biosensing neuron devices for evaluating neuronal exocytosis function upon silver nanoparticles exposure. *Sci. China Chem.* **58**, 1600–1604 (2015).

27. Miller, J. S. *et al.* Rapid casting of patterned vascular networks for perfusable engineered three-dimensional tissues. *Nat. Mater.* **11**, 768–774 (2012).

28. Zhang, Y. S. *et al.* Multisensor-integrated organs-on-chips platform for automated and continual in situ monitoring of organoid behaviors. *Proc. Natl. Acad. Sci.* **114**, E2293–E2302 (2017).

29. Reboud, J. *et al.* Paper-based microfluidics for DNA diagnostics of malaria in low resource underserved rural communities. *Proc. Natl. Acad. Sci. U. S. A.* **116**, 4834–4842 (2019).

30. Li, C. Z. *et al.* Paper based point-of-care testing disc for multiplex whole cell bacteria analysis. *Biosens. Bioelectron.* **26**, 4342–4348 (2011).

31. Hindson, B. J. *et al.* High-throughput droplet digital PCR system for absolute quantitation of DNA copy number. *Anal. Chem.* **83**, 8604–8610 (2011).

32. Nicholas Dias, Yung Peng, R. K. Fluorogenic DNA Sequencing in PDMS Microreactors Peter. *Physiol. Behav.* **176**, 139–148 (2017).

33. Liu, Y., Chen, X., Zhang, Y. & Liu, J. Advancing single-cell proteomics and metabolomics with microfluidic technologies. *Analyst* **144**, 846–858 (2019).

34. Larsen, S. T. & Taboryski, R. All polymer chip for amperometric studies of transmitter release from large groups of neuronal cells. *Analyst* **137**, 5057 (2012).

35. Frey, N. & Olson, E. N. Cardiac Hypertrophy: The Good, the Bad, and the Ugly. *Annu. Rev. Physiol.* **65**, 45–79 (2003).

36. Ronaldson-Bouchard, K. *et al.* Advanced maturation of human cardiac tissue grown from pluripotent stem cells. *Nature* **556**, 239–243 (2018).

37. Zhang, D. *et al.* Tissue-engineered cardiac patch for advanced functional maturation of human ESC-derived cardiomyocytes. *Biomaterials* **34**, 5813–5820 (2013).

38. Ott, H. C. *et al.* Perfusion-decellularized matrix: Using nature's platform to engineer a bioartificial heart. *Nat. Med.* **14**, 213–221 (2008).

39. Narsinh, K. H., Plews, J. & Wu, J. C. Comparison of human induced pluripotent and embryonic stem cells: Fraternal or identical twins? *Mol. Ther.* **19**, 635–638 (2011).

40. Knight, M. B., Drew, N. K., McCarthy, L. A. & Grosberg, A. Emergent Global Contractile Force in Cardiac Tissues. *Biophys. J.* **110**, 1615–1624 (2016).

41. Fleischer, S. *et al.* Albumin fiber scaffolds for engineering functional cardiac tissues. *Biotechnol. Bioeng.* **111**, 1246–1257 (2014).

42. Fleischer, S., Shapira, A., Feiner, R. & Dvir, T. Modular assembly of thick multifunctional cardiac patches. *Proc. Natl. Acad. Sci.* **114**, 1898–1903 (2017).

43. Radisic, M. *et al.* High-density seeding of myocyte cells for cardiac tissue engineering. *Biotechnol. Bioeng.* **82**, 403–414 (2003).

44. Marsano, A. *et al.* Beating heart on a chip: a novel microfluidic platform to generate functional 3D cardiac microtissues. *Lab Chip* **16**, 599–610 (2016).

45. Feiner, R. *et al.* Engineered hybrid cardiac patches with multifunctional electronics for online monitoring and regulation of tissue function. *Nat. Mater.* **15**, 679–685 (2016).

46. Beaulieu, D. R., Davison, I. G., Kılıç, K., Bifano, T. G. & Mertz, J. Simultaneous multiplane imaging with reverberation two-photon microscopy. *Nat. Methods* **17**, 283–286 (2020).

47. Mostovych, N. A. *et al.* Digital image capture for high-resolution medical x-ray diagnostics. **2**, 13 (2018).

48. Pollock, C. *et al.* PWM as a low cost method for the analog control of MEMS devices. *J. Microelectromechanical Syst.* **28**, 245–253 (2019).

49. Hersch, N. *et al.* The constant beat: cardiomyocytes adapt their forces by equal contraction upon environmental stiffening. *Biol. Open* **2**, 351–361 (2013).

50. Shradhanjali, A., Riehl, B. D., Duan, B., Yang, R. & Lim, J. Y. Spatiotemporal Characterizations of Spontaneously Beating Cardiomyocytes with Adaptive Reference Digital Image Correlation. *Sci. Rep.* **9**, 1–10 (2019).

51. Obien, M. E. J., Deligkaris, K., Bullmann, T., Bakkum, D. J. & Frey, U. Revealing neuronal function through microelectrode array recordings. *Front. Neurosci.* **9**, 423 (2015).

52. Wheelwright, M. *et al.* Investigation of human iPSC-derived cardiac myocyte functional maturation by single cell traction force microscopy. *PLoS One* **13**, 1–17 (2018).

53. Liu, J., Sun, N., Bruce, M. A., Wu, J. C. & Butte, M. J. Atomic force mechanobiology of pluripotent stem cell-derived cardiomyocytes. *PLoS One* **7**, (2012).

54. Zhang, X., Wang, T., Wang, P. & Hu, N. High-throughput assessment of drug cardiac safety using a high-speed impedance detection technology-based heart-on-a-chip. *Micromachines* **7**, (2016).

55. Huebsch, N. *et al.* Automated video-based analysis of contractility and calcium flux in human-induced pluripotent stem cell-derived cardiomyocytes cultured over different spatial scales. *Tissue Eng. - Part C Methods* **21**, 467–479 (2015).

56. Mozneb, M. & Mirza, A. Non-Invasive Plasmonic Based Real Time Characterization of Cardiac Drugs on Cardiomyocytes Functional Behavior. (2019) doi:10.1021/acs.analchem.9b04956.

57. Lindau, M. High resolution electrophysiological techniques for the study of calcium-activated exocytosis. *Biochim. Biophys. Acta - Gen. Subj.* **1820**, 1234–1242 (2012).

58. Zhang *et al.* Responsiveness of voltage-gated calcium channels in SH-SY5Y human neuroblastoma cells on quasi-three-dimensional micropatterns formed with poly (l-lactic acid). *Int. J. Nanomedicine* 93 (2013) doi:10.2147/ijn.s38362.

59. Morad, M. & Soldatov, N. Calcium channel inactivation: possible role in signal transduction and Ca2+ signaling. *Cell Calcium* **38**, 223–31 (2005).

60. Hazeltine, L. B. *et al.* Effects of substrate mechanics on contractility of cardiomyocytes generated from human pluripotent stem cells. *Int. J. Cell Biol.* **2012**, (2012).

61. Kreysing, E., Hassani, H., Hampe, N. & Offenhäusser, A. Nanometer-Resolved Mapping of Cell-Substrate Distances of Contracting Cardiomyocytes Using Surface Plasmon Resonance Microscopy. *ACS Nano* **12**, 8934–8942 (2018).

62. Howe, C. L. *et al.* Surface Plasmon Resonance Imaging of Excitable Cells. (2018) doi:10.1088/1361-6463/aaf849.

63. Carrier, R. L. *et al.* Cardiac tissue engineering: Cell seeding, cultivation parameters, and tissue construct characterization. *Biotechnol. Bioeng.* **64**, 580–589 (1999).

64. Zhang, J., Zhu, W., Radisic, M. & Vunjak-Novakovic, G. Can We Engineer a Human Cardiac Patch for Therapy? *Circ. Res.* **123**, 244–265 (2018).

65. Taegtmeyer, H. *et al. Assessing Cardiac Metabolism*. *Circulation Research* vol. 118 (2016).

66. Dhahri, W., Romagnuolo, R. & Laflamme, M. A. Training heart tissue to mature. *Nat. Biomed. Eng.* **2**, 351–352 (2018).

67. Scuderi, G. J. & Butcher, J. Naturally engineered maturation of cardiomyocytes. *Front. Cell Dev. Biol.* **5**, 1–28 (2017).

68. Saini, H., Navaei, A., Van Putten, A. & Nikkhah, M. 3D Cardiac Microtissues Encapsulated with the Co-Culture of Cardiomyocytes and Cardiac Fibroblasts. *Adv. Healthc. Mater.* **4**, 1961–1971 (2015).

69. Camelliti, P., Borg, T. K. & Kohl, P. Structural and functional characterisation of cardiac fibroblasts. *Cardiovasc. Res.* **65**, 40–51 (2005).

70. Kujala, K. *et al.* Electrical field stimulation with a novel platform: Effect on cardiomyocyte gene expression but not on orientation. *Int. J. Biomed. Sci.* **8**, 109–120 (2012).

71. Bird, S. D. *et al.* The human adult cardiomyocyte phenotype. *Cardiovasc. Res.* **58**, 423–434 (2003).

72. Kolwicz, S. C., Purohit, S. & Tian, R. Cardiac metabolism and its interactions with contraction, growth, and survival of cardiomyocytes. *Circ. Res.* **113**, 603–616 (2013).

73. Ganji, Y. *et al.* Cardiomyocyte behavior on biodegradable polyurethane/gold nanocomposite scaffolds under electrical stimulation. *Mater. Sci. Eng. C* **59**, 10–18 (2016).

74. Nitsan, I., Drori, S., Lewis, Y. E., Cohen, S. & Tzlil, S. Mechanical communication in cardiac cell synchronized beating. *Nat. Phys.* **12**, (2016).

75. Kong, M. *et al.* Cardiac Fibrotic Remodeling on a Chip with Dynamic Mechanical Stimulation. *Adv. Healthc. Mater.* **8**, 1–13 (2019).

76. Krook-Magnuson, E., Armstrong, C., Oijala, M. & Soltesz, I. On-demand optogenetic control of spontaneous seizures in temporal lobe epilepsy. *Nat. Commun.* **4**, 1–8 (2013).

77. Zgierski-Johnston, C. M. *et al.* Cardiac pacing using transmural multi-LED probes in channelrhodopsin-expressing mouse hearts. *Prog. Biophys. Mol. Biol.* **154**, 51–61 (2020).

78. Kopton, R. A. *et al.* Electromechanical assessment of optogenetically modulated cardiomyocyte activity. *J. Vis. Exp.* **2020**, 1–15 (2020).

79. Simone, S. A. De *et al.* The Role of Membrane Capacitance in Cardiac Impulse Conduction: An Optogenetic Study With Non-excitable Cells Coupled to Cardiomyocytes. *Front. Physiol.* **11**, 1–16 (2020).

80. Radisic, M., Marsano, A., Maidhof, R., Wang, Y. & Vunjak-Novakovic, G. Cardiac tissue engineering using perfusion bioreactor systems. *Nat. Protoc.* **3**, 719–738 (2008).

81. Uchida, T., Kitora, R. & Gohara, K. Temperature dependence of synchronized beating of cultured neonatal rat heart-cell networks with increasing age measured by multi-electrode arrays. *Trends Med.* **18**, 1–10 (2018).

82. Souza, M. M. & Boyle, R. T. A moderate decrease in temperature inhibits the calcium signaling mechanism(s) of the regulatory volume decrease in chick embryo cardiomyocytes. *Brazilian J. Med. Biol. Res.* **34**, 137–141 (2001).

83. Wang, X. *et al.* Three-dimensional electronic scaffolds for monitoring and regulation of multifunctional hybrid tissues. *Extrem. Mech. Lett.* **35**, 1–9 (2020).

84. Feiner, R., Fleischer, S., Shapira, A., Kalish, O. & Dvir, T. Multifunctional degradable electronic scaffolds for cardiac tissue engineering. *J. Control. Release* **281**, 189–195 (2018).

85. Shevach, M., Fleischer, S., Shapira, A. & Dvir, T. Gold nanoparticle-decellularized matrix hybrids for cardiac tissue engineering. *Nano Lett.* **14**, 5792–5796 (2014).

86. Feiner, R. *et al.* Engineered hybrid cardiac patches with multifunctional electronics for online monitoring and regulation of tissue function. *Nat. Mater.* 1–8 (2016) doi:10.1038/nmat4590.

87. Bursac, N. *et al.* Cardiac muscle tissue engineering: toward an in vitro model for electrophysiological studies. *Am. J. Physiol. Circ. Physiol.* **277**, H433–H444 (2017).

88. Wood, R. W. On a remarkable case of uneven distribution of light in a diffraction grating spectrum. *Proc. Phys. Soc. London* **18**, 269–275 (1901).

89. FANO.U. The Theory of Anomalous Diffraction Gratings and of Quasi-Stationary Waves on Metallic Surfaces (Sommerfeld ' s Waves). **928**, (1936).

90. Otto, A. Excitation of nonradiative surface plasma waves in silver by the method of frustrated total reflection. *Zeitschrift für Phys.* **216**, 398–410 (1968).

91. Kretschmann, E. & Raether, H. Radiative Decay of Non Radiative Surface Plasmons Excited by Light. *Zeitschrift fur Naturforsch. - Sect. A J. Phys. Sci.* **23**, 2135–2136 (1968).

92. Liedberg, B., Nylander, C. & Lunström, I. Surface plasmon resonance for gas detection and biosensing. *Sensors and Actuators* **4**, 299–304 (1983).

93. Nylander, C., Liedberg, B. & Lind, T. Gas detection by means of surface plasmon resonance. *Sensors and Actuators* **3**, 79–88 (1982).

94. Zernii, E. Y. *et al.* Involvement of the recoverin C-terminal segment in recognition of the target enzyme rhodopsin kinase. *Biochem. J.* **435**, 441–450 (2011).

95. Seo, P.-S. *et al.* Identification of erythrocyte p55/MPP1 as a binding partner of NF2 tumor suppressor protein/Merlin. *Exp. Biol. Med. (Maywood).* **234**, 255–262 (2009).

96. Joo, J. Y. *et al.* Differential interactions of cerebellin precursor protein (Cbln) subtypes and neurexin variants for synapse formation of cortical neurons. *Biochem. Biophys. Res. Commun.* **406**, 627–632 (2011).

97. Han, W. & Shin, J. H. Low-cost, open-source 3D printed antibody dispenser for development and small-scale production of lateral flow assay strips. *HardwareX* **9**, e00188 (2021).

98. Borile, G. *et al.* Label-free, real-time on-chip sensing of living cells via grating-coupled surface plasmon resonance. *Biophys. Chem.* **254**, 106262 (2019).

99. Przybylski, C., Gonnet, F., Saesen, E., Lortat-Jacob, H. & Daniel, R. Surface plasmon resonance imaging coupled to on-chip mass spectrometry: a new tool to probe protein-GAG interactions. *Anal. Bioanal. Chem.* **412**, 507–519 (2020).

100. Johnston, M. M. W., Wilson, D. M., Booksh, K. S. & Cramer, J. Integrated optical computing: System-on-chip for surface plasmon resonance imaging. *Proc. - IEEE Int. Symp. Circuits Syst.* 3483–3486 (2005) doi:10.1109/ISCAS.2005.1465379.

101. Yang, C.-T., Méjard, R., Griesser, H. J., Bagnaninchi, P. O. & Thierry, B. Cellular Micromotion Monitored by Long-Range Surface Plasmon Resonance with Optical Fluctuation Analysis. *Anal. Chem.* **87**, 1456–1461 (2015).

102. Liu, C. *et al.* Live cell integrated surface plasmon resonance biosensing approach to mimic the regulation of angiogenic switch upon anti-cancer drug exposure. *Anal. Chem.* **86**, 7305–7310 (2014).

103. Wu, C. *et al.* Real-time Evaluation of Live Cancer Cells by *In Situ* Surface Plasmon Resonance and Electrochemical Study. *ACS Appl. Mater. Interfaces* 151022083726005 (2015) doi:10.1021/acsami.5b08066.

104. Wang, W. *et al.* Label-free measuring and mapping of binding kinetics of membrane proteins in single living cells. *Nat. Chem.* **4**, 846–853 (2012).

105. Fathi, F., Rezabakhsh, A., Rahbarghazi, R. & Rashidi, M. R. Early-stage detection of VE-cadherin during endothelial differentiation of human mesenchymal stem cells using SPR biosensor. *Biosens. Bioelectron.* **96**, 358–366 (2017).

106. Litviňuková, M. *et al.* Cells of the adult human heart. *Nature* **588**, 466–472 (2020).

107. Fang, H. *et al.* Capacitively coupled arrays of multiplexed flexible silicon transistors for long-term cardiac electrophysiology. *Nat. Biomed. Eng.* **1**, (2017).

108. Huang, B., Yu, F. & Zare, R. N. Surface plasmon resonance imaging using a high numerical aperture microscope objective. *Anal. Chem.* **79**, 2979–2983 (2007).

109. Dipalo, M. *et al.* Plasmonic meta-electrodes allow intracellular recordings at network level on high-density CMOS-multi-electrode arrays. *Nat. Nanotechnol.* **13**, 965–971 (2018).

110. Tang, J. *et al.* Plasmon-enhanced photoelectrochemical monitoring of Ca2+ from living cardiomyocytes. *J. Electroanal. Chem.* **759**, 14–20 (2015).

111. Dipalo, M. *et al.* Intracellular action potential recordings from cardiomyocytes by ultrafast pulsed laser irradiation of fuzzy graphene microelectrodes. *Sci. Adv.* **7**, 1–10 (2021).

112. Dipalo, M. *et al.* Intracellular and Extracellular Recording of Spontaneous Action Potentials in Mammalian Neurons and Cardiac Cells with 3D Plasmonic Nanoelectrodes. *Nano Lett.* **17**, 3932–3939 (2017).

113. Desbiolles, B. X. E., De Coulon, E., Bertsch, A., Rohr, S. & Renaud, P. Intracellular Recording of Cardiomyocyte Action Potentials with Nanopatterned Volcano-Shaped Microelectrode Arrays. *Nano Lett.* **19**, 6173–6181 (2019).

114. Ribeiro, A. *et al.* Considerations for an in vitro, cell-based testing platform for detection of drug-induced inotropic effects in early drug development. Part 2: Designing and fabricating microsystems for assaying cardiac contractility with physiological relevance using hum. *Front. Pharmacol.* **10**, 1–19 (2019).

115. Boudreau-Béland, J. *et al.* Spatiotemporal stability of neonatal rat cardiomyocyte monolayers spontaneous activity is dependent on the culture substrate. *PLoS One* **10**, 1–25 (2015).

116. Hayoz, S., Tiwari, P. B., Piszczek, G., Üren, A. & Brelidze, T. I. Investigating cyclic nucleotide and cyclic dinucleotide binding to HCN channels by surface plasmon resonance. *PLoS One* **12**, 1–20 (2017).

117. Schmid, C., Abi-gerges, N., Zellner, D. & Rast, G. Ion channel expression and electrophysiology of singular human (primary and induced pluripotent stem cell derived) cardiomyocytes. *bioRxiv* 2021.03.04.433834 (2021).

118. Ronaldson, K. *et al.* Adult-like cardiac tissue grown from human pluripotent stem cells. *Nature* **556**, 1–34 (2018).

119. Grant, A. O. Cardiac ion channels. *Circ. Arrhythmia Electrophysiol.* **2**, 185–194 (2009).

120. Primary, P., Isolation, N., Medium, N. C. & Yield, C. Pierce Primary Cardiomyoyctes Isolation Kit. **0747**,.

121. RTI. User ' s Manual User ' s Manual ユーザーズマニュアル. **2886**, 1–38 (2010).

122. Yang, F. & Zheng, J. High Temperature Sensitivity is Intrinsic to Voltage-Gated Potassium Channels. *Biophys. J.* **108**, 37a (2015).

123. Charalambous, K., O'Reilly, A. O., Bullough, P. A. & Wallace, B. A. Thermal and chemical unfolding and refolding of a eukaryotic sodium channel. *Biochim. Biophys. Acta - Biomembr.* **1788**, 1279–1286 (2009).

124. Buzatu, S. The temperature-induced changes in membrane potential. *Riv. di Biol. - Biol. Forum* **102**, 199–218 (2009).

125. Han, J., Cho, J., Choi, I., Kim, D. & Jang, I. Han et al 2017 Korean J Phys Pharm. **21**, 215–223 (2017).

126. Boudou, T. *et al.* A microfabricated platform to measure and manipulate the mechanics of engineered cardiac microtissues. *Tissue Eng. - Part A* **18**, 910–919 (2012).

127. Grune, T., Ott, C., Häseli, S., Höhn, A. & Jung, T. The "MYOCYTER" – Convert cellular and cardiac contractions into numbers with ImageJ. *Sci. Rep.* **9**, 1–13 (2019).

128. Kreutzer, J. *et al.* Pneumatic unidirectional cell stretching device for mechanobiological studies of cardiomyocytes. *Biomech. Model. Mechanobiol.* **19**, 291–303 (2020).

129. Verkerk, A. O. *et al.* Patch-Clamp Recordings of Action Potentials From Human Atrial Myocytes: Optimization Through Dynamic Clamp. *Front. Pharmacol.* **12**, 1–16 (2021).

130. Stoppel, W. L. *et al.* HHS Public Access. 135–155 (2017) doi:10.1016/j.addr.2015.07.009.Electrical.

131. Landry, N. M., Rattan, S. G. & Dixon, I. M. C. An Improved Method of Maintaining Primary Murine Cardiac Fibroblasts in Two-Dimensional Cell Culture. *Sci. Rep.* **9**, 1–13 (2019).

132. Majid, Q. A. *et al.* Natural Biomaterials for Cardiac Tissue Engineering: A Highly Biocompatible Solution. *Front. Cardiovasc. Med.* **7**, 1–32 (2020).

133. Hayakawa, T. *et al.* Image-based evaluation of contraction-relaxation kinetics of human-induced pluripotent stem cell-derived cardiomyocytes: Correlation and complementarity with extracellular electrophysiology. *J. Mol. Cell. Cardiol.* **77**, 178–191 (2014).

134. Brod, E., Nimri, S., Turner, B. & Sivan, U. Electrical control over antibody-antigen binding. *Sensors Actuators, B Chem.* **128**, 560–565 (2008).

135. Kurita, R., Yokota, Y., Ueda, A. & Niwa, O. Measurement in a Microliter Volume Flow Cell for Biomolecules. **79**, 9572–9576 (2007).

136. Liu, C. *et al.* Real-time monitoring biomarker expression of carcinoma cells by surface plasmon resonance biosensors. *Chem. Commun.* **48**, 10389–10391 (2012).

137. Saqr, K. M. *et al.* Physiologic blood flow is turbulent. *Sci. Rep.* **10**, 1–12 (2020).

138. Zhang, B. *et al.* Biodegradable scaffold with built-in vasculature for organ-on-a-chip engineering and direct surgical anastomosis. *Nat. Mater.* **15**, 669–678 (2016).

139. Zhang, G. J. *et al.* An integrated chip for rapid, sensitive, and multiplexed detection of cardiac biomarkers from fingerprick blood. *Biosens. Bioelectron.* **28**, 459–463 (2011).

140. Jing, W., Hunt, A., Tao, N., Zhang, F. & Wang, S. Simultaneous quantification of protein binding kinetics in whole cells with surface plasmon resonance imaging and edge deformation tracking. *Membranes (Basel).* **10**, 1–9 (2020).

141. Quispe-Tintaya, W. 乳鼠心肌提取 HHS Public Access. *Physiol. Behav.* **176**, 139–148 (2017).

142. Argyraki, A. *et al.* （生物用）HHS Public Access. *2015 IEEE Summer Top. Meet. Ser. SUM 2015* **10**, 1–13 (2018).

143. Blaber, J., Adair, B. & Antoniou, A. Ncorr: Open-Source 2D Digital Image Correlation Matlab Software. *Exp. Mech.* **55**, 1105–1122 (2015).

144. A., Shafiq, C. W. N. S. S. J. R. B. 乳鼠心肌提取 HHS Public Access. *Physiol. Behav.* **176**, 139–148 (2017).

145. Nummi, A. *et al.* Epicardial Transplantation of Autologous Cardiac Micrografts During Coronary Artery Bypass Surgery. *Front. Cardiovasc. Med.* **8**, (2021).

146. Kalinin, A., Potyagaylo, D. & Kalinin, V. Solving the inverse problem of electrocardiography on the endocardium using a single layer source. *Front. Physiol.* **10**, 1–13 (2019).

147. Ivanushkina, N. G., Ivanko, K. O., Shpotak, M. O. & Prokopenko, Y. V. Solving the Inverse Problem of Relationship Between Action Potentials and Field Potentials in Cardiac Cells. *Visnyk NTUU KPI Seriia - Radiotekhnika Radioaparatobuduvannia* 53–59 (2021) doi:10.20535/RADAP.2021.85.53-59.

148. Ladeira, G. M. V., Lima, G. V., Ribeiro, M. A. & Balthazar, J. M. Kaplan Oscillator Configuration by Means of Bifurcation Diagrams to Generate the P and T Waves, in Addition QRS Complex of the ECG. *Brazilian J. Phys.* **51**, 644–652 (2021).

149. Krogh-Madsen, T. & Christini, D. J. Nonlinear dynamics in cardiology. *Annu. Rev. Biomed. Eng.* **14**, 179–203 (2012).

150. Karagueuzian, H. S., Stepanyan, H. & Mandel, W. J. Bifurcation theory and cardiac arrhythmias. *Am. J. Cardiovasc. Dis.* **3**, 1–16 (2013).

151. Berntson, G. G., Lozano, D. L. & Chen, Y. J. Filter properties of root mean square successive difference (RMSSD) for heart rate. *Psychophysiology* **42**, 246–252 (2005).

152. Bhalla, N., Jolly, P., Formisano, N. & Estrela, P. Introduction to biosensors. *Essays Biochem.* **60**, 1–8 (2016).

153. Ivanushkina, N. *et al.* Approach for Cardiac Action Potential Detection from Noised Recordings. *2019 IEEE 39th Int. Conf. Electron. Nanotechnology, ELNANO 2019 - Proc.* 530–535 (2019) doi:10.1109/ELNANO.2019.8783603.

154. Tun, U., Onn, H. & Sudirman, R. EEG Interpretation through Short Time Fourier Transform for Sensory Response Among Children. *Aust. J. Basic Appl. Sci.* 417–422 (2014).

155. Kolomenskii, A. A., Surovic, E. & Schuessler, H. A. Optical detection of acoustic waves with surface plasmons. *Appl. Opt.* **57**, 5604 (2018).

156. Kolomenskii, A. A., Surovic, E. & Schuessler, H. A. Acousto-optical Transducer with Surface Plasmons. *Int. J. Thermophys.* **39**, 1–10 (2018).

157. Tertoolen, L. G. J., Braam, S. R., van Meer, B. J., Passier, R. & Mummery, C. L. Interpretation of field potentials measured on a multi electrode array in pharmacological toxicity screening on primary and human pluripotent stem cell-derived cardiomyocytes. *Biochem. Biophys. Res. Commun.* **497**, 1135–1141 (2018).

158. Wang, T. W., Sung, Y. L., Chu, H. W. & Lin, S. F. IPG-based field potential measurement of cultured cardiomyocytes for optogenetic applications. *Biosens. Bioelectron.* **179**, 113060 (2021).

159. Raphel, F. *et al.* Identification of ion currents components generating field potential recorded in MEA from HIPSC-CM. *IEEE Trans. Biomed. Eng.* **65**, 1311–1319 (2018).

160. Hayes, H. B. *et al.* Novel method for action potential measurements from intact cardiac monolayers with multiwell microelectrode array technology. *Sci. Rep.* **9**, 1–13 (2019).

161. Kujala, V. J., Pasqualini, F. S., Goss, J. A., Nawroth, J. C. & Parker, K. K. Laminar ventricular myocardium on a microelectrode array-based chip. *J. Mater. Chem. B* **4**, 3534–3543 (2016).

162. Park, J. *et al.* Real-time measurement of the contractile forces of self-organized cardiomyocytes on hybrid biopolymer microcantilevers. *Anal. Chem.* **77**, 6571–6580 (2005).

163. Dai, Y., Oyunbaatar, N. E., Lee, B. K., Kim, E. S. & Lee, D. W. Spiral-shaped SU-8 cantilevers for monitoring mechanical response of cardiomyocytes treated with cardiac drugs. *Sensors Actuators, B Chem.* **255**, 3391–3399 (2018).

164. Herreras, O. Local field potentials: Myths and misunderstandings. *Front. Neural Circuits* **10**, 1–16 (2016).

165. Lind, J. U. *et al.* Cardiac Microphysiological Devices with Flexible Thin Film Sensors for Higher-Throughput Drug Screening. *Lab Chip* (2017) doi:10.1039/C7LC00740J.

166. Ferenczi, E. A., Tan, X. & Huang, C. L. H. Principles of Optogenetic Methods and Their Application to Cardiac Experimental Systems. *Front. Physiol.* **10**, (2019).

167. Kotadia, I. *et al.* Anisotropic cardiac conduction. *Arrhythmia Electrophysiol. Rev.* **9**, 202–210 (2021).

168. Hund, T. J. & Rudy, Y. Determinants of excitability in cardiac myocytes: Mechanistic investigation of memory effect. *Biophys. J.* **79**, 3095–3104 (2000).

169. Radisic, M. *et al.* Medium perfusion enables engineering of compact and contractile cardiac tissue. *Am. J. Physiol. Circ. Physiol.* **286**, H507–H516 (2004).

170. du Pré, B. C. *et al.* Neonatal rat cardiomyocytes as an in vitro model for circadian rhythms in the heart. *J. Mol. Cell. Cardiol.* **112**, 58–63 (2017).

171. Gilchrist, K. H., Lewis, G. F., Gay, E. A., Sellgren, K. L. & Grego, S. High-throughput cardiac safety evaluation and multi-parameter arrhythmia profiling of cardiomyocytes using microelectrode arrays. *Toxicol. Appl. Pharmacol.* **288**, 249–257 (2015).

172. Kaneko, T., Toriumi, H., Shimada, J. & Nomura, F. Extracellular field potential recording of single cardiomyocytes in agarose microchambers using microelectrode array. *Jpn. J. Appl. Phys.* **57**, (2018).

173. Kijlstra, J. D. *et al.* Integrated Analysis of Contractile Kinetics, Force Generation, and Electrical Activity in Single Human Stem Cell-Derived Cardiomyocytes. *Stem Cell Reports* **5**, 1226–1238 (2015).

174. Priest, B. T. & McDermott, J. S. Cardiac ion channels. *Channels* **9**, 352–359 (2015).

175. Chramiec, A. *et al.* Integrated human organ-on-a-chip model for predictive studies of anti-tumor drug efficacy and cardiac safety. *Lab Chip* **20**, 4357–4372 (2020).

176. Zhao, Y. *et al.* A Platform for Generation of Chamber-Specific Cardiac Tissues and Disease Modeling. *Cell* **176**, 913-927.e18 (2019).

177. Eng, G. *et al.* Autonomous beating rate adaptation in human stem cell-derived cardiomyocytes. *Nat. Commun.* **7**, 1–10 (2016).

178. Eng, G. *et al.* Autonomous beating rate adaptation in human stem cell-derived cardiomyocytes. *Nat. Commun.* **7**, 1–10 (2016).

179. O'Neill, S. C. & Eisner, D. A. A mechanism for the effects of caffeine on Ca2+ release during diastole and systole in isolated rat ventricular myocytes. *J. Physiol.* **430**, 519–536 (1990).

180. Chaban, R. *et al.* In-vitro examination of the positive inotropic effect of caffeine and taurine, the two most frequent active ingredients of energy drinks. *BMC Cardiovasc. Disord.* **17**, 1–8 (2017).

181. Rasmussen, C. A. F., Sutko, J. L. & Barry, W. H. Effects of ryanodine and caffeine on contractility, membrane voltage, and calcium exchange in cultured heart cells. *Circ. Res.* **60**, 495–504 (1987).

182. Wang, W. *et al.* Label-free measuring and mapping of binding kinetics of membrane proteins in single living cells. *Nat. Chem.* **4**, 846–53 (2012).

183. Edwards, G. and Physiology. **22**, 1–20 (1981).

184. Gao, J. *et al.* Assessment of sarcoplasmic reticulum calcium reserve and intracellular diastolic calcium removal in isolated ventricular cardiomyocytes. *J. Vis. Exp.* **2017**, 1–6 (2017).

185. Rich, R. L. *et al.* A global benchmark study using affinity-based biosensors. *Anal. Biochem.* **386**, 194–216 (2009).

186. Gondran, C., Dubois, M.-P., Fort, S., Cosnier, S. & Szunerits, S. Detection of carbohydrate-binding proteins by oligosaccharide-modified polypyrrole interfaces using electrochemical surface plasmon resonance. *Analyst* **133**, 206–12 (2008).

187. Singhal, A., Haynes, C. A. & Hansen, C. L. Microfluidic measurement of antibody-antigen binding kinetics from low-abundance samples and single cells. *Anal. Chem.* **82**, 8671–8679 (2010).

188. Wang, S., Huang, X., Shan, X., Foley, K. J. & Tao, N. Electrochemical surface plasmon resonance: Basic formalism and experimental validation. *Anal. Chem.* **82**, 935–941 (2010).

189. Liu, X. W. *et al.* Plasmonic-Based Electrochemical Impedance Imaging of Electrical Activities in Single Cells. *Angew. Chemie - Int. Ed.* **56**, 8855–8859 (2017).

190. Foley, K. J., Shan, X. & Tao, N. J. Surface impedance imaging technique. *Anal. Chem.* **80**, 5146–5151 (2008).

191. Borowska, M. Entropy-based algorithms in the analysis of biomedical signals. *Stud. Logic, Gramm. Rhetor.* **43**, 21–32 (2015).

192. Graff, B., Graff, G. & Kaczkowska, A. Entropy measures of heart rate variability for short ECG datasets in patients with congestive heart failure. *Acta Phys. Pol. B, Proc. Suppl.* **5**, 153–158 (2012).

193. Diab, A., Hassan, M., Marque, C. & Karlsson, B. Performance analysis of four nonlinearity analysis methods using a model with variable complexity and application to uterine EMG signals. *Med. Eng. Phys.* **36**, 761–767 (2014).

194. Jelinek, H. F., Cornforth, D. J., Tarvainen, M. P. & Miloevic, N. T. Multiscale renyi entropy and cardiac autonomic neuropathy. *Proc. - 2015 20th Int. Conf. Control Syst. Comput. Sci. CSCS 2015* 545–547 (2015) doi:10.1109/CSCS.2015.148.

195. Helakari, H. *et al.* Spectral entropy indicates electrophysiological and hemodynamic changes in drug-resistant epilepsy – A multimodal MREG study. *NeuroImage Clin.* **22**, (2019).

196. Lin, G. G. & Scott, J. G. Sample Entropy Analysis of Surface EMG for Improved Muscle Activity Onset Detection against Spurious Background Spikes. *J. Electromyogr. Kinesiol.* **100**, 130–134 (2012).

197. Ehler, E., Moore-Morris, T. & Lange, S. Isolation and Culture of Neonatal Mouse Cardiomyocytes. *J. Vis. Exp.* 1–10 (2013) doi:10.3791/50154.

198. Weyand, B. *et al.* Noninvasive Oxygen Monitoring in Three-Dimensional Tissue Cultures Under Static and Dynamic Culture Conditions. *Biores. Open Access* **4**, 266–277 (2015).

199. Claridge, S. & Yue, A. Cardiac channelopathies. *Med. (United Kingdom)* **46**, 618–621 (2018).

200. Zhang, Y. S. *et al.* HHS Public Access. 45–59 (2017)

doi:10.1016/j.biomaterials.2016.09.003.Bioprinting.

201. Sala, L. *et al.* Musclemotion: A versatile open software tool to quantify cardiomyocyte and cardiac muscle contraction in vitro and in vivo. *Circ. Res.* **122**, e5–e16 (2018).

202. Raedschelders, K., Ansley, D. M. & Chen, D. D. Y. The cellular and molecular origin of reactive oxygen species generation during myocardial ischemia and reperfusion. *Pharmacol. Ther.* **133**, 230–255 (2012).

203. Klabunde, R. E. Cardiac electrophysiology: Normal and ischemic ionic currents and the ECG. *Adv. Physiol. Educ.* **41**, 29–37 (2017).

204. Liu, C. *et al.* A 3D localized surface plasmon resonance biosensor for the study of trivalent arsenic binding to the ArsA ATPase. *Biosens. Bioelectron.* **38**, 19–26 (2012).

VITA

ROBERT SMITH

Born, Hastings, Florida

2022	PhD, Biomedical Engineering Florida International University Miami, Florida